MMNSA

Mathematical Modelling and Numerical Simulation with Applications

ISSN Online : 2791-8564

Year : 2023

Volume : 3

Issue : 1

https://dergipark.org.tr/en/pub/mmnsa

Editor-in-Chief
Mehmet Yavuz, PhD

VOLUME: 3 ISSUE: 1
ISSN ONLINE: 2791-8564

March 2023
https://dergipark.org.tr/en/pub/mmnsa

MATHEMATICAL MODELLING AND NUMERICAL SIMULATION WITH APPLICATIONS

Technical Editor

English Editor

Editorial Secretariat

Contents

Research Articles

Mathematical Modelling and Numerical Simulation with Applications, 2023, 3(1), 1–16

https://dergipark.org.tr/en/pub/mmnsa

ISSN Online: 2791-8564 / Open Access

https://doi.org/10.53391/mmnsa.1273908

RESEARCH PAPER

A three-component prey-predator system with interval number

Dipankar Ghosh [1,‡], **Prasun Kumar Santra** [2,‡,*] **and Ghanshaym Singha Mahapatra** [1,‡]

[1]Department of Mathematics, National Institute of Technology Puducherry, Karaikal-609609, India,
[2]Abada Nsup School, Abada-711313, Howrah, India

*Corresponding Author
‡dipankar.msc@gmail.com (Dipankar Ghosh); prasunsantra5@gmail.com (Prasun Kumar Santra); gs.mahapatra@nitpy.ac.in (Ghanshaym Singha Mahapatra)

Abstract

This paper presents a three-component model consisting of one prey and two predator species using imprecise biological parameters as interval numbers and applied functional parametric form in the proposed prey-predator system. The positivity and boundedness of the model are checked, and a stability analysis of the five equilibrium points is performed. Numerical simulations are performed to study the effect of the interval number and to illustrate analytical studies.

Keywords: Prey-predator; interval number; stability; competition; uncertainty

AMS 2020 Classification: 34D20; 34D23; 37C25; 37D45; 39A28

1 Introduction

The dynamics of predator-prey relationships [1–5] relationships is an essential aspect of any ecosystem where plants, animals, and other living organisms coexist in a delicate balance. Prey-predator model dynamics [6–10] are influenced by a variety of factors, including environmental conditions, competition from the predator population, and mortality rates. Mathematical ecology is an area of study that investigates the dynamic relationships between prey and predators. In this research, we analyze a three-species prey-predator model [11–15] with competition in predator populations to study dynamics with imprecise parameters.

Most previous research on prey-predator models has been based on the assumption of exact biological parameters [1–15]. However, in reality, biological parameters may not be fixed and can change due to various reasons, making the exact estimation of these parameters difficult. To address this issue, we consider interval number biological parameters in our study. Interval

➤ **Received:** 15.01.2023 ➤ **Revised:** 07.03.2023 ➤ **Accepted:** 10.03.2023 ➤ **Published:** 31.03.2023

numbers allow us to incorporate uncertainty into our models and make more realistic predictions about the behavior of the system.

Furthermore, using interval numbers for parameters can capture the complex dynamics of predator-prey systems, such as boom-bust cycles, where the populations of both species oscillate over time. Interval numbers can also provide greater flexibility in modeling a prey-predator system, enabling us to simulate the effect of different environmental factors on the system and explore different scenarios.

In this paper, we focus on studying the advantages of using interval number biological parameters for prey-predator systems and the effect of certain model parameters on the system. Although some studies have explored the use of interval parameters in prey-predator models [16–22], our research offers new insights into the potential benefits of this approach. Ultimately, our findings can contribute to a better understanding and management of these vital ecosystems.

2 Prey-predator imprecise model with interval number

In this proposed model, we consider one prey species and two predator species. Let $X(t)$ denote the prey density, $Y(t)$ the 1^{st} predator and $Z(t)$ the 2^{nd} predator density at any time t.

The biological environment of populations is not completely predictable, so the biological parameters of modeling the prey-predator system should be considered imprecise. The proposed prey-predator system is developed on the following assumptions:

Assumption 1. The prey population grows according to the logistic curve with carrying capacity $k(k\epsilon\mathbb{R}_+)$ and with an intrinsic growth rate $r(r\epsilon\mathbb{R}_+)$, in the absence of both predator species. The logistic equation is a mathematical model that describes the growth of a population over time. It is represented by the following differential equation:

$$\frac{dN}{dt} = rN\left(1 - \frac{N}{K}\right),$$

where N is the population size, t is time, r is the intrinsic growth rate of the population, and K is the carrying capacity, which is the maximum number of individuals that the environment can support.

The logistic equation incorporates the concept of density dependence, which means that the growth rate of the population decreases as it approaches the carrying capacity. This results in an S-shaped growth curve, where the population initially grows rapidly, slows down as it approaches the carrying capacity, and eventually stabilizes at the carrying capacity. In the presence of predators, Y and Z, the population of prey X will decrease due to the attack of predators. The first and second predators attack the prey with an interval-valued rate $\widehat{\beta}_1\,(>0)$ and $\widehat{\beta}_2\,(>0)$ respectively and the Holling type I functional response manner. Holling type function, also known as the functional response curve, is a mathematical model that describes the rate at which a predator consumes prey as a function of prey density. It is named after Canadian ecologist C.S. Holling, who first proposed the idea in the 1950s.

The Holling type function is typically represented by one of three functional forms:

Type I: $f(x) = ax$, where a is a constant that represents the attack rate of the predator.

Type II: $f(x) = \frac{ax}{1+\frac{ax}{h}}$, where h is a constant that represents the handling time, or the time it takes for the predator to consume a single prey item.

Type III: $f(x) = \frac{ax^2}{1+bx+\frac{x^2}{k}}$, where b and k are constants that determine the shape of the curve.

In general, the Holling type function predicts that the rate of predation increases with prey density up to a certain point, after which the rate of predation begins to level off as the predator becomes

saturated with prey. The precise shape of the curve depends on the specific functional form of the model. Then the mathematical form of the above assumption is as follows.

$$\frac{dX}{dt} = rX\left(1-\frac{X}{k}\right) - \widehat{\beta}_1 XY - \widehat{\beta}_2 XZ. \tag{1}$$

Assumption 2. Prey X are food for predators (Y and Z), so in the presence of food, the population density of predators (Y and Z) will increase in the Holling type I functional response manner. We introduced the natural death of predators. Here we also consider the competition between the predators, and for this reason, the population density of both predators will decrease. We consider the competition parameters $\widehat{\delta}_1$ and $\widehat{\delta}_2$ to be imprecise. Hence, from the above assumption, we have

$$\frac{dY}{dt} = \widehat{\beta}_1 XY - d_1 Y - \widehat{\delta}_1 YZ, \tag{2}$$

$$\frac{dZ}{dt} = \widehat{\beta}_2 XZ - d_2 Z - \widehat{\delta}_2 YZ. \tag{3}$$

Therefore, our final mathematical model with four interval-valued parameters is as follows.

$$\begin{aligned} \frac{dX}{dt} &= rX\left(1-\frac{X}{k}\right) - \widehat{\beta}_1 XY - \widehat{\beta}_2 XZ, \\ \frac{dY}{dt} &= \widehat{\beta}_1 XY - d_1 Y - \widehat{\delta}_1 YZ, \\ \frac{dZ}{dt} &= \widehat{\beta}_2 XZ - d_2 Z - \widehat{\delta}_2 YZ, \end{aligned} \tag{4}$$

where $\widehat{\beta}_1 \in [\beta_{1l}, \beta_{1u}]$, $\widehat{\beta}_2 \in [\beta_{2l}, \beta_{2u}]$, $\widehat{\delta}_1 \in [\delta_{1l}, \delta_{1u}]$, $\widehat{\delta}_2 \in [\delta_{2l}, \delta_{2u}]$, for $\beta_{1l} > 0$, $\beta_{2l} > 0$, $\delta_{1l} > 0$ and $\delta_{2l} > 0$, with initial conditions

$$X(0) > 0, Y(0) > 0, \text{ and } Z(0) > 0. \tag{5}$$

Using the parametric form of interval-valued parameters, the equations (4) can be written in the parametric prey-predator model [16, 17] for $p \in [0,1]$ is as follows:

$$\begin{aligned} \frac{dX}{dt} &= rX\left(1-\frac{X}{k}\right) - \beta_{1l}^{1-p}\beta_{1u}^{p} XY - \beta_{2l}^{1-p}\beta_{2u}^{p} XZ, \\ \frac{dY}{dt} &= \beta_{1l}^{1-p}\beta_{1u}^{p} XY - d_1 Y - \delta_{1l}^{1-p}\delta_{1u}^{p} YZ, \\ \frac{dZ}{dt} &= \beta_{2l}^{1-p}\beta_{2u}^{p} XZ - d_2 Z - \delta_{2l}^{1-p}\delta_{2u}^{p} YZ, \end{aligned} \tag{6}$$

subject to the initial conditions

$$X(0) > 0, Y(0) > 0 \text{ and } Z(0) > 0. \tag{7}$$

The biological descriptions of each parameter have been discussed in Table 1.

Table 1. Biological meaning of the model parameters

Parameter	Biological meaning
X	Prey species
Y	1^{st} predator species
Z	2^{nd} predator species
r	Intrinsic growth rate
k	Carrying capacity
β_1	Consumption rate of 1^{st} predator
β_2	Consumption rate of 2^{nd} predator
δ_1	Competition rate between the 1^{st} predator (Y) to 2^{nd} predator (Z)
δ_2	Competition rate between the 2^{nd} predator (Z) to 1^{st} predator (Y)
d_1	Natural death rate of 1^{st} predator
d_2	Natural death rate of 2^{nd} predator

3 Dynamical behavior

In this section, we describe the rigorous dynamical behavior of the proposed model system. To do so, we first check the positivity of the solutions of the interval model and the uniform boundedness of the solution of the same model.

Positivity

Theorem 1 *Every solution of system (6) with initial conditions (7) exists in the interval* $[0,\infty)$ *and* $X(0)>0, Y(0)>0$ *and* $Z(0)>0$ *for all* $t\geq 0$.

Proof Since the right-hand side of the system (6) is completely continuous and locally Lipschitzian on C, the solution $(X(t), Y(t), Z(t))$ of (6) with initial conditions (7) exists and is unique on $[0,\xi)$, where $0<\xi<\infty$.
From system (6) with initial conditions (7), we have

$$X(t)=X(0)exp\left[\int_0^t\{r(1-(X(\theta))/k)-\beta_{1l}^{1-p}\beta_{1u}^{p}Y(\theta)-\beta_{2l}^{1-p}\beta_{2u}^{p}Z(\theta)\}d\theta\right]>0,$$

$$Y(t)=Y(0)exp\left[\int_0^t\{\beta_{1l}^{1-p}\beta_{1u}^{p}X(\theta)-d_1-\delta_{1l}^{1-p}\delta_{1u}^{p}Z(\theta)\}d\theta\right]>0,$$

$$Z(t)=Z(0)exp\left[\int_0^t\{\beta_{2l}^{1-p}\beta_{2u}^{p}X(\theta)-d_2-\delta_{2l}^{1-p}\delta_{2u}^{p}Y(\theta)\}d\theta\right]>0,$$

which completes the proof. ■

Uniform boundedness

Theorem 2 *The solutions of the model system (6) are completely bounded.*

Proof We construct a function such as $\Lambda(t)=X(t)+Y(t)+Z(t)$.
Differentiating both sides with respect to t, we have

$$\frac{d\Lambda(t)}{dt}=\frac{dX(t)}{dt}+\frac{dY(t)}{dt}+\frac{dZ(t)}{dt}.$$

Therefore,

$$\frac{d\Lambda}{dt} = rX(1-\frac{X}{k}) - \beta_{1l}^{1-p}\beta_{1u}^{p}XY - \beta_{2l}^{1-p}\beta_{2u}^{p}XZ$$
$$+\beta_{1l}^{1-p}\beta_{1u}^{p}XY - d_1Y - \delta_{1l}^{1-p}\delta_{1u}^{p}YZ + \beta_{2l}^{1-p}\beta_{2u}^{p}XZ - d_2Z - \delta_{2l}^{1-p}\delta_{2u}^{p}YZ$$
$$= rX(1-\frac{X}{k}) - \left(\delta_{1l}^{1-p}\delta_{1u}^{p} + \delta_{2l}^{1-p}\delta_{2u}^{p}\right)YZ - d_1Y - d_2Z.$$

Now,

$$\frac{d\Lambda}{dt} + \gamma\Lambda == rX(1-\frac{X}{k}) - \left(\delta_{1l}^{1-p}\delta_{1u}^{p} + \delta_{2l}^{1-p}\delta_{2u}^{p}\right)YZ - d_1Y - d_2Z + \gamma\left(X+Y+Z\right).$$
$$\frac{d\Lambda}{dt} + \gamma\Lambda = \left(rX - \frac{rX^2}{k} + \gamma X\right) - \left(d_1-\gamma\right)X - \left(d_2-\gamma\right)Y - \left(\delta_{1l}^{1-p}\delta_{1u}^{p} + \delta_{2l}^{1-p}\delta_{2u}^{p}\right)YZ.$$

Since $\left(\delta_{1l}^{1-p}\delta_{1u}^{p} + \delta_{2l}^{1-p}\delta_{2u}^{p}\right)YZ > 0$ and assuming $\gamma < \min\left(d_1, d_2\right)$, then from the above equation, we have

$$\frac{d\Lambda}{dt} + \gamma\Lambda \leq \left(rX - \frac{rX^2}{k} + \gamma X\right) \leq k\frac{(r+\gamma)^2}{4r} = A\,(say).$$

Applying the result of differential inequality, we obtain,
$0 \leq \Lambda\left(X(t), Y(t), Z(t)\right) \leq \frac{A}{\gamma}\left(1-e^{-\gamma t}\right) + \Lambda\left(X(0), Y(0), Z(0)\right)e^{-\gamma t}$,
which implies that $0 \leq \Lambda \leq \frac{A}{\gamma}$ as $t \to \infty$.
Hence all the solutions of (6) is uniformly bounded. ■

4 Equilibrium points and their existence and stability

In this section, we study the existence and stability behavior of the system (6) at equilibrium points of the model system (6) are:
(I) Trivial equilibrium $E_0\left(0,0,0\right)$, (II) Axial equilibrium $E_1\left(k,0,0\right)$, (III) Planar equilibrium
(a) $E_2\left(X_2, Y_2, 0\right)$ where $X_2 = \frac{d_1}{\beta_{1l}^{1-p}\beta_{1u}^{p}}$ and $Y_2 = \frac{r}{\beta_{1l}^{1-p}\beta_{1u}^{p}}\left(1 - \frac{d_1}{\beta_{1l}^{1-p}\beta_{1u}^{p}k}\right)$, (b) $E_3\left(X_3, 0, Z_3\right)$,
where $X_3 = \frac{d_2}{\beta_{2l}^{1-p}\beta_{2u}^{p}}$ and $Z_3 = \frac{r}{\beta_{2l}^{1-p}\beta_{2u}^{p}}\left(1 - \frac{d_2}{\beta_{2l}^{1-p}\beta_{2u}^{p}k}\right)$. (IV) Interior equilibrium $E^*\left(X^*, Y^*, Z^*\right)$,
where $X^* = \frac{k\left(\beta_{1l}^{1-p}\beta_{1u}^{p}\delta_{1l}^{1-p}\delta_{1u}^{p}d_2 + rd_1\delta_{2l}^{1-p}\delta_{2u}^{p} + \beta_{2l}^{1-p}\beta_{2u}^{p}d_1\delta_{2l}^{1-p}\delta_{2u}^{p}\right)}{r\delta_{1l}^{1-p}\delta_{1u}^{p}\delta_{2l}^{1-p}\delta_{2u}^{p} + k\beta_{1l}^{1-p}\beta_{1u}^{p}\beta_{2l}^{1-p}\beta_{2u}^{p}\left(\delta_{1l}^{1-p}\delta_{1u}^{p} + \delta_{2l}^{1-p}\delta_{2u}^{p}\right)} > 0$, $Y^* = \frac{\beta_{2l}^{1-p}\beta_{2u}^{p}X^* - d_2}{\delta_{2l}^{1-p}\delta_{2u}^{p}}$,
and $Z^* = \frac{\beta_{1l}^{1-p}\beta_{1u}^{p}X^* - d_1}{\delta_{1l}^{1-p}\delta_{1u}^{p}}$.
Now $Y^* > 0$ if $\beta_{2l}^{1-p}\beta_{2u}^{p}X^* > d_2$, and $Z^* > 0$ if $\beta_{1l}^{1-p}\beta_{1u}^{p}X^* > d_1$.

Local stability analysis

In this section, we study the local stability of the system (6) at various equilibrium points.

Theorem 3 *The equilibrium point E_0 is always unstable.*

Proof Variational matrix of system (6) at $E_0(0,0,0)$ is given by

$$V(E_0) = \begin{pmatrix} r & 0 & 0 \\ 0 & -d_1 & 0 \\ 0 & 0 & -d_2 \end{pmatrix}.$$

Therefore, eigenvalues of the characteristic equation of $V(E_0)$ are $\lambda_1 = r > 0$, $\lambda_2 = -d_1 < 0$, $\lambda_3 = -d_2 < 0$. Here, one of the eigenvalues is positive and the other two are negative, so E_0 is always unstable. ■

Theorem 4 *The equilibrium point E_1 is stable if $\beta_{1l}^{1-p}\beta_{1u}^{p}k < d_1$ and $\beta_{2l}^{1-p}\beta_{2u}^{p}k < d_2$.*

Proof Variational matrix of system (6) at $E_1(k,0,0)$ is given by

$$V(E_1) = \begin{pmatrix} -r & -\beta_{1l}^{1-p}\beta_{1u}^{p}k & -\beta_{2l}^{1-p}\beta_{2u}^{p}k \\ 0 & \beta_{1l}^{1-p}\beta_{1u}^{p}k - d_1 & 0 \\ 0 & 0 & \beta_{2l}^{1-p}\beta_{2u}^{p}k - d_2 \end{pmatrix}.$$

The eigenvalues of the characteristic equation of $V(E_1)$ are $\lambda_1 = -r < 0$, $\lambda_2 = \beta_{1l}^{1-p}\beta_{1u}^{p}k - d_1$, $\lambda_3 = \beta_{2l}^{1-p}\beta_{2u}^{p}k - d_2$. Therefore, E_1 is stable if $\beta_{1l}^{1-p}\beta_{1u}^{p}k < d_1$ and $\beta_{2l}^{1-p}\beta_{2u}^{p}k < d_2$. ■

Theorem 5 *The equilibrium point E_2 is locally asymptotically stable if $d_2 > \beta_{2l}^{1-p}\beta_{2u}^{p}X_2 - \delta_{2l}^{1-p}\delta_{2u}^{p}Y_2$, $A_1 > 0$ and $A_2 > 0$.*

Proof The variational matrix of system (6) at $E_2\,(X_2, Y_2, 0)$ is given by

$$V(E_2) = \begin{pmatrix} m_{11} & m_{12} & m_{13} \\ m_{21} & m_{22} & m_{23} \\ 0 & 0 & m_{33} \end{pmatrix},$$

where $m_{11} = r - \frac{2rX_2}{k} - \beta_{1l}^{1-p}\beta_{1u}^{p}Y_2$, $m_{12} = -\beta_{1l}^{1-p}\beta_{1u}^{p}X_2$, $m_{13} = -\beta_{2l}^{1-p}\beta_{2u}^{p}X_2$, $m_{21} = \beta_{1l}^{1-p}\beta_{1u}^{p}Y_2$, $m_{22} = \beta_{1l}^{1-p}\beta_{1u}^{p}X_2 - d_1$, $m_{23} = -\delta_{1l}^{1-p}\delta_{1u}^{p}Y_2$, $m_{33} = \beta_{2l}^{1-p}\beta_{2u}^{p}X_2 - d_2 - \delta_{2l}^{1-p}\delta_{2u}^{p}Y_2$.
Now the characteristic equation for $V(E_2)$ is $(m_{33} - \lambda)\left\{\lambda^2 + A_1\lambda + A_2\right\} = 0$, where $A_1 = -(m_{11} + m_{22})$ and $A_2 = m_{11}m_{22} - m_{12}m_{21}$.
Therefore, one eigenvalue of the characteristic equation above is m_{33}, which is negative as $d_2 > \beta_{2l}^{1-p}\beta_{2u}^{p}X_2 - \delta_{2l}^{1-p}\delta_{2u}^{p}Y_2$ and the other two eigenvalues are negative if $A_1 > 0$ and $A_2 > 0$. Therefore, the second predator-free equilibrium point $E_2\,(X_2, Y_2, 0)$ is locally asymptotically stable if $d_2 > \beta_{2l}^{1-p}\beta_{2u}^{p}X_2 - \delta_{2l}^{1-p}\delta_{2u}^{p}Y_2$, $A_1 > 0$, and $A_2 > 0$, otherwise the system (6) will be unstable. ■

Theorem 6 *The equilibrium point E_3 is locally asymptotically stable if $d_1 > \beta_{1l}^{1-p}\beta_{1u}^{p}X_3 - \delta_{1l}^{1-p}\delta_{1u}^{p}Z_3$, $B_1 > 0$ and $B_2 > 0$.*

Proof The variational matrix of system (6) at $E_3\,(X_3, 0, Z_3)$ is given by

$$V(E_3) = \begin{pmatrix} p_{11} & p_{12} & p_{13} \\ 0 & p_{22} & 0 \\ p_{31} & p_{32} & p_{33} \end{pmatrix},$$

where $p_{11} = r - \frac{2rX_3}{k} - \beta_{2l}^{1-p}\beta_{2u}^{p}Z_3$, $p_{12} = -\beta_{1l}^{1-p}\beta_{1u}^{p}X_3$, $p_{13} = -\beta_{2l}^{1-p}\beta_{2u}^{p}X_3$, $p_{22} = \beta_{1l}^{1-p}\beta_{1u}^{p}X_3 - d_1 - \delta_{1l}^{1-p}\delta_{1u}^{p}Z_3$, $p_{31} = \beta_{2l}^{1-p}\beta_{2u}^{p}Z_3$, $p_{32} = -\delta_{2l}^{1-p}\delta_{2u}^{p}Z_3$, $p_{33} = \beta_{2l}^{1-p}\beta_{2u}^{p}X_3 - d_2$.
The characteristic equation for $V(E_3)$ is $(p_{22} - \lambda)\left(\lambda^2 + B_1\lambda + B_2\right) = 0$, where $B_1 = -(p_{11} + p_{33})$ and $B_2 = p_{11}p_{33} - p_{13}p_{31}$.
Therefore, the eigenvalue of the characteristic equation above is p_{22}, which is negative as $d_1 > \beta_{1l}^{1-p}\beta_{1u}^{p}X_3 - \delta_{1l}^{1-p}\delta_{1u}^{p}Z_3$, and the other two eigenvalues are negative if $B_1 > 0$ and $B_2 > 0$.
The first predator-free equilibrium point $E_3\,(X_3, 0, Z_3)$ is locally asymptotically stable if $d_1 > \beta_{1l}^{1-p}\beta_{1u}^{p}X_3 - \delta_{1l}^{1-p}\delta_{1u}^{p}Z_3$, $B_1 > 0$ and $B_2 > 0$, otherwise the system (6) will be unstable. ■

Theorem 7 *The equilibrium point E^* is locally asymptotically stable if the inequalities $A > 0$, $C > 0$, $AB - C > 0$ are satisfied.*

Proof Variational matrix of system (6) at $E^*(X^*, Y^*, Z^*)$ is given by,

$$V(E^*) = \begin{pmatrix} a_{11} & a_{12} & a_{13} \\ a_{21} & a_{22} & a_{23} \\ a_{31} & a_{32} & a_{33} \end{pmatrix},$$

where $a_{11} = r - \frac{2rX^*}{k} - \beta_{1l}^{1-p}\beta_{1u}^{p}Y^* - \beta_{2l}^{1-p}\beta_{2u}^{p}Z^*$, $a_{12} = -\beta_{1l}^{1-p}\beta_{1u}^{p}X^*$, $a_{13} = -\beta_{2l}^{1-p}\beta_{2u}^{p}X^*$, $a_{21} = \beta_{1l}^{1-p}\beta_{1u}^{p}Y^*$, $a_{22} = \beta_{1l}^{1-p}\beta_{1u}^{p}X^* - \delta_{1l}^{1-p}\delta_{1u}^{p}Z^* - d_1$, $a_{23} = -\delta_{1l}^{1-p}\delta_{1u}^{p}Y^*$, $a_{31} = \beta_{2l}^{1-p}\beta_{2u}^{p}Z^*$, $a_{32} = -\delta_{2l}^{1-p}\delta_{2u}^{p}Z^*$, $a_{33} = \beta_{2l}^{1-p}\beta_{2u}^{p}X^* - \delta_{2l}^{1-p}\delta_{2u}^{p}Y^* - d_2$.

Therefore, the characteristic equation of $V(E^*)$ is

$$\lambda^3 + A\lambda^2 + B\lambda + C = 0, \tag{8}$$

where, $A = -(a_{11} + a_{22} + a_{33})$, $B = -\left(a_{12}a_{21} + a_{13}a_{31} + a_{23}a_{32} - a_{11}a_{22} - a_{11}a_{33} - a_{22}a_{33}\right)$, $C = -(a_{11}a_{22}a_{33} + a_{12}a_{23}a_{31} + a_{13}a_{21}a_{32} - a_{13}a_{22}a_{31} - a_{12}a_{21}a_{33} - a_{11}a_{23}a_{32})$.

According to the Routh-Hurwitz criterion, all eigenvalues of the characteristic equation (8) have negative real parts, which means that the system (6) shows local asymptotic stability at E^* if and only if $A > 0$, $C > 0$, $AB - C > 0$. ■

Remark 1 *When analyzing the stability of a model with exact biological parameters, the results are typically the same as those for the model with the corresponding imprecise biological parameters. The key difference between the two lies in the nature of the parameters used. While exact parameter models use precise numerical values, imprecise biological parameter models employ uncertain parameters that are often in the form of probability distributions or ranges of values. Despite this difference, the stability analysis techniques used for both types of models are essentially the same.*

Global stability analysis

In this section, we discuss the global stability behavior of the system (6) at interior equilibrium point $E^*(X^*, Y^*, Z^*)$. Studying the global stability of the equilibrium points using Lyapunov's direct method has gained popularity in recent years, but constructing suitable Lyapunov functions can be challenging. In general, there are no systematic methods for constructing Lyapunov functions for prey-predator models. However, the most commonly used types of Lyapunov

functions are quadratic and Volterra-type functions. In this study, the global stability of the equilibrium states was demonstrated using a Volterra-type Lyapunov function [23–28]. This function was carefully chosen because of its effectiveness in analyzing the stability of dynamical systems with more complex behavior.

Theorem 8 *If E^* is locally asymptotically stable, then E^* is globally asymptotically stable in*

$$G = \{(X, Y, Z) : X > X^*, Y > Y^* \text{ and } Z > Z^* \text{or } X < X^*, Y < Y^* \text{ and } Z < Z^*\}. \tag{9}$$

Proof Let

$$L(X, Y, Z) = \alpha_1 \left(X - X^* - X^* \ln \frac{X}{X^*} \right) + \alpha_2 \left(Y - Y^* - Y^* \ln \frac{Y}{Y^*} \right) + \alpha_3 \left(Z - Z^* - Z^* \ln \frac{Z}{Z^*} \right),$$

where α_1, α_2 and α_3 are positive constants that will be chosen later.
Define $L_1(X) = \left(X - X^* - X^* \ln \left(\frac{X}{X^*} \right) \right)$, $L_2(Y) = \left(Y - Y^* - Y^* \ln \left(\frac{Y}{Y^*} \right) \right)$,
and $L_3(Z) = \left(Z - Z^* - Z^* \ln \left(\frac{Z}{Z^*} \right) \right)$, therefore, $L(X, Y, Z) = \alpha_1 L_1(X) + \alpha_2 L_2(Y) + \alpha_3 L_3(Z)$.
Differentiating $L(X, Y, Z)$ along the solution of the system (6) with respect to t, we get

$$\frac{dL}{dt} = \alpha_1 \left(1 - \frac{X^*}{X} \right) \frac{dX}{dt} + \alpha_2 \left(1 - \frac{Y^*}{Y} \right) \frac{dY}{dt} + \alpha_3 \left(1 - \frac{Z^*}{Z} \right) \frac{dZ}{dt}. \tag{10}$$

Linear approximations $X - X^* \cong X$, $Y - Y^* \cong Y$ and $Z - Z^* \cong Z$ are used to compute $\frac{dL_1(X(t))}{dt}$, $\frac{dL_2(Y(t))}{dt}$ and $\frac{dL_3(Z(t))}{dt}$ as follows:

$$\begin{aligned} \frac{dL_1}{dt} &= \left(1 - \frac{X^*}{X} \right) \left[r \left(1 - \frac{X}{k} \right) - \beta_{1l}^{1-p} \beta_{1u}^{p} Y - \beta_{2l}^{1-p} \beta_{2u}^{p} Z \right] X \\ &= -\frac{r}{k} (X - X^*)^2 - \beta_{1l}^{1-p} \beta_{1u}^{p} (X - X^*)(Y - Y^*) - \beta_{2l}^{1-p} \beta_{2u}^{p} (Z - Z^*)(X - X^*), \end{aligned}$$

$$\begin{aligned} \frac{dL_2}{dt} &= \left(1 - \frac{Y^*}{Y} \right) \left[\beta_{1l}^{1-p} \beta_{1u}^{p} X - d_1 - \delta_{1l}^{1-p} \delta_{1u}^{p} Z \right] Y \\ &= \beta_{1l}^{1-p} \beta_{1u}^{p} (X - X^*)(Y - Y^*) - \delta_{1l}^{1-p} \delta_{1u}^{p} (Z - Z^*)(X - X^*), \end{aligned}$$

and

$$\begin{aligned} \frac{dL_3}{dt} &= \left(1 - \frac{Z^*}{Z} \right) \left[\beta_{2l}^{1-p} \beta_{2u}^{p} X - d_2 - \delta_2 Y \right] Z \\ &= \beta_{2l}^{1-p} \beta_{2u}^{p} (Z - Z^*)(X - X^*) - \delta_{2l}^{1-p} \delta_{2u}^{p} (Y - Y^*)(Z - Z^*). \end{aligned}$$

Now,

$$\frac{dL}{dt} = -\alpha_1 \frac{r}{k}(X-X^*)^2 - \left[\alpha_1 \beta_{2l}^{1-p}\beta_{2u}^{p} + \alpha_2 \delta_{1l}^{1-p}\delta_{1u}^{p} - \alpha_3 \beta_{2l}^{1-p}\beta_{2u}^{p}\right](Z-Z^*)(X-X^*)$$
$$+ (\alpha_2-\alpha_1)\beta_{1l}^{1-p}\beta_{1u}^{p}(X-X^*)(Y-Y^*) - \alpha_3 \delta_{2l}^{1-p}\delta_{2u}^{p}(Y-Y^*)(Z-Z^*).$$

Let $\alpha_2 = 1$ and $\alpha_3 = 1$, then $\alpha_1 = \alpha_2 = 1$. Hence,

$$\frac{dL}{dt} = -\frac{r}{k}(X-X^*)^2 - \delta_{1l}^{1-p}\delta_{1u}^{p}(Z-Z^*)(X-X^*) - \delta_{2l}^{1-p}\delta_{2u}^{p}(Y-Y^*)(Z-Z^*).$$

Now, we see that $\frac{dL}{dt}$ is negative definite in the region:

$$G = \{(X,Y,Z) : X > X^*, Y > Y^* \text{ and } Z > Z^* \text{or } X < X^*, Y < Y^* \text{ and } Z < Z^*\}.$$

Therefore, the theorem follows. ■

5 Numerical simulation

To validate our analytical studies, we performed numerical simulations using hypothetical parameter data. Obtaining real data for this purpose can be complex, and therefore, we chose to use hypothetical parameters for our simulations. This approach allows us to assess the precision of our analytical studies and provides us with a reliable means of testing the effectiveness of our models. In this study, we meticulously examine the influence of four significant parameters on the

Table 2. Value of the parameters for various simulations.

Parameter	Simulation 1	Simulation 2	Simulation 3	Simulation 4
r	0.8	0.8	0.8	0.8
k	5.0	5.0	5.0	5.0
$\widehat{\beta}_1$	$[0.3, 0.5]$	$[0.4, 0.6]$	$[0.3, 0.5]$	$[0.3, 0.5]$
$\widehat{\beta}_2$	$[0.3, 0.5]$	$[0.3, 0.5]$	$[0.3, 0.5]$	$[0.3, 0.5]$
$\widehat{\delta}_1$	$[0.04, 0.06]$	$[0.04, 0.06]$	$[0.05, 0.07]$	$[0.04, 0.06]$
$\widehat{\delta}_2$	$[0.04, 0.06]$	$[0.04, 0.06]$	$[0.04, 0.06]$	$[0.04, 0.06]$
d_1	0.1	0.1	0.1	0.1
d_2	0.1	0.1	0.1	0.1
p	0.5	0.5	0.5	$0.0, 0.2, 0.4, 0.6, 0.8, 1.0$

model system by using the four-parameter state approach, while simultaneously exploring the potential benefits of incorporating interval numbers into our analysis. In doing so, our objective is to expand our understanding of the model system and to provide valuable insight into its behavior under varying conditions.

For the parameter set of **simulation 1**, we find that equilibrium points of the model are $E_0\,(0,0,0)$, $E_1\,(5,0,0)$, $E_2\,(0.2582, 1.9589, 0)$, $E_3\,(0.2582, 0, 1.9589)$ and $E^*\,(0.3789, 0.9545, 0.9545)$.

And corresponding eigenvalues are $-0.1000, -0.1000, 0.8000; -0.8000, 1.8365, 1.8365; -0.0207 \pm 0.2747i$,

$-0.0960; -0.0207 \pm 0.2747i, -0.0960$ and $-0.0297 \pm 0.3313i, -0.0012$. Among these points, E_2, E_3 and E^* are stable. Fig. 1 supports our results.

To study the effect of the transmission coefficient ($\widehat{\beta}_1$ and $\widehat{\beta}_2$) on the model, we change the value of the parameter $\widehat{\beta}_1$ in **simulation 2** compared to **simulation 1**. For the parameter set of **simulation 2**, $E_0\,(0,0,0)$, $E_1\,(5,0,0)$, $E_2\,(0.2041, 1.5663, 0)$, $E_3\,(0.2582, 0, 1.9589)$ and $E^*\,(0.3277, 0.5492, 1.2355)$

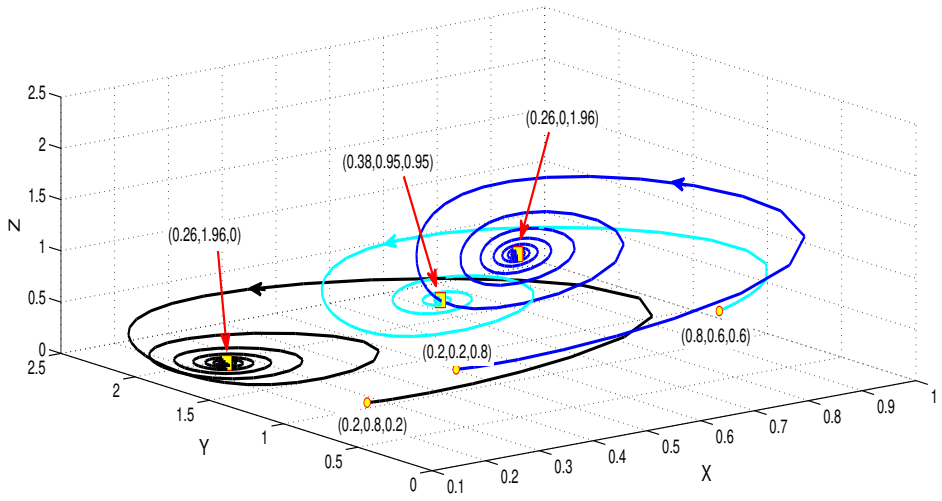

Figure 1. Dynamical behaviour for the equilibrium points.

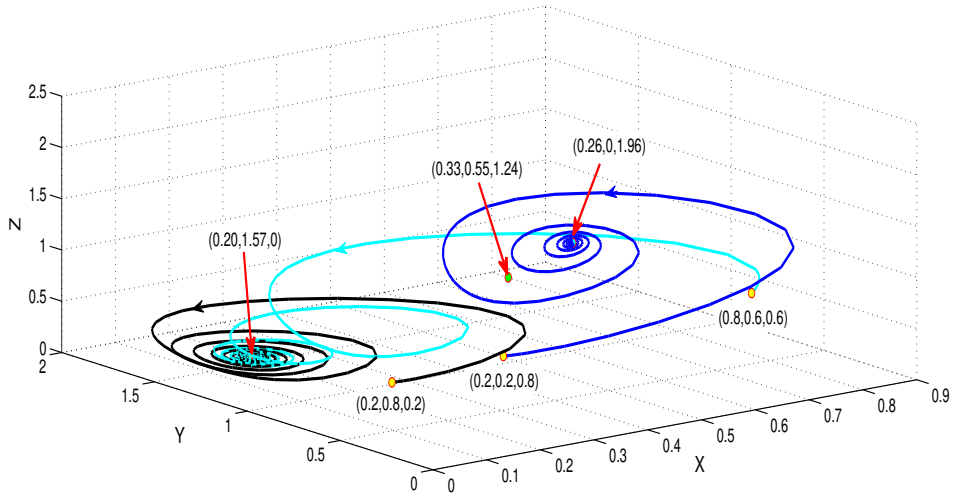

Figure 2. Effect of consumption parameter on the system.

are equilibrium points of our model system. The corresponding eigenvalues are $-0.1000, -0.1000, 0.8000$; $-0.8000, 2.3495, 1.8365$; $-0.0163 \pm 0.2765i, -0.0977$; $-0.0205 \pm 0.2746i, -0.0694$ and $-0.0258 \pm 0.3238i, -0.0008$. Out of these points E_2, E_3 and E^* are stable. Fig. 2 and Fig. 3 are the graphical representation of our analysis based on the set of parameters of **simulation 2**. We found that the initial value and the transmission coefficient ($\widehat{\beta}_1$, and $\widehat{\beta}_2$) are sensitive issues in this system. Due to the change in $\widehat{\beta}_1$, Fig. 2 shows a change compared to Fig. 1 for the same initial condition. We notice another change in Fig. 3 compared to Fig. 2 for different initial conditions and the same parameter values.

To study the effect of the competition coefficient ($\widehat{\delta}_1$ and $\widehat{\delta}_2$) on the model, we change the value of the parameter $\widehat{\delta}_1$ in **simulation 3** compared to **simulation 1**. For the parameter set of **simulation 3** $E_0\,(0,0,0)$, $E_1\,(5,0,0)$, $E_2\,(0.2582, 1.9589, 0)$, $E_3\,(0.2582, 0, 1.9589)$ and $E^*\,(0.3899, 1.0418, 0.8627)$ are the equilibrium points of our model.
And the corresponding eigenvalues are $-0.1000, -0.1000, 0.8000$; $-0.8000, 1.8365, 1.8365$; $-0.0207 \pm$

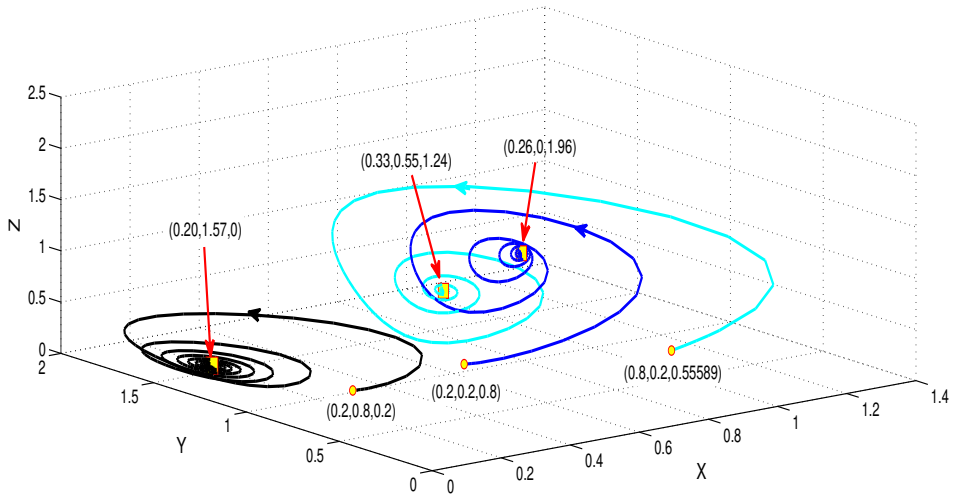

Figure 3. Dynamical behaviour for the equilibrium points.

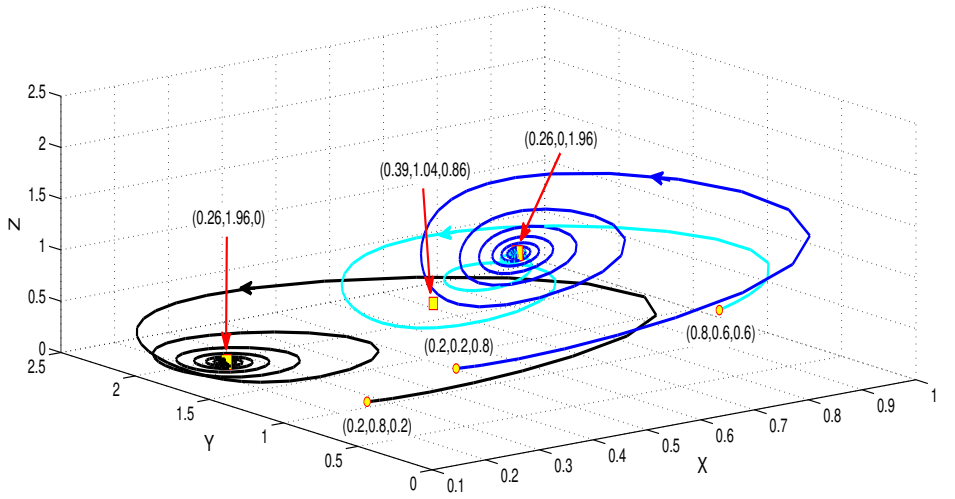

Figure 4. Effect of the competition parameter on the model.

$0.2747i, -0.0960$; $-0.0207 \pm 0.2747i, -0.1159$ and $-0.0281 \pm 0.3360i, -0.0061$.

Among these points, we identify three equilibrium points, namely E_2, E_3, and E^*, with stable dynamics. The graphical representation of our findings based on the set of parameters used in **simulation 3** is presented in Figs. 4 and 5. Our analysis reveals that the initial values of the competition coefficients ($\widehat{\delta}1$ and $\widehat{\delta}2$) are critical determinants of the behavior of the system. Specifically, even slight changes in $\widehat{\delta_1}$ can significantly alter the system's dynamics, as evident from the comparison between Figs. 1 and 4 for the same initial conditions. Furthermore, we observe another significant change in Fig. 5 compared to Fig. 4 when there is a change in the initial state. These findings highlight the importance of carefully selecting and monitoring initial conditions and competition coefficients in ecological systems to ensure their long-term sustainability. Here, we explore the impact of varying the values of the parameter p on the equilibrium points of the model system. The interior equilibrium points, the corresponding eigenvalues, and the equilibrium characteristics for different values of p are presented in Table 3, based on the parameters used in

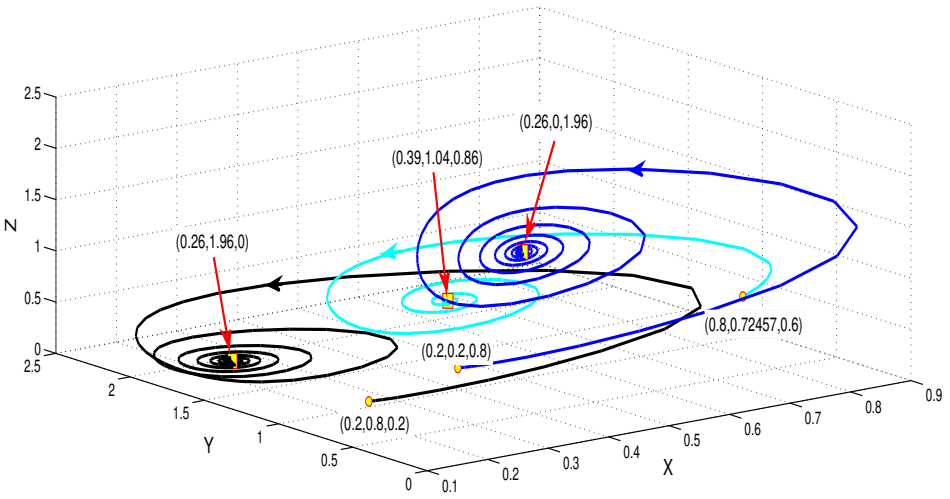

Figure 5. Dynamical behaviour for the equilibrium points.

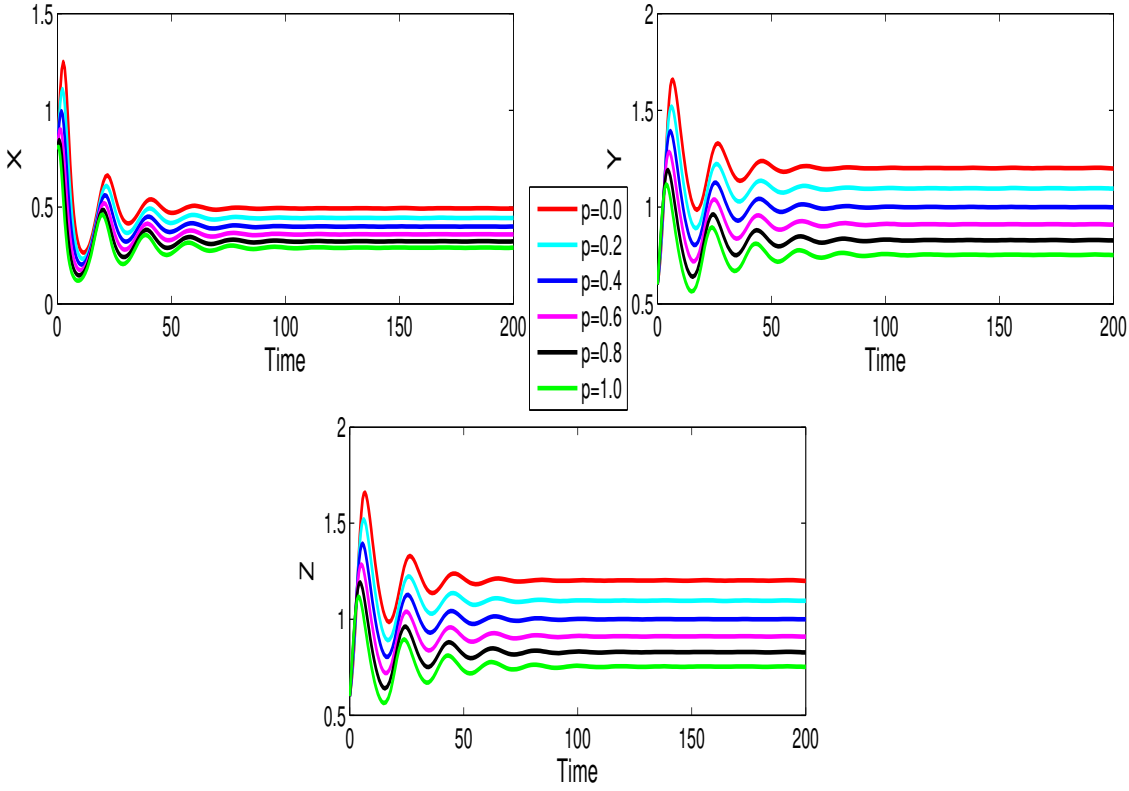

Figure 6. Time history for different value of p.

simulation 4. The results reveal that as p increases, the equilibrium population levels of both the prey and predator species exhibit a gradual decline. This finding suggests that changes in the parameter p have a significant impact on the stability and behavior of the model system.

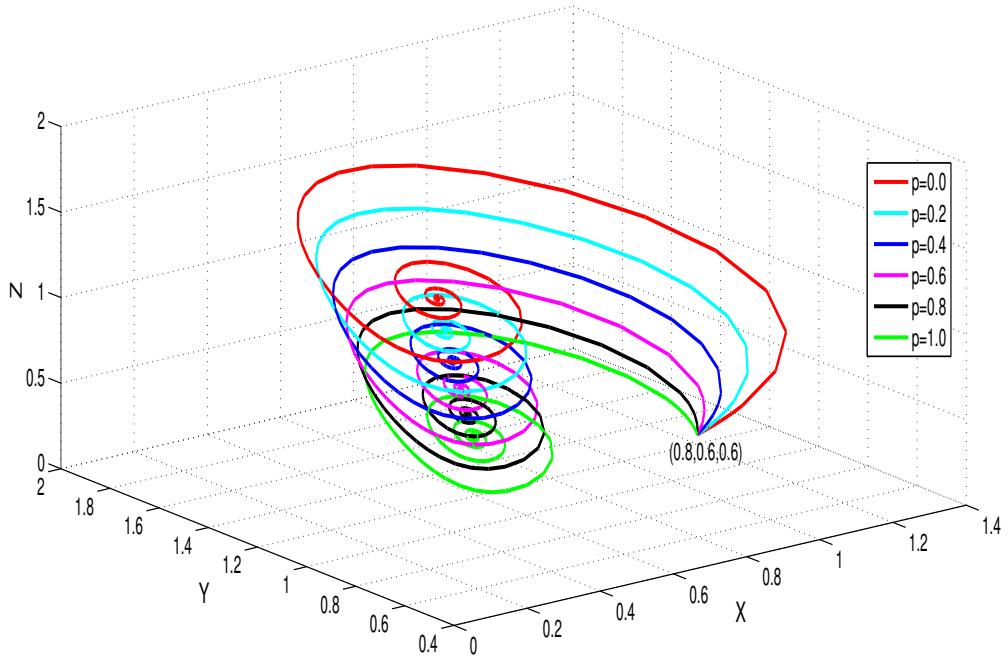

Figure 7. Phase portrait for different value of p.

Table 3. Equilibrium points, eigenvalues, and their nature for different p values.

p	Equilibrium	Eigenvalue	Nature
0	$(0.49356, 1.2017, 1.20172)$	$-0.0386 \pm 0.3278i, -0.0017$	Stable
0.2	$(0.44416, 1.09690, 1.09690)$	$-0.0348 \pm 0.3294i, -0.0015$	Stable
0.4	$(0.39957, 1.00006, 1.00006)$	$-0.0313 \pm 0.3307i, -0.0013$	Stable
0.6	$(0.35934, 0.91083, 0.91083)$	$-0.0282 \pm 0.3317i, -0.0011$	Stable
0.8	$(0.32309, 0.82880, 0.82880)$	$-0.0254 \pm 0.3325i, -0.0010$	Stable
1	$(0.29042, 0.75353, 0.75353)$	$-0.0228 \pm 0.3330i, -0.0009$	Stable

In this study, we analyze the population dynamics of prey and predator species over time, starting with initial population values of $X = 0.8$ (prey), $Y = 0.6$ (first predator), and $Z = 0.6$ (second predator), for various values of $p \in [0, 1]$. The results are presented in Fig. 6, while the corresponding phase portrait is depicted in Fig. 7. From these figures, it is evident that an increase in the value of p is associated with a gradual decrease in population density. These findings provide valuable information on the sensitivity of the model system to changes in parameter values and highlight the importance of understanding the underlying mechanisms that govern predator-prey interactions.

6 Conclusion

In this article, we have presented a three-species prey-predator model that incorporates imprecise biological parameters using the concept of interval numbers. Through the analysis of the model, we have demonstrated that the interval number method is a simple and effective tool for examining the impact of imprecise parameters on the behavior of the system.

Our analysis included checking the positivity and boundedness of the model, as well as performing a stability analysis of the five equilibrium points. The results of our analysis provide valuable insights into the dynamics of the prey-predator system and the effects of imprecision in the parameters.

In conclusion, our work highlights the importance of considering imprecision in biological parameters when modeling ecological systems. The interval number method provides a powerful approach to this challenge, enabling researchers to better capture the complexity of ecological systems and make more accurate predictions about their behavior. We believe that our findings will be of significant value to researchers working in the field of ecological modeling and contribute to the development of more accurate and reliable models of complex ecological systems.

Declarations

Consent for publication

Not applicable.

Conflicts of interest

The authors declare that they have no conflict of interest.

Funding

Not applicable.

Author's contributions

D.G.: Conceptualization, Methodology, Investigation, Writing-Original draft. P.K.S.: Conceptualization, Investigation, Software, Writing-Original draft, Supervision. G.S.M.: Visualization, Writing-Reviewing and Editing, Supervision. All authors discussed the results and contributed to the final manuscript.

Acknowledgements

Not applicable.

References

[1] Dubey, B., & Upadhyay, R.K. Persistence and extinction of one-prey and two-predators system. *Nonlinear Analysis: Modelling and Control*, 9(4), 307-329, (2004). [CrossRef]

[2] Gao, Y., & Yang, F. Persistence and extinction of a modified Leslie–Gower Holling-type II two-predator one-prey model with Lévy jumps. *Journal of Biological Dynamics*, 16(1), 117-143, (2022). [CrossRef]

[3] Gakkhar, S., Singh, B., & Naji, R.K. Dynamical behavior of two predators competing over a single prey. *BioSystems*, 90(3), 808-817, (2007).[CrossRef]

[4] Lv, S., & Zhao, M. The dynamic complexity of a three species food chain model. *Chaos, Solitons & Fractals*, 37(5), 1469-1480, (2008). [CrossRef]

[5] Gholami, M., Ghaziani, R.K., & Eskandari, Z. Three-dimensional fractional system with the stability condition and chaos control. *Mathematical Modelling and Numerical Simulation With Applications*, 2(1), 41–47, (2022). [CrossRef]

[6] Mukherjee, D. Effect of fear on two predator-one prey model in deterministic and fluctuating environment. *Mathematics in Applied Sciences and Engineering*, 2(1), 1-71, (2021). [CrossRef]

[7] Mulugeta, B. T., Yu, L., & Ren, J. Bifurcation Analysis of a One-Prey and Two-Predators Model with Additional Food and Harvesting Subject to Toxicity. *International Journal of Bifurcation and Chaos*, 31(6), 2150089, (2021). [CrossRef]

[8] Sarwardi, S., Mandal, P.K., & Ray, S. Dynamical behaviour of a two-predator model with prey refuge. *Journal of Biological Physics*, 39(4), 701-722, (2013). [CrossRef]

[9] Alebraheem, J., & Abu-Hasan, Y. Persistence of predators in a two predators-one prey model with non-periodic solution. *Applied Mathematical Sciences*, 6(19), 943-956, (2012).

[10] Savitri, D., Suryanto, A., & Kusumawinahyu, W.M. Dynamical behavior of a modified leslie-gower one prey-two predators with competition. *Mathematics*, 8(5), 699, (2020). [CrossRef]

[11] Kharbanda, H., & Kumar, S. Asymptotic stability of one prey and two predators model with two functional responses. *Ricerche Di Matematica*, 68(2), 435–452, (2019). [CrossRef]

[12] Pal, D., Santra, P., & Mahapatra, G.S. Dynamical behavior of three species predator-prey system with mutual support between non refuge prey. *Ecological Genetics and Genomics*, 3(5), 1-6, (2017). [CrossRef]

[13] Vijaya, S., & Rekha, E. Prey–predator three species model using predator harvesting Holling type II functional. *Biophysical Reviews and Letters*, 11(2), 87-104, (2016). [CrossRef]

[14] Laurie, H., & Venturino, E. A two-predator one-prey model of population dynamics influenced by herd behaviour of the prey. *Theoretical Biology Forum*, 111(1–2), 27–47, (2019). [CrossRef]

[15] Wang, J., & Wang, M. Boundedness and global stability of the two-predator and one-prey models with nonlinear prey-taxis. *Zeitschrift Fur Angewandte Mathematik Und Physik*, 69(3), (2018). [CrossRef]

[16] Pal, D., Mahapatra, G.S. Dynamic behavior of a predator–prey system of combined harvesting with interval-valued rate parameters. *Nonlinear Dynamics*, 83(4), 2113–2123, (2016). [CrossRef]

[17] Pal, D., Mahaptra, G.S., Samanta, G.P. Optimal harvesting of prey-predator system with interval biological parameters: A bioeconomic model. *Mathematical Biosciences*, 241(2), 181–187, (2013). [CrossRef]

[18] Santra, P.K. & Mahapatra, G.S. Dynamical study of discrete-time prey-predator model with constant prey refuge under imprecise biological parameters. *Journal of Biological Systems*, 28(3), 681–699, (2020). [CrossRef]

[19] Ghosh, D., Santra, P.K., & Mahapatra, G.S. Fear effect on a discrete-time prey predator model with imprecise biological parameters. *In AIP Conference Proceedings (Vol. 2246), American Institute of Physics Inc.* (2020). [CrossRef]

[20] Santra, P., & Mahapatra, G.S. Discrete prey–predator model with square root functional response under imprecise biological parameters.*In Springer Proceedings in Mathematics and Statistics, Springer*, 320, 211–225, (2020). [CrossRef]

[21] Mondal, B., Rahman, M.S., Sarkar, S., & Ghosh, U. Studies of dynamical behaviours of an imprecise predator-prey model with Holling type II functional response under interval uncertainty. *European Physical Journal Plus*, 137(1), (2022). [CrossRef]

[22] Mahata, A., Mondal, S.P., Roy, B., & Alam, S. Study of two species prey-predator model in imprecise environment with MSY policy under different harvesting scenario. *Environment, Development & Sustainability*, 23(10), 14908–14932, (2021). [CrossRef]

[23] Vargas-De-León, C. On the global stability of SIS, SIR and SIRS epidemic models with standard incidence. *Chaos, Solitons and Fractals*, 44(12), 1106–1110, (2011). [CrossRef]

[24] Beretta, E. & Capasso, V. On the general structure of epidemic systems. *Global asymptotic stability, Computers & Mathematics with Applications*, 12(6), 677–694, (1986). [CrossRef]

[25] Korobeinikov, A. & Wake, G.C. Lyapunov functions and global stability for SIR, SIRS, and SIS epidemiological models. *Applied Mathematics Letters*, 15(8), 955–960, (2002). [CrossRef]

[26] Goh, B.S. Global stability in two species interactions. *Journal of Mathematical Biology*, 3(3–4), 313–318, (1976). [CrossRef]

[27] Korobeinikov, A. Lyapunov functions and global properties for SEIR and SEIS epidemic models. *Mathematical Medicine and Biology*, 21(2), 75–83, (2004). [CrossRef]

[28] McCluskey, C.C. Lyapunov functions for tuberculosis models with fast and slow progression. *Mathematical Biosciences and Engineering*, 3(4), 603–614, (2006). [CrossRef]

Mathematical Modelling and Numerical Simulation with Applications (MMNSA)
(https://dergipark.org.tr/en/pub/mmnsa)

How to cite this article: Ghosh, D., Santra, P.K. & Mahapatra, G.S. (2023). A three-component prey-predator system with interval number. *Mathematical Modelling and Numerical Simulation with Applications*, 3(1), 1-16. https://doi.org/10.53391/mmnsa.1273908

Mathematical Modelling and Numerical Simulation with Applications, 2023, 3(1), 17–32

https://dergipark.org.tr/en/pub/mmnsa

ISSN Online: 2791-8564 / Open Access

https://doi.org/10.53391/mmnsa.1273945

RESEARCH PAPER

Finite volume simulation of calcium distribution in a cholangiocyte cell

Nakul Nakul [1,‡], **Vedika Mishra** [1,*,‡] **and Neeru Adlakha** [1,‡]

[1]Department of Mathematics and Humanities, SVNIT, Surat, 395007, Gujarat, India

*Corresponding Author

‡i17ma040@amhd.svnit.ac.in (Nakul Nakul); d20ma001@amhd.svnit.ac.in (Vedika Mishra); nad@amhd.svnit.ac.in (Neeru Adlakha)

Abstract

Cholangiocytes are the cells of the liver having a major role in the conditioning of bile used in digestion. Other functions of cholangiocytes are in apoptosis and bicarbonate secretion. The Calcium in the intracellular environment of various cells including cholangiocytes regulates a large number of functions. This regulating mechanism in cholangiocytes has been poorly understood to date. In order to analyze the calcium regulation in cholangiocyte cells, a mathematical model for a one-dimensional steady-state case is constructed in this study. This involves a non-linear reaction-diffusion equation with appropriate boundary conditions. The influx from IP_3 receptor, ryanodine receptor (RYR), and plasma membrane as well as the efflux of calcium from SERCA pump and plasma membrane have been employed in the model. The finite volume method and Newton-Raphson method have been used to solve the problem. Numerical findings have been used to examine the effects of parameters like diffusion coefficient, rate of SERCA pump efflux, buffer, and influx from plasma membrane on calcium concentration in cholangiocyte cells. The information generated from the model can be useful for understanding the mechanism of cholestatic disorders which can be further useful in the diagnosis and treatment of these disorders.

Keywords: Liver; reaction-diffusion equation; calcium; finite volume method; Newton-Raphson method

AMS 2020 Classification: 65N08; 92-10; 35-04; 92C37

1 Introduction

The largest organ in the body is the liver. The liver is located just above the stomach and below the diaphragm in the upper right abdomen. Liver weighs about 838 to 2584 grams, is reddish brown in colour and is slightly conical shaped. This organ is extra soft and fleshy. It is the only organ that can completely regenerate from a small part of itself [1, 2]. Liver cells are classified into

➤ **Received:** 30.01.2023 ➤ **Revised:** 15.03.2023 ➤ **Accepted:** 18.03.2023 ➤ **Published:** 31.03.2023

two categories viz Parenchymal cells and Non-Parenchymal cells. The Parenchymal cells of the liver are hepatocytes. Hepatocyte cells are cubical epithelial cells. This cell lines the sinusoids and makes up to 70% of cells in the liver. Cells within the liver that are not hepatocytes are collectively called as Non- Parenchymal cells. These cells serve a wide variety of metabolic, immune, and structural functions [3]. The Non-Parenchymal cells line up the normal liver sinusoid consisting of four different types of cells which are kuffer, endothelial/cholangiocyte, pit and stallete/ito cells. These cells differ in origin, population kinetics, phenotypic and functional characteristics [4]. A network of bile ducts or cholangiocytes lines the biliary tree. These are a diverse and highly active group of epithelial cells. Cholangiocytes collect bile from bile canaliculi from the hearing canals of hepatocytes. Primitive bile is generated in hepatocytes. Bile reaches to the gallbladder, choledochal, and extrahepatic duct using a network of channels. Only 3-5 percent of the overall number of liver cells are cholangiocyte cells [5]. The ability of a cell to accept, process, and disseminate signals to its surrounding and with itself is known as 'cellular communication' or 'signaling' [6]. Ca^{2+} in the intracellular environment regulates a large number of functions like cell proliferation, apoptosis and secretion. The secretion of bile juice is one of the liver's most critical activities, it is the end consequence of hepatocytes producing bile whereas cholangiocytes condition it [6, 7]. When calcium is released from the endoplasmic reticulum (ER) through IP_3 receptors, inositol 1,4,5 triphosphate (IP_3) regulates calcium signaling in the cholangiocytes [8, 9]. Calcium signaling has been studied in various cells like neurons, oocytes, myocytes, astrocytes, pancreatic acinar cells, hepatocytes, etc. by various researchers [10–12, 15–25, 27]. Kotwani et al. constructed and simulated a one-dimensional unsteady state case mathematical model of calcium concentration in fibroblast cells using the finite difference approach [10]. Panday et al. constructed a model involving reaction-diffusion equations to study Ca^{2+} distribution in oocyte cells involving Na^+/Ca^{2+} exchanger and advection of calcium [11]. Naik et al. studied the calcium distribution involving voltage-gated calcium channels (VGCC), ryanodine receptors, and buffers in one, two and three dimensions for oocyte and T lymphocyte cells. They concluded that the increase of Ca^{2+} concentration due to RYR was higher than that of VGCC [12–14, 60, 62]. Introducing a two-dimensional discrete-time chemical model and the existence of its fixed points, the one and two-parameter bifurcations of the model were also investigated by them [61]. Jha et al. studied calcium distribution using the finite element approach in astrocytes [15]. An attempt was also made by them to consider a one-dimensional fractional diffusion equation to study the effects of buffers and endoplasmic reticulum on the calcium distribution profile in nerve cells [63].
Amrita et al. observed the effects of Na^+/Ca^{2+} exchanger, source geometry, leak, SERCA pump, etc. on Ca^{2+} oscillations in dendritic spines & neuron cells employing finite element approach [16–18]. Pathak et al. devised a mathematical model for calcium distribution in cardiac myocytes involving a pump, excess buffer and leaks [19]. Manhas et al. observed calcium variation in pancreatic acinar cells describing the effect of mitochondria on Ca^{2+} signaling [20–22]. Tewari et al. have constructed a model for neuron cells expressing the impact of sodium pump on Ca^{2+} oscillation and calcium diffusion with excess buffer [23, 24]. Jagtap et al. solved interdependent calcium and IP_3 dynamics involving calcium flux, calcium diffusion coefficient, and protein content in the cytoplasm [25]. They also solved the problem for calcium concentration fluctuation in two dimensions using the finite volume method for the unsteady state situation [26]. Hemant et al. formulated an unsteady state mathematical model in one dimension to explore the distribution of intracellular calcium in T lymphocyte cells. The model takes into account factors including buffers, ryanodine receptors (RyRs), source influx and diffusion coefficient [27]. Kothiya et al. provided a mathematical model to analyze the Ca^{2+} signaling to affect the synthesis of ATP and IP_3 in fibroblast cells [28, 29]. Bhardwaj et al. used a radial basis function-based differential quadrature method to examine the nonlinear spatiotemporal dynamics of Ca^{2+} in T cells while accounting for

the SERCA pump, ryanodine receptor, source amplitude, and buffers [30]. Pawar et al. studied interdependent calcium and IP_3 dynamics and their effects on nitric oxide production and β-amyloid production and degradation in neuron cells. They also simulated the interdependent dynamics of calcium with dopamine, nitric oxide and β- amyloid in neuron cells [49–53]. Joshi et al. presented a calcium dynamics model that firmly orchestrates exchanges of calcium flux through intracellular/extracellular sources of calcium to investigate cellular activities and calcium homeostasis using a generalized two-dimensional space-time reaction-diffusion model [56].
Protein and voltage-dependent calcium channels were also used to obtain an approximate Ca^{2+} profile by the fractional integral transform method [55]. A mathematical model of calcium was developed in the form of the Hilfer fractional reaction-diffusion equation to examine the calcium diffusion in the neuron cells. The effects of calcium-dependent protein and flux through the sodium-calcium exchanger were incorporated in the model [59]. Pankratova et al. employed bifurcation theory analysis and examined steady-state solutions, bistability, simple and complicated periodic limit cycles and also chaotic attractors for calcium variation in astrocytes [54]. Tarifa et al. demonstrated that preferential calcium release near the sarcolemma is key to a higher spatiotemporal distribution of sparks and amplitude of post-depolarizations in atrial myocytes from patients with atrial fibrillation using mathematical model [57]. Chang et al. developed a mathematical model of intracellular calcium dynamics for evaluating the combined anticancer effects of Afatinib and RP4010 in esophageal cancer [58].
Minagawa et al. have discussed that in almost every kind of cell, cytosolic Ca^{2+} is an essential second messenger. Furthermore, Ca^{2+} controls a variety of actions in individual cells. They looked at the cellular level machinery in cholangiocytes which is responsible for Ca^{2+} signaling. Two Ca^{2+} -mediated events have also been found in cholangiocytes which are apoptosis and bicarbonate secretion. They concluded that calcium signaling is responsible for therapeutically treating cholestatic disorders [31]. Nathanson et al. addressed the control of intracellular Ca^{2+} channel expression in cholangiocytes [32]. Woo et al. formulated a model of the human biliary system and found that the release of ATP is closely co-related with shear which is dependent on intracellular Ca^{2+} and becomes desensitized with repeated exposure to flow. Additionally, they found that activating membrane P2Y (Purinergic) receptors and ATP release both contribute to the increase in fluid flow's effect on Ca^{2+} [33]. Weerachayaphorn et al. explained that cholangiocyte abnormalities are the primary cause of the majority of cholestatic diseases. The inositol 1,4,5-triphosphate receptor (IP3R), an intracellular calcium release channel, is most frequently seen in cholangiocytes as its type 3 isoform. In individuals with cholestatic diseases, IP3R expression is decreased in the intrahepatic bile ducts, which are necessary for the bile ducts to secrete bicarbonate. It was also examined how the oxidative stress-sensitive nuclear factor erythroid 2-like 2 (NFE2L2 or NRF2) controls the expression of IP3R [34]. Ueasilamongkol et al. examined cholangiocarcinoma (the second most common kind of liver cancer) using the type 3 variant of the inositol 1,4,5-triphosphate receptor [35]. Shibao et al. examined the effects of the inositol 1,4,5-triphosphate receptor (IP3R) (Ca^{2+} release channel) in cholestasis-related animal models and patients on ductular secretion and Ca^{2+} signaling [36]. Rodrigues et al. analyzed the mechanisms underlying Ca^{2+} signals in cholangiocyte cells and used the experimental approaches to find cholangiocyte Ca^{2+} signaling. The role of Ca^{2+} in the regular and abnormal control of secretion and apoptosis in cholangiocytes was also explored [37]. Masyuk et al. explored the idea that the sensory organelles known as cholangiocyte cilia gather up and transmit information from luminal bile flow into intracellular Ca^{2+} and adenosine $3^{'}$, $5^{'}$ cAMP (cyclic adenosine monophosphate) signaling [38]. Marzioni et al. examined to see if glucagon-like peptide-1 modifies the biological response of cholangiocytes to cholestasis [39]. Martin et al. suggested that the loss of IP3Rs may be the most widely used cause of cholestasis. It seems crucial for healthy bile secretion in the liver

that IP3R-mediated Ca^{2+} signaling occurs in bile duct epithelia [40]. Maroni et al. determined that cholangiocytes react to injury by secreting a number of peptides, acquiring a neuroendocrine-like character. These substances alter cholangiocyte biology and control the progression of biliary injury through an autocrine/paracrine mechanism.
Cholangiopathies, a class of illnesses that targets biliary cells exclusively, are thought to progress more slowly as a result of the failure of such mechanisms [41]. Lazaridis et al. discussed the various diseases occurring in cholangiocytes such as inflammation, cholestasis, apoptotic death, and ductopenia, etc. due to dysregulation in calcium signaling [42]. Jung et al. explained the cAMP-induced processes in epithelial cells work in conjunction with calcium signaling to control membrane transport proteins and play a role in bicarbonate secretion [43]. Guerra et al. discussed the molecular processes that control cholangiocytes' bile production. Furthermore, there is evidence that certain cholestatic disorders of the bile ducts modify several aspects of the Ca^{2+} signaling system, including the cholangiocytes's regulation of the expression of intracellular Ca^{2+} channels [44]. Amaya et al. investigated the evidence indicating cholangiocyte Ca^{2+} signaling defects are a major factor in the development of cholestatic diseases characterized by decreased hepatic bile secretion [45]. Shin et al. found that anion channels can equally fulfill a variety of physiological functions including regulation of neuronal excitability and secretion of epithelial fluid [46]. Alpini et al. suggested that a special absorption mechanism must exist in cholangiocytes for bile acid activity. Simultaneously cholangiocytes express a bile acid transporter [47]. A good number of investigations is reported on calcium distribution in various cells like neurons, oocytes, pancreatic acinar cells, hepatocytes, etc mostly using linear reaction-diffusion equations. Most of the investigations of calcium distribution in cells of the liver are reported for hepatocyte cells. But very little attention has been paid to understanding the calcium distribution patterns in cholangiocyte cells and that too is mostly experimental.
None of the theoretical studies on calcium distribution patterns in cholangiocyte cells have explored the role of buffers, SERCA pump, efflux, influxes, etc. Therefore the mechanisms of calcium signaling regulating the functions of cholangiocyte cells are not well understood to date. The insights of these mechanisms will be useful in understanding the processes leading to cholestasis diseases. In view of the above, the present study is focused on developing a mathematical model of calcium distribution in cholangiocyte cells. A nonlinear steady-state reaction-diffusion model of calcium ions in cholangiocyte cells is proposed by incorporating parameters like buffer, SERCA pump, influxes, efflux, etc. The numerical simulation is performed using the Finite Volume method and Newton Raphson method to analyze the effects of these parameters on calcium signaling in cholangiocyte cells.

2 Mathematical formulation of the problem

Mathematical modelling plays a key role in finding solutions to many real-world problems. The experimental approaches are very tedious and time-consuming therefore scientists prefer to make use of computational approaches for solving the problems. The computational approaches are congenial and hence adaptable. In the present study, the mathematical model and the solution of Ca^{2+} signaling in cholangiocyte cell is presented.
The reaction-diffusion equation for Ca^{2+} distribution in steady state for cholangiocyte is given by [48].

$$D_{Ca}\frac{\partial^2[Ca^{2+}]}{\partial x^2} + J_{IP3R} + J_{RYR} - J_{SERCA} + J_{IN} - J_{out} - k^+[B]_\infty([Ca^{2+}] - C_\infty) = 0. \tag{1}$$

D_{Ca} represents diffusion coefficient, k^+ represents buffer association rate, $[B]_\infty$ represents buffer

concentration at equilibrium, $[Ca^{2+}]_\infty$ represents calcium concentration at equilibrium, J_{IPR} represents influx from IP_3 receptor, J_{RYR} represents influx from ryanodine receptor, J_{SERCA} represents efflux into ER, J_{IN} represent influx from plasma membrane, J_{out} represent outflux from plasma membrane.
The fluxes are modelled as,

$$J_{IP3R} + J_{RYR} = k_1(T + T_0)(C_e - [Ca^{2+}]), \tag{2}$$

where T indicates the basal fractional activity of the channels in the store, T_0 represents the calcium release rate from the store and k_1 denotes the rate of calcium release from the store.

$$J_{IN} = k_5(T + T_0)(C_{out} - [Ca^{2+}]), \tag{3}$$

k_5 represents external medium calcium influx and C_{out} represents extracellular calcium concentration.

$$J_{out} = \frac{V_6[Ca^{2+}]^2}{k_7^2 + [Ca^{2+}]^2}, \tag{4}$$

The plasma membrane pump's maximal rate is represented by V_6 and its dissociation constant is represented by k_7.

$$J_{SERCA} = \frac{V_{serca}[Ca^{2+}]^2}{k_4^2 + [Ca^{2+}]^2}, \tag{5}$$

V_{serca} represents the maximum rate of calcium pumping into the store and k_4 represents the storage calcium pump's dissociation constant.
Calcium concentration in ER can be replaced by,

$$C_e = \frac{(C_T - V_c)[Ca^{2+}]}{V_e}, \tag{6}$$

C_T represents calcium concentration in cell and C_e represent the calcium in ER.

Boundary condition: It is assumed that the influx source channel is present at $x = 0$. Therefore, the following flux condition is enforced:

$$lim_{x\to 0}\left(-D_{Ca}\left(\frac{\partial[Ca^{2+}]}{\partial x}\right)\right) = \sigma_{Ca}, \tag{7}$$

σ_{Ca} represents source influx [25]. The other end of the cell $(x = 10)$ is assumed to be at rest. Therefore, a constant resting calcium concentration is assumed as given below:

$$lim_{x\to 10}([Ca^{2+}]) = C_\infty = 0.1\mu M, \tag{8}$$

Solution: The cytosol of the cholangiocyte cell is split into 20 nodes. By putting all the various

fluxes in Eq. (1), it can be rewritten as

$$D_{Ca}\frac{\partial^2[Ca^{2+}]}{\partial x^2} - k^+[B]_\infty([Ca^{2+}] - C_\infty) + k_1(T+T_0)\left(\frac{(C_T - V_c)[Ca^{2+}]}{V_e} - [Ca^{2+}]\right) + k_5(T+T_0)(C_{out} - [Ca^{2+}]) - \frac{V_{serca}[Ca^{2+}]^2}{k_4^2 + [Ca^{2+}]^2} - \frac{V_6[Ca^{2+}]^2}{k_7^2 + [Ca^{2+}]^2} = 0. \tag{9}$$

Representing calcium concentration in the cytosol of the cell ($[Ca^{2+}]$) by u, Eq. (9) can be written as,

$$D_{Ca}\frac{\partial^2 u}{\partial x^2} + k_1(T+T_0)\left(\frac{(C_T - V_c)u}{V_e} - u\right) + k_5(T+T_0)(C_{out} - u) - \frac{V_{serca}u^2}{k_4^2 + u^2} - \frac{V_6 u^2}{k_7^2 + u^2} - k^+[B]_\infty(u - C_\infty) = 0, \tag{10}$$

In general, Eq. (10) can be written as,

$$\frac{\partial^2 u}{\partial x^2} - au + c - \frac{V_{serca}u^2}{k_4^2 + u^2} - \frac{V_6 u^2}{k_7^2 + u^2} = 0, \tag{11}$$

a and c are given as,

$$a = \frac{k^+[B]_\infty + \frac{k_1(T+T_0)(V_c+V_e)}{V_e} + k_5(T+T_0)C_{out}}{D_{Ca}}, \tag{12}$$

$$c = \frac{k^+[B]_\infty C_\infty + \frac{k_1(T+T_0)C_T}{V_e} + k_5(T+T_0)}{D_{Ca}}. \tag{13}$$

To solve Eq. (11) finite volume method is employed. For the first term in Eq. (11), a linear profile assumption is taken for calcium concentration, and for the rest of the term, a constant profile assumption is taken. On integrating from w to e over control volumes,

$$\left(\frac{\partial u}{\partial x}\right)_e - \left(\frac{\partial u}{\partial x}\right)_w - au_G\delta x + c\delta x - \frac{V_{serca}u^2}{k_4^2 + u^2} - \frac{V_6 u^2}{k_7^2 + u^2} = 0, \tag{14}$$

where u_G represents calcium concentration at the centroid point for any element.
For first control volume (n=1) Eq. (11) can be written as,

$$\left(\frac{\partial u}{\partial x}\right)_e + \frac{\sigma_{Ca}}{D_{Ca}} - au_G\delta x + c\delta x - \frac{V_{serca}u^2}{k_4^2 + u^2} - \frac{V_6 u^2}{k_7^2 + u^2} = 0. \tag{15}$$

Since linear profile assumption is taken for calcium concentration for the first term in Eq. (8), Eq. (12) can be rewritten as

$$\frac{u_E - u_G}{\delta x} + \frac{\sigma_{Ca}}{D_{Ca}} - au_G\delta x + c\delta x - \frac{V_{serca}u^2}{k_4^2 + u^2} - \frac{V_6 u^2}{k_7^2 + u^2} = 0. \tag{16}$$

After rearranging the terms,

$$\left(\frac{1}{\delta x}+a\delta x\right)u_G=\frac{1}{\delta x}u_E+\frac{\sigma_{Ca}}{D_{Ca}}+c\delta x-\frac{V_{serca}u^2}{k_4^2+u^2}-\frac{V_6u^2}{k_7^2+u^2}. \tag{17}$$

For last control volume (n=20), u_E is 0.1 μM (C_∞)

$$\frac{u_E-u_G}{\delta x}-\frac{u_G-u_w}{\delta x}-au_G\delta x+c\delta x-\frac{V_{serca}u^2}{k_4^2+u^2}-\frac{V_6u^2}{k_7^2+u^2}=0, \tag{18}$$

$$\left(\frac{2}{\delta x}+a\delta x\right)u_G=\frac{1}{\delta x}u_w+c\delta x+\frac{C_\infty}{\delta x}-\frac{V_{serca}u^2}{k_4^2+u^2}-\frac{V_6u^2}{k_7^2+u^2}. \tag{19}$$

For intermediate control volumes (n=2 to 19),

$$\frac{u_E-u_G}{\delta x}-\frac{u_G-u_w}{\delta x}-au_G\delta x+c\delta x-\frac{V_{serca}u^2}{k_4^2+u^2}-\frac{V_6u^2}{k_7^2+u^2}=0, \tag{20}$$

it is rewritten as,

$$\left(\frac{2}{\delta x}+a\delta x\right)u_G=\frac{1}{\delta x}u_E+\frac{1}{\delta x}u_w+c\delta x+\frac{C_\infty}{\delta x}-\frac{V_{serca}u^2}{k_4^2+u^2}-\frac{V_6u^2}{k_7^2+u^2}. \tag{21}$$

The resulting system of nonlinear equations is resolved using Newton Raphson's method.

3 Results and discussion

The following physiological parameters are used for solving the formulated problem in Eq. (11).

Table 1. Parameters of physiology affecting calcium variation [16, 26]

Symbol	Parameter	Value
D_{Ca}	Calcium's diffusion coefficient	50 μ m^2sec^{-1}
k_1	Rate of calcium release from store	7.5 sec^{-1}
K_2	Buffer association rate	300 $\mu^{-1}M^{-1}sec^{-1}$
V_{serca}	Store pump dissociation constant	0.65 $\mu Msec^{-1}$
k_4	The storage calcium pump's dissociation constant	0.1 μM
k_5	Calcium influx rate from the external medium	0.000158 sec^{-1}
V_6	Plasma membrane pump's maximum rate	2 µM/s $\mu Msec^{-1}$
k_7	Plasma membrane pump's dissociation constant	0.6 μM
C_{out}	Calcium concentration of extracellular medium	2 μM
T_0	The store's channel's baseline fractional activity	0.2
T	Activity on the store's channels in fractions	0.8
C_T	Total $[Ca^{2+}]$ relative to cell volume	2 μM
k^+	Association rate of buffer	1.5 $\mu M^{-1}sec^{-1}$
V_c	Volume of the cytosol to the total cell volume ratio	0.83
V_e	Ratio of Volume of ER to total volume of cell	0.3
C_∞	Calcium concentration at Equilibrium	0.1 μM

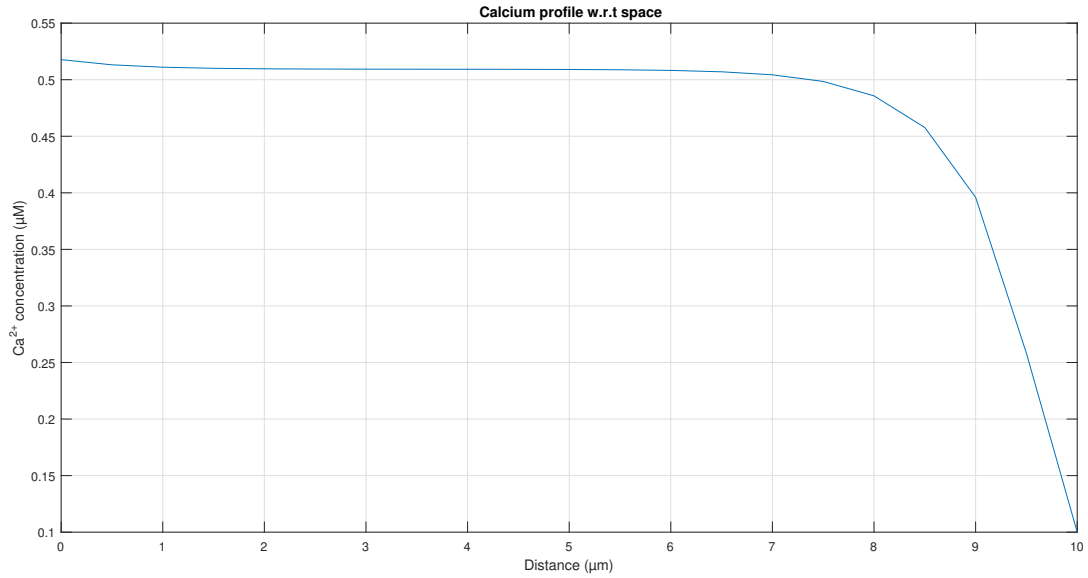

Figure 1. Calcium variation in cholangiocyte cell with respect to space

Figure 1 shows the calcium variation in a cholangiocyte cell with respect to space for diffusion coefficient 50 $\mu m^2 sec^{-1}$, source influx 1 pA and buffer 5 μM. By carefully studying the above graph, it shows that near the source, there was the highest concentration of calcium $\approx$ 0.53 μM. The calcium concentration continuously decreases until it reaches to its equilibrium value i.e. 0.1 μM, away from the source. The graph shows the non-linear behaviour of the calcium concentration pattern between x= 7 to 9 μm. This may be due to major imbalances among biophysical processes like diffusion, buffering, efflux, and influxes which is clear from the major difference in calcium concentration at x=7 μm and x=9 μm. The sharp fall from x=9 to x= 10 μm indicates the major role of buffering and calcium-reducing mechanisms in this area.

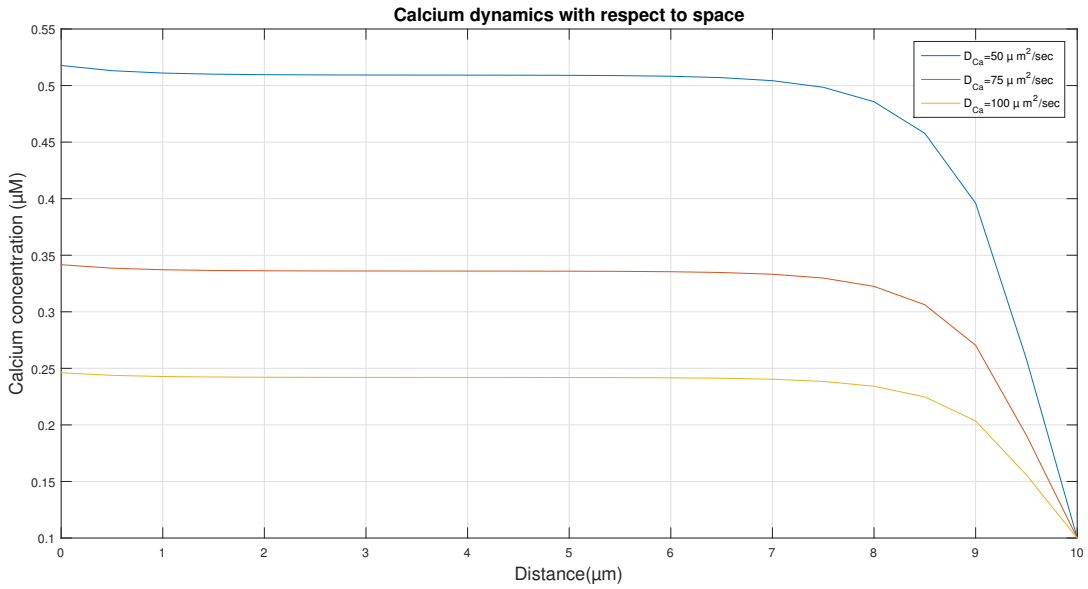

Figure 2. Cholangiocyte cell calcium change for various diffusion coefficient values with regard to space

Figure 2 shows the calcium variation with respect to space for source influx 1 pA, buffer 5 μM and diffusion coefficient 50 $\mu m^2 sec^{-1}$, 75 $\mu m^2 sec^{-1}$ and 100 $\mu m^2 sec^{-1}$. It can be observed from the figure that as the diffusion coefficient increases calcium concentration starts decreasing. This fall in calcium concentration with the increase in diffusion coefficient from $x = 0$ to $x = 9$ μm implies that the higher quantity of calcium is diffusing from the source towards the other end of the cell for higher rates of diffusion which further activates and increases the role of calcium reducing mechanisms like buffering etc. in the whole cell. The maximum value for calcium concentration is around 0.55 μM and the minimum value is 0.25 μM. Non-linear behaviour is the same as Figure 1. Moving away from the source calcium concentration starts decreasing gradually and it attains its equilibrium concentration 0.1 μM.

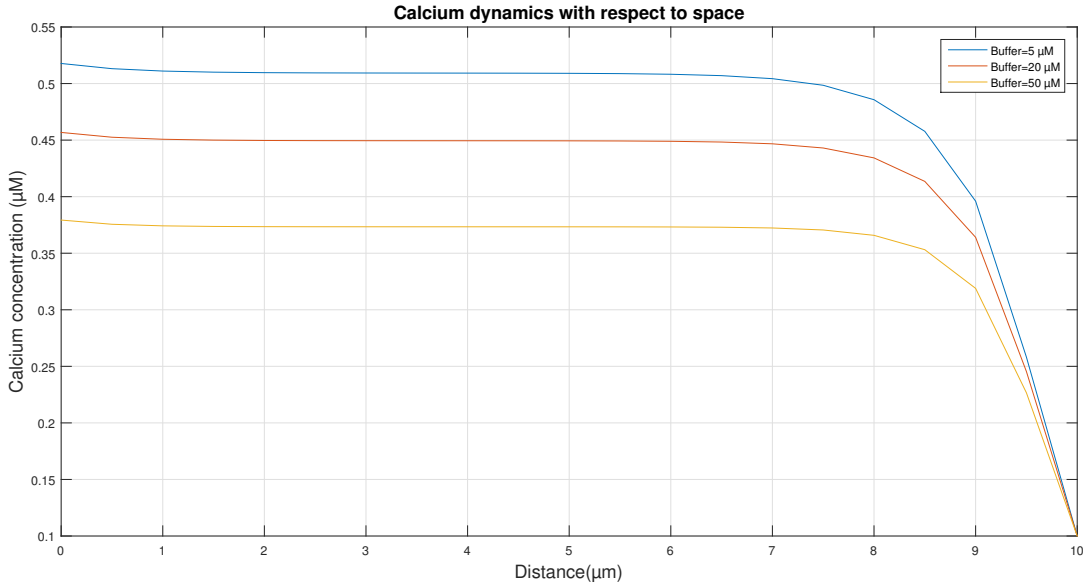

Figure 3. Calcium variation in cholangiocyte cell with respect to space for different value of buffer

Figure 3 shows the calcium concentration variation with respect to space for source influx 1 pA, buffer 5 μM, 20 μM and 50 μM and diffusion coefficient 50 $\mu m^2 sec^{-1}$. It can be observed from the figure as the buffer value increases calcium concentration starts decreasing. Free buffer binds with free calcium and forms calcium-bound buffer which decreases free calcium concentration. The maximum value for calcium concentration is around 0.55 μM and the minimum value is 0.38 μM. Non-linear behaviour is the same as Figure 1. Moving away from the source calcium concentration starts decreasing gradually and it attains its equilibrium concentration 0.1 μM.

Figure 4 shows the calcium variation with respect to space for source influx 1 pA , buffer 5 μM and diffusion coefficient 50 $\mu m^2 sec^{-1}$. A comparative study has been done for the rate of calcium influx from plasma membrane k_1 = 5.5 sec^{-1}, 7.5 sec^{-1} and 15 sec^{-1}. It is evident from the graph that the concentration of calcium starts to increase as k_1 rises due to an increased influx of calcium from the plasma membrane. The maximum value for calcium concentration is around 0.95 μM and the minimum value is 0.38 μM. Non-linear behaviour is the same as Figure 1. Moving away from the source calcium concentration starts decreasing gradually and it attains its equilibrium concentration 0.1 μM.

Figure 5 shows the calcium concentration variation with respect to space for source influx 1 pA, buffer 5 μM and diffusion coefficient 50 $\mu m^2 sec^{-1}$. A comparative study has been done for the rate of calcium efflux to SERCA pump V_{serca} 0.5 $\mu Msec^{-1}$, 0.65 $\mu Msec^{-1}$ and 1 $\mu Msec^{-1}$. It is evident

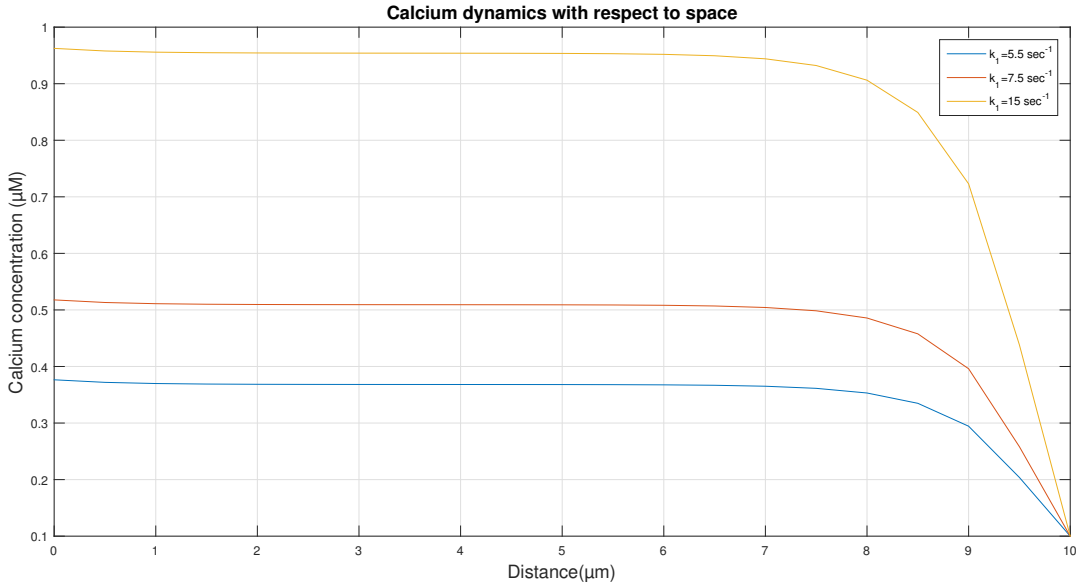

Figure 4. Calcium variation in cholangiocyte cell with respect to space for different value of k_1

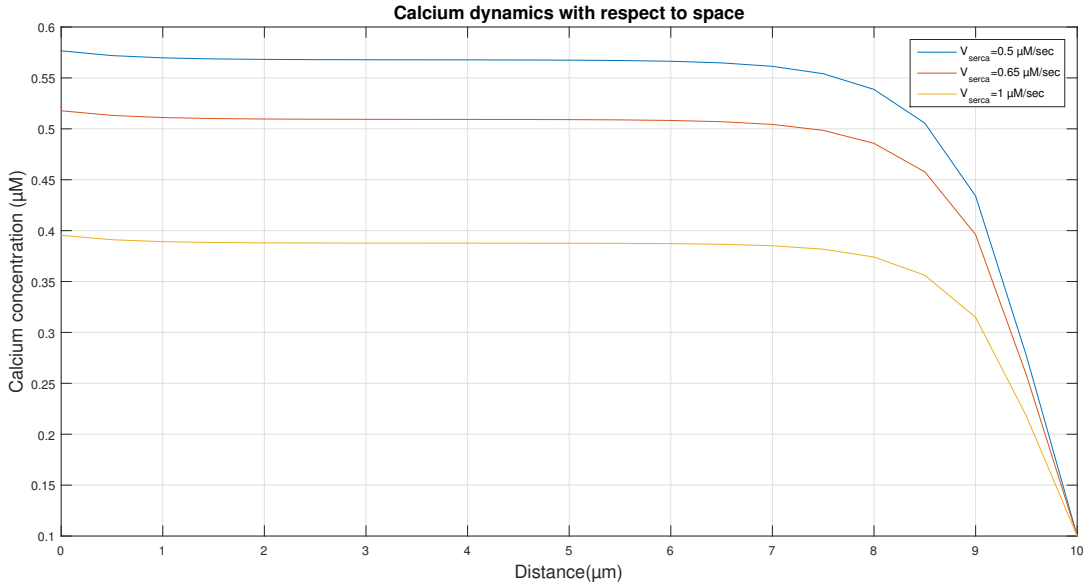

Figure 5. Calcium variation in cholangiocyte cell with respect to space for different values of V_{serca}

from the graph that the concentration of calcium starts to decrease as V_{serca} rises due to SERCA pump which takes calcium out of the cytosol. The maximum value for calcium concentration is around 0.58 μM and the minimum value is 0.4 μM. Non-linear behaviour is the same as Figure 1. Moving away from the source calcium concentration starts decreasing gradually and it attains its equilibrium concentration 0.1 μM.

4 Conclusion

A reaction-diffusion model of calcium distribution patterns in cholangiocyte cells in constructed for a one-dimensional steady-state case and successfully simulated to analyze the impacts of various parameters incorporated in the model. The finite volume method can be used on arbitrary geometries, using structured or unstructured meshes and it leads to robust schemes. It

is locally conservative because it is based on 'balance' approach. The combination of the finite volume method and Newton's method has been successfully employed for solving the non-linear reaction-diffusion of calcium in the cell. The proposed numerical strategy for the simulation of the proposed nonlinear model provides novel insights into calcium distribution patterns in cholangiocyte cells. The following novel conclusions have been made on the basis of numerical results:

1. The calcium concentration variation shows nonlinear behaviour mostly near the boundary the cell maintained at resting calcium concentration along space. Most of the parts of cells are dominated by the effect of source influx. This is necessary due to the requirement of a high concentration of calcium for initiation, sustenance, and termination of the activity of the cell. The nonlinear behaviour observed in the region near the resting condition of calcium at the boundary is due to the role of calcium-reducing mechanisms like buffering and various efflux like SERCA pump.
2. The combined effect of calcium-reducing mechanisms like buffering and efflux like SERCA pump play the role depending on the requirement of the cell which is visible from Figure 1 and 2. This role is limited to a small region in Figure 1 but this role is more and in the whole region of the cell in response to increasing in diffusion coefficient in Figure 2.
3. The buffers have a crucial role in reducing the calcium concentration in the cell when efflux like SERCA pump is fixed or constant or limited or absent.
4. The role of V_{serca} is crucial in reducing the calcium concentration in the cell when buffer quantity is fixed or constant or limited or absent.
5. The relation between calcium concentration and diffusion coefficient is inversely proportional that is the calcium concentration decreases with an increase in the diffusion coefficient.
6. The rise in calcium concentration is directly proportional to the rate of calcium release by storing the plasma membrane.

These novel insights obtained from the proposed model can be useful in understanding the mechanisms of the cells during health and disease. The present study was focused on calcium signaling in normal cholangiocyte cells. This model can be extended to the cells involving cholangiocyte disorders leading to various diseases like biliary cirrhosis etc. The present study provides the base for the development of models to evaluate abnormalities in mechanisms that can cause cholestatic disorders. The fractional processes of diffusion and Brownian motion can be incorporated in the future to develop a model of calcium distribution in cholangiocyte cells under various conditions. Various numerical and mathematical approaches like finite element method, cubic spline and iterated functional spaces can be explored in the future under various conditions. In the future, calcium signaling can be combined with other signaling systems to develop a systems biology model for cholangiocyte cells.

Declarations

Consent for publication

Not applicable.

Conflicts of interest

The authors declare that they have no conflict of interest.

Funding

Not applicable.

Author's contributions

N.: Conceptualization; V.M.: Conceptualization, Methodology, Writing - Original Draft, Graphics, Analysis, Investigation, Visualization, Software; N.A.: Review and editing of the manuscript. All authors discussed the results and contributed to the final manuscript.

Acknowledgements

Not applicable.

References

[1] Wake, K. Perisinusoidal stellate cells (fat-storing cells, interstitial cells, lipocytes), their related structure in and around the liver sinusoids, and vitamin A-storing cells in extrahepatic organs. *International review of cytology*, 66, 303-353, (1980). [CrossRef]

[2] Tabibian, J.H., Masyuk, A.I., Masyuk, T.V., O'Hara, S.P., & LaRusso, N.F. Physiology of cholangiocytes. *Comprehensive Physiology*, 3(1), (2013). [CrossRef]

[3] Wang, D.Q.H., Neuschwander-Tetri, B.A., & Portincasa, P. The Biliary System, Colloquium Series on Integrated Systems Physiology: From Molecule to Function. *Morgan & Claypool*, 109-145,(2012).

[4] Bouwens, L., De Bleser, P., Vanderkerken, K., Geerts, B., & Wisse, E. Liver cell heterogeneity: functions of non-parenchymal cells. *Enzyme*, 46, 155-168, (1992).

[5] Strazzabosco, M., & Fabris, L. Functional anatomy of normal bile ducts. *The Anatomical Record: Advances in Integrative Anatomy and Evolutionary Biology*, 291(6), 653-660, (2008). [CrossRef]

[6] Minagawa, N., Kruglov, E.A., Dranoff, J.A., Robert, M.E., Gores, G.J., & Nathanson, M.H. The anti-apoptotic protein Mcl-1 inhibits mitochondrial Ca^{2+} signals. *Journal of Biological Chemistry*, 280(39), 33637-33644, (2005). [CrossRef]

[7] Fiorotto, R., Spirlì, C., Fabris, L., Cadamuro, M., Okolicsanyi, L., & Strazzabosco, M. Ursodeoxycholic acid stimulates cholangiocyte fluid secretion in mice via CFTR-dependent ATP secretion. *Gastroenterology*, 133(5), 1603-1613, (2007). [CrossRef]

[8] Li, Q., Dutta, A., Kresge, C., Bugde, A., & Feranchak, A.P. Bile acids stimulate cholangiocyte fluid secretion by activation of transmembrane member 16A Cl^{-} channels. *Hepatology*, 68(1), 187-199, (2018). [CrossRef]

[9] Hirata, K., Dufour, J.F., Shibao, K., Knickelbein, R., O'Neill, A.F., Bode, H.P., ... & Nathanson, M.H. Regulation of Ca^{2+} signaling in rat bile duct epithelia by inositol 1, 4, 5-trisphosphate receptor isoforms. *Hepatology*, 36(2), 284-296, (2002). [CrossRef]

[10] Kotwani, M., & Adlakha, N. Modeling of endoplasmic reticulum and plasma membrane Ca^{2+} uptake and release fluxes with excess buffer approximation (EBA) in fibroblast cell. *International Journal of Computational Materials Science and Engineering*, 6(01), 1750004, (2017). [CrossRef]

[11] Panday, S., & Pardasani, K. R. Finite element model to study effect of advection diffusion and Na^{+}/Ca^{2+} exchanger on Ca^{2+} distribution in oocytes. *Journal of medical imaging and health informatics*, 3(3), 374-379, (2013). [CrossRef]

[12] Naik, P.A., & Pardasani, K.R. One dimensional finite element model to study calcium distri-

bution in oocytes in presence of VGCC, RyR and buffers. *Journal of Medical Imaging and Health Informatics*, 5(3), 471-476, (2015). [CrossRef]

[13] Naik, P.A., & Pardasani, K.R. Finite element model to study calcium distribution in oocytes involving voltage gated Ca^{2+} channel, ryanodine receptor and buffers. *Alexandria Journal of Medicine*, 52(1), 43-49, (2016). [CrossRef]

[14] Naik, P.A., & Pardasani, K.R. Three-dimensional finite element model to study effect of RyR calcium channel, ER leak and SERCA pump on calcium distribution in oocyte cell. *International Journal of Computational Methods*, 16(01), 1850091, (2019). [CrossRef]

[15] Jha, B.K., Adlakha, N., & Mehta, M.N. Finite element model to study calcium diffusion in astrocytes. *Int. J. of Pure and Appl. Math*, 78(7), 945-955, (2012).

[16] Jha, A., & Adlakha, N. Finite element model to study the effect of exogenous buffer on calcium dynamics in dendritic spines. *International Journal of Modeling, Simulation, and Scientific Computing*, 5(02), 1350027, (2014). [CrossRef]

[17] Jha, A., Adlakha, N., & Jha, B.K. Finite element model to study effect of Na^{+}-Ca^{2+} exchangers and source geometry on calcium dynamics in a neuron cell. *Journal of Mechanics in Medicine and Biology*, 16(02), 1650018, (2016). [CrossRef]

[18] Jha, A., & Adlakha, N. Two-dimensional finite element model to study unsteady state Ca^{2+} diffusion in neuron involving ER LEAK and SERCA. *International Journal of Biomathematics*, 8(01), 1550002, (2015). [CrossRef]

[19] Pathak, K.B., & Adlakha, N. Finite element model to study calcium signalling in cardiac myocytes involving pump, leak and excess buffer. *Journal of Medical Imaging and Health Informatics*, 5(4), 683-688, (2015). [CrossRef]

[20] Manhas, N., & Anbazhagan, N. A mathematical model of intricate calcium dynamics and modulation of calcium signalling by mitochondria in pancreatic acinar cells. *Chaos, Solitons & Fractals*, 145, 110741, (2021). [CrossRef]

[21] Manhas, N., & Pardasani, K.R. Mathematical model to study IP_3 dynamics dependent calcium oscillations in pancreatic acinar cells. *Journal of Medical Imaging and Health Informatics*, 4(6), 874-880, (2014). [CrossRef]

[22] Manhas, N., & Pardasani, K.R. Modelling mechanism of calcium oscillations in pancreatic acinar cells. *Journal of bioenergetics and biomembranes*, 46, 403-420, (2014). [CrossRef]

[23] Tewari, S.G., & Pardasani, K.R. Modeling effect of sodium pump on calcium oscillations in neuron cells. *Journal of Multiscale Modelling*, 4(03), 1250010, (2012). [CrossRef]

[24] Tewari, S., & Pardasani, K.R. Finite element model to study two dimensional unsteady state cytosolic calcium diffusion in presence of excess buffers. *IAENG International Journal of Applied Mathematics*, 40(3), 108-112, (2010).

[25] Jagtap, Y., & Adlakha, N. Numerical study of one-dimensional buffered advection–diffusion of calcium and IP_3 in a hepatocyte cell. *Network Modeling Analysis in Health Informatics and Bioinformatics*, 8(1), 25, (2019). [CrossRef]

[26] Jagtap, Y., & Adlakha, N. Finite volume simulation of two dimensional calcium dynamics in a hepatocyte cell involving buffers and fluxes. *Communications in Mathematical Biology and Neuroscience*, 2018, 15, (2018).

[27] Kumar, H., Naik, P.A., & Pardasani, K.R. Finite element model to study calcium distribution in T lymphocyte involving buffers and ryanodine receptors. *Proceedings of the National Academy of Sciences, India Section A: Physical Sciences*, 88, 585-590, (2018). [CrossRef]

[28] Kothiya, A., & Adlakha, N. Model of Calcium Dynamics Regulating IP_3 and ATP Production in a Fibroblast Cell. *Advances in Systems Science and Applications*, 22(3), 49-69, (2022).

[29] Kothiya, A.B., & Adlakha, N. Cellular nitric oxide synthesis is affected by disorders in the interdependent Ca^{2+} and IP_3 dynamics during cystic fibrosis disease. *Journal of Biological Physics*, 1-26, (2023). [CrossRef]

[30] Bhardwaj, H., & Adlakha, N. Radial Basis Function Based Differential Quadrature Approach to Study Reaction Diffusion of Ca^{2+} in T Lymphocyte. *International Journal of Computational Methods*, (2022). [CrossRef]

[31] Minagawa, N., Nagata, J., Shibao, K., Masyuk, A.I., Gomes, D.A., Rodrigues, M.A., ... & Nathanson, M.H. Cyclic AMP regulates bicarbonate secretion in cholangiocytes through release of ATP into bile. *Gastroenterology*, 133(5), 1592-1602, (2007). [CrossRef]

[32] Nathanson, M.H., Burgstahler, A.D., Mennone, A.L.B.E.R.T., & Boyer, J.L. Characterization of cytosolic Ca^{2+} signaling in rat bile duct epithelia. *American Journal of Physiology-Gastrointestinal and Liver Physiology*, 271(1), G86-G96, (1996). [CrossRef]

[33] Woo, K., Dutta, A.K., Patel, V., Kresge, C., & Feranchak, A.P. Fluid flow induces mechanosensitive ATP release, calcium signalling and Cl^- transport in biliary epithelial cells through a PKCγ-dependent pathway. *The Journal of physiology*, 586(11), 2779-2798, (2008). [CrossRef]

[34] Weerachayaphorn, J., Amaya, M.J., Spirli, C., Chansela, P., Mitchell-Richards, K.A., Ananthanarayanan, M., & Nathanson, M.H. Nuclear factor, erythroid 2-like 2 regulates expression of type 3 inositol 1, 4, 5-trisphosphate receptor and calcium signaling in cholangiocytes. *Gastroenterology*, 149(1), 211-222, (2015). [CrossRef]

[35] Ueasilamongkol, P., Khamphaya, T., Guerra, M. T., Rodrigues, M.A., Gomes, D.A., Kong, Y., ... & Weerachayaphorn, J. Type 3 inositol 1, 4, 5-trisphosphate receptor is increased and enhances malignant properties in cholangiocarcinoma. *Hepatology*, 71(2), 583-599, (2020). [CrossRef]

[36] Shibao, K., Hirata, K., Robert, M.E., & Nathanson, M.H. Loss of inositol 1, 4, 5-trisphosphate receptors from bile duct epithelia is a common event in cholestasis. *Gastroenterology*, 125(4), 1175-1187, (2003). [CrossRef]

[37] Rodrigues, M.A., Gomes, D.A., & Nathanson, M.H. Calcium signaling in cholangiocytes: methods, mechanisms, and effects. *International Journal of Molecular Sciences*, 19(12), 3913, (2018). [CrossRef]

[38] Masyuk, A.I., Masyuk, T.V., Splinter, P.L., Huang, B.Q., Stroope, A.J., & LaRusso, N.F. Cholangiocyte cilia detect changes in luminal fluid flow and transmit them into intracellular Ca^{2+} and cAMP signaling. *Gastroenterology*, 131(3), 911-920, (2006). [CrossRef]

[39] Marzioni, M., Alpini, G., Saccomanno, S., Candelaresi, C., Venter, J., Rychlicki, C., ... & Benedetti, A. Glucagon-like peptide-1 and its receptor agonist exendin-4 modulate cholangiocyte adaptive response to cholestasis. *Gastroenterology*, 133(1), 244-255, (2007). [CrossRef]

[40] Martin, J., & Dufour, J.F. Cholestasis shuts down calcium signaling in cholangiocytes. *Hepatology*, 39(1), 248-249, (2004). [CrossRef]

[41] Maroni, L., Haibo, B., Ray, D., Zhou, T., Wan, Y., Meng, F., ... & Alpini, G. Functional and structural features of cholangiocytes in health and disease. *Cellular and molecular gastroenterology and hepatology*, 1(4), 368-380, (2015). [CrossRef]

[42] Lazaridis, K.N., Strazzabosco, M., & LaRusso, N.F. The cholangiopathies: disorders of biliary epithelia. *Gastroenterology*, 127(5), 1565-1577, (2004). [CrossRef]

[43] Jung, J., & Lee, M.G. Role of calcium signaling in epithelial bicarbonate secretion. *Cell Calcium*,

55(6), 376-384, (2014). [CrossRef]

[44] Guerra, M.T., & Nathanson, M.H. Calcium signaling and secretion in cholangiocytes. Pancreatology, 15(4), S44-S48, (2015). [CrossRef]

[45] Amaya, M.J., & Nathanson, M.H. Calcium signaling and the secretory activity of bile duct epithelia. *Cell Calcium*, 55(6), 317-324, (2014). [CrossRef]

[46] Shin, D.H., Kim, M., Kim, Y., Jun, I., Jung, J., Nam, J.H., ... & Lee, M.G. Bicarbonate permeation through anion channels: its role in health and disease. *Pflügers Archiv-European Journal of Physiology*, 472, 1003-1018, (2020). [CrossRef]

[47] Alpini, G., Glaser, S.S., Rodgers, R., Phinizy, J.L., Robertson, W.E., Lasater, J., ... & LeSage, G.D. Functional expression of the apical Na+-dependent bile acid transporter in large but not small rat cholangiocytes. *Gastroenterology*, 113(5), 1734-1740, (1997). [CrossRef]

[48] Lopez-Caamal, F., Oyarzún, D.A., Middleton, R. H., & García, M.R. Spatial Quantification of Cytosolic Ca^{2+} Accumulation in Non excitable Cells: An Analytical Study. *IEEE/ACM Transactions on Computational Biology and Bioinformatics*, 11(3), 592-603, (2014). [CrossRef]

[49] Pawar, A., & Pardasani, K.R. Effect of disturbances in neuronal calcium and IP_3 dynamics on β-amyloid production and degradation. *Cognitive Neurodynamics*, 1-18, (2022). [CrossRef]

[50] Pawar, A., & Pardasani, K.R. Simulation of disturbances in interdependent calcium and β-amyloid dynamics in the nerve cell. *The European Physical Journal Plus*, 137(8), 1-23, (2022). [CrossRef]

[51] Pawar, A., & Pardasani, K.R. Study of disorders in regulatory spatiotemporal neurodynamics of calcium and nitric oxide. *Cognitive Neurodynamics*, 1-22, (2022). [CrossRef]

[52] Pawar, A., & Pardasani, K.R. Computational model of calcium dynamics-dependent dopamine regulation and dysregulation in a dopaminergic neuron cell. *The European Physical Journal Plus*, 138(1), 30, (2023). [CrossRef]

[53] Pawar, A., & Raj Pardasani, K. Effects of disorders in interdependent calcium and IP_3 dynamics on nitric oxide production in a neuron cell. *The European Physical Journal Plus*, 137(5), 1-19, (2022). [CrossRef]

[54] Pankratova, E.V., Sinitsina, M.S., Gordleeva, S., & Kazantsev, V.B. Bistability and Chaos Emergence in Spontaneous Dynamics of Astrocytic Calcium Concentration. *Mathematics*, 10(8), 1337, (2022). [CrossRef]

[55] Joshi, H., & Jha, B.K. 2D dynamic analysis of the disturbances in the calcium neuronal model and its implications in neurodegenerative disease. *Cognitive Neurodynamics*, 1-12, (2022). [CrossRef]

[56] Joshi, H., & Jha, B.K. 2D memory-based mathematical analysis for the combined impact of calcium influx and efflux on nerve cells. *Computers & Mathematics with Applications*, 134, 33-44, (2023). [CrossRef]

[57] Tarifa, C., Vallmitjana, A., Jiménez-Sábado, V., Marchena, M., Llach, A., Herraiz-Martínez, A., ... & Hove-Madsen, L. *Spatial distribution of calcium sparks determines their ability to induce afterdepolarizations in human atrial myocytes. Basic to Translational Science*, 8(1), 1-15, (2023). [CrossRef]

[58] Chang, Y., Funk, M., Roy, S., Stephenson, E., Choi, S., Kojouharov, H. V., ... & Pan, Z. Developing a mathematical model of intracellular calcium dynamics for evaluating combined anticancer effects of afatinib and RP4010 in esophageal cancer. International Journal of Molecular Sciences, 23(3), 1763, (2022). [CrossRef]

[59] Joshi, H., & Jha, B.K. Chaos of calcium diffusion in Parkinson's infectious disease model and treatment mechanism via Hilfer fractional derivative. *Mathematical Modelling and Numerical Simulation with Applications*, 1(2), 84-94, (2021). [CrossRef]

[60] Naik, P.A. Modeling the mechanics of calcium regulation in T lymphocyte: a finite element method approach. *International Journal of Biomathematics*, 13(05), 2050038, (2020). [CrossRef]

[61] Naik, P.A., Eskandari, Z., & Shahraki, H.E. Flip and generalized flip bifurcations of a two-dimensional discrete-time chemical model. *Mathematical Modelling and Numerical Simulation with Applications*, 1(2), 95-101, (2021). [CrossRef]

[62] Naik, P.A., & Pardasani, K.R. Two dimensional finite element model to study calcium distribution in oocytes. *Journal of Multiscale Modelling*, 6(01), 1450002, (2015). [CrossRef]

[63] Jha, B.K., & Joshi, H. A Fractional Mathematical Model to Study the Effect of Buffer and Endoplasmic Reticulum on Cytosolic Calcium Concentration in Nerve Cells. *In Fractional Calculus in Medical and Health Science* (pp. 211-227), CRC Press, (2020). [CrossRef]

Mathematical Modelling and Numerical Simulation with Applications (MMNSA)
(https://dergipark.org.tr/en/pub/mmnsa)

How to cite this article: Nakul, N., Mishra, V. & Adlakha, N. (2023). Finite volume simulation of calcium distribution in a cholangiocyte cell. *Mathematical Modelling and Numerical Simulation with Applications*, 3(1), 17-32. https://doi.org/10.53391/mmnsa.1273945

Mathematical Modelling and Numerical Simulation with Applications, 2023, 3(1), 33–57

https://dergipark.org.tr/en/pub/mmnsa
ISSN Online: 2791-8564 / Open Access
https://doi.org/10.53391/mmnsa.1273982

RESEARCH PAPER

Malaria and cholera co–dynamic model analysis furnished with fractional-order differential equations

Livinus L. Iwa [1,‡,*], **Ugochukwu K. Nwajeri** [1,‡], **Anne O. Atede** [1,‡], **Augustine B. Panle** [1,‡] **and Kenneth U. Egeonu** [1,‡]

[1]Department of Mathematics, Federal University of Technology, Owerri, Nigeria

*Corresponding Author
‡iwa.livinus@gmail.com (Livinus L. Iwa); ugochukwu.nwajeri@futo.edu.ng (Ugochukwu K. Nwajeri); anoja4god@gmail.com (Anne O. Atede); panle.augustine@futo.edu.ng (Augustine B. Panle); kennethegeonu91@gmail.com (Kenneth U. Egeonu)

Abstract

This paper presents malaria and cholera co–dynamics under Caputo–Fabrizio derivative of order $\alpha \in (0,1)$ varied with some notable parameters in the fractional system. The fractional order system comprises ten compartments divided into human and vector classes. The human population is exposed to obnoxious diseases such as malaria and cholera which can lead to an untimely death if proper care is not taken. As a result, we present the qualitative analysis of the fractional order system where the existence and uniqueness of the solution using the well-known Banach and Schauder fixed point theorems. The numerical solution of the system is achieved through the famous iterative Atangana–Baleanu fractional order Adams–Bashforth scheme. The numerical algorithm obtained from the scheme is used for graphic simulation for different fractional orders $\alpha \in (0,1)$. The figures produced using various fractional orders show total convergence and stability as time increases. It is also evident that stability and convergence are achieved as the fractional orders tend to 1. The actual behavior of the fractional co–dynamical system of the diseases is established also in the numerical simulation.

Keywords: Malaria disease; cholera disease; fractional derivative; stability; co-infection

AMS 2020 Classification: 34C60; 92C42; 92D30; 92D25

1 Introduction

The disease malaria caused by harmful parasites and transmitted from infected female **anopheles** mosquitoes to humans through contagious bites is a serious life-threatening disease and one of the most common deadly diseases in the world. This disease has caused millions of life all over the world, especially in tropical and sub-Saharan Africa [1], where the parasites can survive freely in the host. The world malaria report of 2021, shows that in the year 2020, an estimated 627,000

➤ **Received:** 30.01.2023 ➤ **Revised:** 20.03.2023 ➤ **Accepted:** 24.03.2023 ➤ **Published:** 31.03.2023

deaths occurred out of estimated 241 million cases of malaria reported worldwide. Among these number of reported cases of malaria, there were 95 percent recorded cases in Africa with 94 percent deaths which include 80 percent of children under the age of five [2]. Most of the deaths recorded occurred during a latent period of 10–15 days with symptoms of severe fever, headaches, and loss of appetite for food or drinks. Suspected cases of malaria symptoms are confirmed through parasite–based diagnosis testing. The WHO recommends the use of insecticide-treated nets (ITNs), indoor residual spraying (IRS) and draining of stagnant waters to prevent transmission of malaria. On the other hand, the disease cholera is an acute diarrhoeal infection caused by ingestion of food and water contaminated with the bacterium Vibrio cholera [3, 4]. An estimated 1.3 to 4 million cases of cholera are reported globally each year and 21,000 to 143,000 deaths are recorded annually to cholera. Inadequate access to clean water and properly sanitized water are normally linked to the transmission of cholera.

The number of reported cases of cholera has continued to grow in recent years. In 2020, 323,369 cases were recorded with 857 deaths from 24 countries amidst limitations in surveillance systems and the fear of trade and tourism. The co-infection of these diseases is prevalent in the sense that the parasite which transmits these diseases are associated with contaminated water and the environment. It is widely known that mosquitoes are the real agents of malaria which breed from stagnant and contaminated water. In another hand, the contaminated water where these mosquitoes breed is the main source of cholera transmission. Both these diseases are treatable through clinical means but can be harmful to vital organs if proper care and diagnosis are found wanting.

Mathematical models have been used extensively over the years as relevant tools in understanding the dynamics of disease transmission and policy-making with regard control mechanism of diseases. For instance, Ross [5] first formulated the malaria transmission models. In his paper, he focused on malaria prevention and showed that the mosquito population should decrease to a certain threshold for malaria to be eradicated. Okosun et al. [6] formulated a mathematical model for malaria–cholera co-infection for the purpose of investigating the synergy between malaria and cholera in the face of treatment. Other important contribution includes Egeonu et al. [7] who proposed a co-infection model for two–strains of malaria and cholera with optimal control. Mandal et al. [8] proposed a hierarchical structure of a range of deterministic models of different levels of complexity and the evolution of modelling strategies to describe malaria incidence by including the critical features of host–vector–parasite interactions.

Oke et al. [9] proposed a mathematical model of malaria disease with a control strategy where prevention through bed nets, treatment, and insecticide were considered. In their paper, it was demonstrated that the use of treatments and treated bed nets should be taken into account when scarce resources arise while combining the two gives maximum results to malaria control. Osman and Adu [10] analyzed two sections in their mathematical model; the SEIR and the SEIR-SEI models. They showed that malaria may be controlled through the use of active malaria drugs, insecticides, and mosquito-treated nets. Tilahun et al. [11] proposed a stochastic and deterministic mathematical model of cholera disease dynamics with direct transmission. Hintsa and Kahsay [12] proposed the analysis of cholera epidemic control using mathematical models. In their findings, they showed that the introduction of preventive measures for contracting the disease reduces the basic reproduction number to below one as against the opposite where the reproduction number is greater than one. This suggests that cholera disease can be controlled and eliminated from the community if susceptible and recovered individuals comply with the preventive measures. However, a few studies have been carried out on the formulation and application of fractional order differential equations of malaria models. To the best of our knowledge, no work has been carried out on the analysis of co–dynamic model of malaria and cholera via Caputo–Fabrizio

fractional order differential equation. Only recently, the authors in [13] used Caputo–Fabrizio fractional order derivative to model HPV and Syphilis diseases. Omame et al. [14] proposed a fractional order model for dual variants of COVID-19 and HIV co-infection via another derivative that has a non–singular kernel, Atangana–Baleanu fractional order derivative. Nwajeri et al. [15] proposed the analysis of HPV and CT co-infection model using a fractional order derivative. Fractional order derivatives have made a tremendous contribution to the field of epidemiological modelling and have huge developments [16–25]. It is evident nowadays that fractional differential equations are efficient tools and very useful and effective in numerous fields of science and engineering such as biology, finance, rheology, electro–chemistry, chemical physics, etc. These wonderful applications of fractional differential equations to physical problems are due to their natural relation to the system with memory which is a common feature of many phenomena [26–31].

The aim of this work is to analyze vividly the co–dynamism of malaria and cholera via fractional order derivative. In particular, we formulate a fractional order model of ten compartments which depicts the two diseases' interaction within a population. The model is based on the paper of Omame et al. [32] where Atangana–Baleanu fractional order derivative to model the impact of SARS-CoV-2 infection on the dynamics of dengue and HIV. Moreover, we describe and analyze the results using Caputo–Fabrizio fractional derivative and Caputo fractional derivative.

The rest of the paper is arranged as follows; the fractional order model is formulated in Section 2 via Caputo–Fabrizio fractional derivative. In Section 3, we present in nutshell, some definitions of fractional order differential equations. Qualitative analysis of the fractional system takes the centre stage in Section 4 where the positive invariant region of the system, and basic reproduction number are presented. We also present the existence and uniqueness of the solution using the fixed point theorem. In Section 5, we developed the numerical solution of the fractional system with the aid of the Atangana-Baleanu technique. In Section 6, graphical figures and their biological discussions and results were presented after rigorous MATLAB simulations. Finally, we draw the necessary conclusion of our manuscript in Section 7.

2 Model formulation

The model consists of different compartments of human and vector populations. The human population is divided into the following compartments: susceptible humans $\mathcal{S}_{HB}$, infected individuals with malaria $\mathcal{I}_{MAL}$, recovered individuals from malaria disease $\mathcal{R}_{MAL}$, individuals infected with cholera $\mathcal{I}_{CHO}$, recovered individuals from cholera disease $\mathcal{R}_{CHO}$, individuals co-infected with malaria and cholera $\mathcal{I}_{MAC}$ and recovered individuals from malaria and cholera $\mathcal{R}_{MAC}$. On another note, we have bacterial population denoted by $\mathcal{B}_{CHO}$ and the vector population which is divided into two compartments, namely, the susceptible vectors $\mathcal{S}_{VEC}(t)$ and infected vectors $\mathcal{I}_{VEC}(t)$. The total population of humans and vectors at the time t are given by $\mathcal{N}_{HB}(t) = \mathcal{S}_{HB}(t) + \mathcal{I}_{MAL}(t) + \mathcal{R}_{MAL}(t) + \mathcal{I}_{CHO}(t) + \mathcal{R}_{CHO}(t) + \mathcal{I}_{MAC}(t) + \mathcal{R}_{MAC}(t)$ and $\mathcal{N}_{VEC}(t) = \mathcal{S}_{VEC}(t) + \mathcal{I}_{VEC}(t)$, respectively. The parameter β_{MAL} denotes the probability of humans infected with malaria while μ_{HB} denotes the natural mortality rate from the human population. The quantity $\frac{\beta_{MAL} b \mathcal{I}_{VEC}}{N_{HB}}$ represents the rate $\mathcal{S}_{HB}$ are exposed to the infected vectors and moved to $\mathcal{I}_{MAL}$ and and $\mathcal{I}_{MAC}$ compartments while the quantity $\frac{\mathcal{B}_{CHO} q_{CHO}}{\kappa + \mathcal{B}_{CHO}} \mathcal{S}_{HB}$ denotes the rate $\mathcal{S}_{HB}$ contracts cholera through bacteria and moved to $\mathcal{I}_{CHO}$ and $\mathcal{I}_{MAC}$ classes. The remaining parameters are properly defined in Table 1.

Table 1. Description of parameters in model (1)

Parameter	Description	Value	References
Λ_{HB}	Recruitment rate of humans	$100day^{-1}$	[33]
β_{MAL}	Human probability of infection with malaria	0.181 (dimensionless)	[34]
q_{CHO}	Bacterial contact rate for human	$0.05day^{-1}$	[6]
β_{CHO}	Human probability of infection with cholera	0.005	Assumed
μ_{HB}	Natural death rate for humans	$\frac{1}{(70\times360)}day^{-1}$	[7]
r	Per capita bacteria reproduction rate	0.5	Assumed
b	Average vectors bitting rate	$0.5day^{-1}$	[35]
ω_{MAL}	Waning rate of malaria	$\frac{1}{(60\times360)}day^{-1}$	[33]
ω_{CHO}	Waning rate of cholera	$0.001day^{-1}$	[34]
ω_{mc}	Malaria-Cholera co-infection waning rate	$0.001-0.02day^{-1}$	[6]
δ_{MAL}	Malaria induced death rate	$0.05-0.1day^{-1}$	[6, 36]
γ_{MAL}	Recovery rate from malaria	0.25	[37]
δ_{CHO}	cholera induced death rate	$0.0002day^{-1}$	Assumed
γ_{CHO}	Recovery rate from cholera	$0.07day^{-1}$	[34]
β_{VEC}	Vector probability of infection with malaria	0.181 (dimensionless)	[34]
δ_{MAC}	Death caused by malaria-cholera co-infection	$0.05day^{-1}$	Assumed
γ_{MAC}	Recovery rate for malaria and cholera	$0.4day^{-1}$	Assumed
ξ_{MP1}, ξ_{MP2}	Modification parameters	0.6 (dimensionless)	Assumed
μ_{DBR}	Natural death rate for bacterial	0.123	[38]
μ_{VEC}	Natural death rate for vectors	$\frac{1}{15}, 0.143day^{-1}$	[33]
Λ_{VEC}	Recruitment rate for vectors	$1000day^{-1}$	[33]

Motivated by the numerous advantages of fractional order operators as already stated, we hereby state the fractional order co–dynamic model under the Caputo–Fabrizio derivative as

$$
\begin{aligned}
{}^{CF}\mathcal{D}_t^{\alpha}\mathcal{S}_{HB}(t) &= \Lambda_{HB} - \frac{\beta_{MAL} b \mathcal{I}_{VEC}}{N_{HB}}\mathcal{S}_{HB} - \frac{\mathcal{B}_{CHO} q_{CHO}}{\kappa + \mathcal{B}_{CHO}}\mathcal{S}_{HB} - \mu_{HB}\mathcal{S}_{HB} + \omega_{MAL}\mathcal{R}_{MAL} \\
&\quad + \omega_{CHO}\mathcal{R}_{CHO} + \omega_{mc}\mathcal{R}_{MAC}, \\
{}^{CF}\mathcal{D}_t^{\alpha}\mathcal{I}_{MAL}(t) &= \beta_{MAL} b \frac{\mathcal{I}_{VEC}}{\mathcal{N}_{HB}}(\mathcal{S}_{HB} + \mathcal{R}_{CHO}) + \frac{\mathcal{B}_{CHO} q_{CHO}}{\kappa + \mathcal{B}_{CHO}}\mathcal{I}_{MAL} - (\mu_{HB} + \delta_{MAL} + \gamma_{MAL})\mathcal{I}_{MAL}, \\
{}^{CF}\mathcal{D}_t^{\alpha}\mathcal{R}_{MAL}(t) &= \gamma_{MAL}\mathcal{I}_{MAL} - (\mu_{MAL} + \omega_{MAL})\mathcal{R}_{MAL} - \frac{\mathcal{B}_{CHO} q_{CHO}}{\kappa + \mathcal{B}_{CHO}}\mathcal{R}_{MAL}, \\
{}^{CF}\mathcal{D}_t^{\alpha}\mathcal{I}_{CHO}(t) &= \frac{\beta_{CHO} q_{CHO}}{\kappa + \mathcal{B}_{CHO}}(\mathcal{S}_{HB} + \mathcal{R}_{MAL}) - (\delta_{CHO} + \mu_{HB} + \gamma_{CHO})\mathcal{I}_{CHO} - \frac{\beta_{VEC} b \mathcal{I}_{VEC}}{\mathcal{N}_{HB}}\mathcal{I}_{CHO}, \\
{}^{CF}\mathcal{D}_t^{\alpha}\mathcal{R}_{CHO}(t) &= \gamma_{CHO}\mathcal{I}_{CHO} - (\mu_{HB} + \omega_{CHO})\mathcal{R}_{CHO} - \frac{\beta_{MAL} b \mathcal{I}_{VEC}}{\mathcal{N}_{HB}}\mathcal{R}_{CHO}, \\
{}^{CF}\mathcal{D}_t^{\alpha}\mathcal{I}_{MAC}(t) &= \frac{\mathcal{B}_{CHO} q_{CHO}}{\kappa + \mathcal{B}_{CHO}}\mathcal{I}_{MAL} + \frac{\beta_{MAL} b \mathcal{I}_{VEC}}{\mathcal{N}_{HB}}\mathcal{I}_{CHO} - (\mu_{HB} + \delta_{MAC} + \gamma_{MAC})\mathcal{I}_{MAC}, \\
{}^{CF}\mathcal{D}_t^{\alpha}\mathcal{R}_{MAC}(t) &= \gamma_{MAC}\mathcal{I}_{CHO} - (\mu_{HB} + \omega_{mc})\mathcal{R}_{MAC}, \\
{}^{CF}\mathcal{D}_t^{\alpha}\mathcal{B}_{CHO}(t) &= r\mathcal{B}_{CHO}\left(1 - \frac{\mathcal{B}_{CHO}}{\kappa}\right) + \xi_{MP1}\mathcal{I}_{CHO} + \xi_{MP2}\mathcal{I}_{MAC} - \mu_{DBR}\mathcal{B}_{CHO}, \\
{}^{CF}\mathcal{D}_t^{\alpha}\mathcal{S}_{VEC}(t) &= \Lambda_{VEC} - \frac{\beta_{VEC} b (\mathcal{I}_{MAL} + \mathcal{I}_{MAC})}{\mathcal{N}_{HB}}\mathcal{S}_{VEC} - \mu_{VEC}\mathcal{S}_{VEC}, \\
{}^{CF}\mathcal{D}_t^{\alpha}\mathcal{I}_{VEC}(t) &= \frac{\beta_{VEC} b (\mathcal{I}_{MAL} + \mathcal{I}_{MAC})}{\mathcal{N}_{HB}}\mathcal{S}_{VEC} - \mu_{VEC}\mathcal{I}_{VEC},
\end{aligned}
\tag{1}
$$

which corresponds to the following initial conditions

$$\begin{cases} \mathcal{S}_{HB}(0) = \mathcal{S}_{HB(0)} \geq 0, \quad \mathcal{I}_{MAL}(0) = \mathcal{I}_{MAL(0)} \geq 0, \quad \mathcal{R}_{MAL}(0) = \mathcal{R}_{MAL(0)} \geq 0, \\ \mathcal{I}_{CHO}(0) = \mathcal{I}_{CHO(0)} \geq 0, \quad \mathcal{R}_{CHO}(0) = \mathcal{R}_{CHO(0)} \geq 0, \quad \mathcal{I}_{MAC}(0) = \mathcal{I}_{MAC(0)} \geq 0, \\ \mathcal{R}_{MAC}(0) = \mathcal{R}_{MAC(0)} \geq 0, \quad \mathcal{B}_{CHO}(0) = \mathcal{B}_{CHO(0)} \geq 0, \quad \mathcal{S}_{VEC}(0) = \mathcal{S}_{VEC(0)} \geq 0, \\ \mathcal{I}_{VEC}(0) = \mathcal{I}_{VEC(0)} \geq 0. \end{cases} \tag{2}$$

3 Preliminaries

This section presents several important properties and definitions of Caputo-Fabrizio derivative in the Caputo sense which will aid the analysis of the manuscript.

Definition 1 ([39]) *The Caputo–Fabrizio fractional derivative of order α for the function $\mathcal{K} \in H^1([0,b],\mathbb{R}^+)$ where $b > 0$ is given by*

$$^{CF}\mathcal{D}_t^{\alpha}\mathcal{K}(t) = \frac{(2-\alpha)\mathcal{U}(\alpha)}{2(1-\alpha)}\int_0^t \exp\left(\frac{-\alpha(t-\xi)}{1-\alpha}\right)\mathcal{K}'(\zeta)d\zeta, \qquad 0 < \alpha \leq 1, \qquad t \geq 0. \tag{3}$$

Definition 2 ([40]) *The Caputo–Fabrizio fractional integral order α for the function $\mathcal{K} \in H^1([0,b],\mathbb{R}^+)$ where $b > 0$ is given by*

$$^{CF}I_t^{\alpha}\mathcal{K}(t) = \frac{2(1-\alpha)}{(2-\alpha)\mathcal{U}(\alpha)}\mathcal{K}(t) + \frac{2\alpha}{(2-\alpha)\mathcal{U}(\alpha)}\int_0^t \mathcal{K}(\zeta)d\zeta, \qquad 0 < \alpha \leq 1, \qquad t \geq 0. \tag{4}$$

Definition 3 ([22]) *The Atangana–Baleanu fractional derivative in the Caputo sense of order α for the function $\mathcal{K} \in H^1([0,b],\mathbb{R}^+)$, where $b > 0$, is given by*

$$^{ABC}\mathcal{D}_t^{\alpha}\mathcal{K}(t) = \frac{\mathcal{U}(\alpha)}{(1-\alpha)}\int_0^t \mathcal{E}_{\alpha}\left(\frac{-\alpha(t-\zeta)}{1-\alpha}\right)\mathcal{K}'(\zeta)d\zeta, \qquad 0 < \alpha \leq 1, \qquad t \geq 0.$$

Definition 4 ([39]) *The Atangana–Baleanu fractional integral of order α for the function $\mathcal{K} \in H^1([0,b],\mathbb{R}^+)$, where $b > 0$, is given by*

$$^{AB}I_t^{\alpha}\mathcal{K}(t) = \frac{(1-\alpha)}{\mathcal{U}(\alpha)}\mathcal{K}(t) + \frac{\alpha}{\mathcal{U}(\alpha)\Gamma(\alpha)}\int_0^t (t-\zeta)^{\alpha-1}\mathcal{K}(\zeta)d\zeta, \qquad 0 < \alpha \leq 1, \qquad t \geq 0, \tag{5}$$

where $\mathcal{U}(\alpha)$ denotes the normalization function and

$$\mathcal{E}_{\alpha}(d) = \sum_{k=0}^{\infty}\frac{d^k}{\Gamma(\alpha k+1)}, \quad \Re(\alpha) > 0.$$

Lemma 1 ([39]) *The solution for the following problem with $\alpha \in (0,1]$ is given as:*

$$\begin{aligned} ^{CF}\mathcal{D}_t^{\alpha}\mathcal{W}(t) &= \mathcal{V}(t), \\ \mathcal{W}(0) &= \mathcal{W}_0, \end{aligned} \tag{6}$$

that is assumed to be equivalent to the following fractional Volterra integral equation

$$\mathcal{W}(t) = \mathcal{W}_0 + \frac{2(1-\alpha)}{(2-\alpha)\mathcal{U}(\alpha)}\left(\mathcal{V}(t)-\mathcal{V}(0)\right) + \frac{2\alpha}{(2-\alpha)\mathcal{U}(\alpha)}\int_0^t \mathcal{W}(\zeta)d\zeta, \qquad t \geq 0. \tag{7}$$

Lemma 2 ([40]) *The Laplace transform of Caputo-Fabrizio fractional derivative in the Caputo sense of order $\alpha \in (0,1]$ for the function $\mathcal{K}(t)$ is given by*

$$\mathcal{L}\{D_t^\alpha \mathcal{K}(t), s\} = \frac{(2-\alpha)\mathcal{U}(\alpha)}{2}\frac{s\mathcal{L}\{\mathcal{K}(t)\}-\mathcal{K}(0)}{s+\alpha(1-s)}, \qquad s \geq 0.$$

4 Qualitative analysis of the constructed model

In this section, we present carefully the analysis of the fractional order co–dynamic model of malaria and cholera (1) where the positivity of the solution, basic reproduction number via next-generation matrix method, existence and uniqueness of the solution are presented.

Positivity

Lemma 3 *The region $\mathcal{D} = \mathcal{D}_h \cup \mathcal{D}_b \cup \mathcal{D}_v \subset \mathcal{R}_+^7 \times \mathcal{R}_+ \times \mathcal{R}_+^2$ is non-negatively invariant for the model (1) with initial conditions in $\mathcal{R}_+^{10}$, where*

$$\begin{aligned}\mathcal{D}_h = \Big\{ &(\mathcal{S}_{HB}, \mathcal{I}_{MAL}, \mathcal{R}_{MAL}, \mathcal{I}_{CHO}, \mathcal{R}_{CHO}, \mathcal{I}_{MAC}, \mathcal{R}_{MAC}) : \mathcal{S}_{HB} + \mathcal{I}_{MAL} \\ &+\mathcal{R}_{MAL} + \mathcal{I}_{CHO} + \mathcal{R}_{CHO} + \mathcal{I}_{MAC} + \mathcal{R}_{MAC} < \frac{\Lambda_{HB}}{\mu_{HB}}\Big\},\end{aligned}$$

$$\mathcal{D}_b = \left\{\mathcal{B}_{CHO} : \mathcal{B}_{CHO} \leq \frac{(\rho_1+\rho_2)\,\Lambda_{HB}}{\mu_{HB}\mu_{DBR}}\right\},$$

$$\mathcal{D}_v = \left\{(\mathcal{S}_{VEC}, \mathcal{I}_{VEC}) : \mathcal{S}_{VEC} + \mathcal{I}_{VEC} \leq \frac{\Lambda_{VEC}}{\mu_{VEC}}\right\}.$$

Proof Adding all the equations corresponding to the human components of the system (1) gives

$${}^{\mathcal{CF}}\mathcal{D}_t^\alpha \mathcal{N}_{HB}(t) = \Lambda_{HB} - \mu_{HB}\mathcal{N}_{HB}(t) - \left[\delta_{MAL}\mathcal{I}_{MAL} + \delta_{CHO}\mathcal{I}_{CHO} + \delta_{MAC}\mathcal{I}_{MAC}\right], \tag{8}$$

so that from (8), we have

$${}^{\mathcal{CF}}\mathcal{D}_t^\alpha \mathcal{N}_{HB}(t) \leq \Lambda_{HB} - \mu_{HB}\mathcal{N}_{HB}(t).$$

Applying the Laplace transform of the Caputo-Fabrizio derivative on the above inequality, and

simplifying, we obtain

$$\begin{aligned}\mathcal{N}_{HB}(t) \leq & \frac{\Lambda_{HB}}{\mu_{HB}} - \frac{\Lambda_{HB}(2\alpha-\varrho_1)}{[1+\mu_{HB}(1-\alpha)]\varrho_1}e^{-\varrho_1 t} - \frac{\mathcal{N}_{HB}(0)}{(1-\alpha)[1+\mu_{HB}(1-\alpha)](\varrho_1-\varrho_2)}e^{-\varrho_1 t} \\ & + \frac{\mathcal{N}_{HB}(0)}{(1-\alpha)[1+\mu_{HB}(1-\alpha)](\varrho_1-\varrho_2)}e^{-\varrho_2 t},\end{aligned}$$

where $\varrho_1 = \frac{\mu_{HB}\alpha}{1+\mu_{HB}(1-\alpha)}$, $\varrho_2 = \frac{\alpha}{(1-\alpha)}$. Thus, the total population of humans, $\mathcal{N}_{HB}(t) \leq \frac{\Lambda_{HB}}{\mu_{HB}}$ as $t \to \infty$. Similarly, the total population of vectors $\mathcal{N}_{VEC}(t) \leq \frac{\Lambda_{VEC}}{\mu_{VEC}}$ and total bacteria population $\mathcal{B}_{CHO}(t) \leq \frac{K(r-\mu_{DBR})}{\mu_{DBR}}$. This shows that malaria and cholera fractional order model (1) is bounded and has a solution in $\mathcal{D}_h$, $\mathcal{D}_b$ and $\mathcal{D}_v$, respectively. Hence, for fractional malaria and cholera co–dynamic model, $\mathcal{D}_h$, $\mathcal{D}_b$ and $\mathcal{D}_v$ are positively invariant regions and thus the proof. ■

Basic reproduction number

The disease-free equilibrium (DFE) of the fractional order malaria and cholera co–dynamic model (1) achieved by setting the right-hand side of the equations of the model to zero is given by

$$\begin{aligned}\mathcal{T}_0 &= (\mathcal{S}^*_{HB}, \mathcal{I}^*_{MAL}, \mathcal{R}^*_{MAL}, \mathcal{I}^*_{CHO}, \mathcal{R}^*_{CHO}, \mathcal{I}^*_{MAC}, \mathcal{R}^*_{MAC}, \mathcal{B}^*_{CHO}, \mathcal{S}^*_{VEC}, \mathcal{I}^*_{VEC}) \\ &= \left(\frac{\Lambda_{HB}}{\mu_{HB}}, 0, 0, 0, 0, 0, 0, 0, \frac{\Lambda_{VEC}}{\mu_{VEC}}, 0\right).\end{aligned} \tag{9}$$

Using the similar approach in [41], we obtain the basic reproduction number as follows

$$F = \begin{pmatrix} 0 & 0 & 0 & 0 & \beta_{MAL} b \\ 0 & 0 & 0 & \frac{q_{CHO}\mathcal{S}^*_{HB}}{\kappa} & 0 \\ 0 & 0 & 0 & 0 & 0 \\ 0 & 0 & 0 & 0 & 0 \\ \frac{\beta_{VEC}\mathcal{S}^*_{VEC}}{\mathcal{N}^*_{HB}} & 0 & \frac{\beta_{VEC}\mathcal{S}^*_{VEC}}{\mathcal{N}^*_{HB}} & 0 & 0 \end{pmatrix},$$

$$V = \begin{pmatrix} \mathcal{A}_1 & 0 & 0 & 0 & 0 \\ 0 & \mathcal{A}_2 & 0 & 0 & 0 \\ 0 & 0 & \mathcal{A}_3 & 0 & 0 \\ 0 & -\rho_1 & -\rho_2 & \mu & 0 \\ 0 & 0 & 0 & 0 & \mu \end{pmatrix},$$

where

$$\mathcal{A}_1 = \mu_{HB} + \delta_{MAL} + \gamma_{MAL}, \quad \mathcal{A}_2 = \delta_{CHO} + \mu_{HB} + \gamma_{CHO}, \quad \mathcal{A}_3 = \mu_{HB} + \delta_{MAC} + \gamma_{MAC}.$$

After elementary algebra, we obtain the basic reproduction number $\mathcal{R}_0 = \max\{\mathcal{R}_{0P}, \mathcal{R}_{0T}\}$, where

$$\mathcal{R}_{0P} = \sqrt{\frac{b\beta_{MAL}\beta_{VEC}b\mathcal{S}_{VEC}}{N^*_h \mathcal{A}_1 \mu_{VEC}}}, \qquad \mathcal{R}_{0T} = \frac{\rho_1 q_{CHO} S^*_h}{\kappa \mu \mathcal{A}_2}.$$

Theorem 1 *The DFE, $\mathcal{T}_0$, of the fractional Malaria and Cholera model (1) is locally asymptotically stable*

(LAS) if $\mathcal{R}_0 < 1$, *and unstable if* $\mathcal{R}_0 > 1$.

Proof The Jacobian matrix of the malaria and cholera fractional order model (1) evaluated at the disease-free equilibrium, $\mathcal{T}_0$ is given by:

$$J(\mathcal{T}_0) = \begin{pmatrix} -\mu_{HB} & 0 & \omega_{MAL} & 0 & \omega_{CHO} & 0 & \omega_{mc} & -\frac{q_{CHO}\mathcal{S}^*_{HB}}{N^*_{HB}} & 0 & -\beta_{MAL}b \\ 0 & -\mathcal{A}_1 & 0 & 0 & 0 & 0 & 0 & 0 & 0 & \beta_{MAL}b \\ 0 & \gamma_{MAL} & -Q_1 & 0 & 0 & 0 & 0 & 0 & 0 & 0 \\ 0 & 0 & 0 & -\mathcal{A}_2 & 0 & 0 & 0 & \frac{q_{CHO}\mathcal{S}^*_{HB}}{\kappa} & 0 & 0 \\ 0 & 0 & 0 & \gamma_{CHO} & -Q_2 & 0 & 0 & 0 & 0 & 0 \\ 0 & 0 & 0 & 0 & 0 & -\mathcal{A}_3 & 0 & 0 & 0 & 0 \\ 0 & 0 & 0 & 0 & 0 & \gamma_{MAC} & -Q_3 & 0 & 0 & 0 \\ 0 & 0 & 0 & \rho_1 & 0 & \rho_2 & 0 & -\mu_{DBR} & 0 & 0 \\ 0 & -\theta & 0 & 0 & 0 & -\theta & 0 & 0 & -\mu_{VEC} & 0 \\ 0 & \theta & 0 & 0 & 0 & \theta & 0 & 0 & 0 & -\mu_{VEC} \end{pmatrix},$$

where

$$\mathcal{A}_1 = \mu_{HB} + \delta_{MAL} + \gamma_{MAL}, \quad \mathcal{A}_2 = \delta_{CHO} + \mu_{HB} + \gamma_{CHO}, \quad \mathcal{A}_3 = \mu_{HB} + \delta_{MAC} + \gamma_{MAC},$$
$$Q_1 = \mu + \omega_{MAL}, Q_2 = \mu + \omega_{CHO}, Q_3 = \mu + \omega_{mc}, \theta = \frac{\beta_{VEC}bS^*_v}{N^*_h}.$$

Thus the eigenvalues are as follows $\lambda_1 = -Q_1$, $\lambda_2 = -Q_2$, $\lambda_3 = -Q_3$, $\lambda_4 = -\mathcal{A}_3$, $\lambda_5 = -\mu_{HB}$, $\lambda_6 = -\mu_{VEC}$ and the following characteristic equations given below

$$\left(-b\theta\beta_{MAL}\left(\lambda + \mathcal{A}_1\right)\left(\lambda + \mu_{VEC}\right)\right)\left(1 - \mathcal{R}_{0P}\right) = 0,$$

and

$$\left(\left(\lambda + \mathcal{A}_2\right)\left(\lambda + \mu_{DBR}\right)\frac{\rho_1 q_{CHO}S^*_h}{\kappa}\right)\left(1 - \mathcal{R}_{0T}\right) = 0.$$

By the Routh-Hurwitz criterion, the above equations will possess negative real roots if and only if $\mathcal{R}_{0P} < 1$ and $\mathcal{R}_{0T} < 1$, respectively. Hence, the DFE, $\mathcal{T}_0$ is locally asymptotically stable if $\mathcal{R}_0 = \max\{\mathcal{R}_{0P}, \mathcal{R}_{0T}\} < 1$. ■

Existence and uniqueness of solution

Here, we present the existence and uniqueness of the formulated fractional order system (1) using fixed point theorems. For this purpose, we rewrite malaria and cholera fractional co–dynamic model as

$$^{CF}\mathcal{D}^{\alpha}\mathcal{S}_{HB}(t) = \mathcal{Q}_1\left(t, \mathcal{S}_{HB}, \mathcal{I}_{MAL}, \mathcal{R}_{MAL}, \mathcal{I}_{CHO}, \mathcal{R}_{CHO}, \mathcal{I}_{MAC}, \mathcal{R}_{MAC}, \mathcal{B}_{CHO}, \mathcal{S}_{VEC}, \mathcal{I}_{VEC}\right),$$
$$^{CF}\mathcal{D}^{\alpha}\mathcal{I}_{MAL}(t) = \mathcal{Q}_2\left(t, \mathcal{S}_{HB}, \mathcal{I}_{MAL}, \mathcal{R}_{MAL}, \mathcal{I}_{CHO}, \mathcal{R}_{CHO}, \mathcal{I}_{MAC}, \mathcal{R}_{MAC}, \mathcal{B}_{CHO}, \mathcal{S}_{VEC}, \mathcal{I}_{VEC}\right),$$

$$
\begin{aligned}
{}^{CF}\mathcal{D}^{\alpha}\mathcal{R}_{MAL}(t) &= \mathcal{Q}_3\left(t,\mathcal{S}_{HB},\mathcal{I}_{MAL},\mathcal{R}_{MAL},\mathcal{I}_{CHO},\mathcal{R}_{CHO},\mathcal{I}_{MAC},\mathcal{R}_{MAC},\mathcal{B}_{CHO},\mathcal{S}_{VEC},\mathcal{I}_{VEC}\right),\\
{}^{CF}\mathcal{D}^{\alpha}\mathcal{I}_{CHO}(t) &= \mathcal{Q}_4\left(t,\mathcal{S}_{HB},\mathcal{I}_{MAL},\mathcal{R}_{MAL},\mathcal{I}_{CHO},\mathcal{R}_{CHO},\mathcal{I}_{MAC},\mathcal{R}_{MAC},\mathcal{B}_{CHO},\mathcal{S}_{VEC},\mathcal{I}_{VEC}\right),\\
{}^{CF}\mathcal{D}^{\alpha}\mathcal{R}_{CHO}(t) &= \mathcal{Q}_5\left(t,\mathcal{S}_{HB},\mathcal{I}_{MAL},\mathcal{R}_{MAL},\mathcal{I}_{CHO},\mathcal{R}_{CHO},\mathcal{I}_{MAC},\mathcal{R}_{MAC},\mathcal{B}_{CHO},\mathcal{S}_{VEC},\mathcal{I}_{VEC}\right),\\
{}^{CF}\mathcal{D}^{\alpha}\mathcal{I}_{MAC}(t) &= \mathcal{Q}_6\left(t,\mathcal{S}_{HB},\mathcal{I}_{MAL},\mathcal{R}_{MAL},\mathcal{I}_{CHO},\mathcal{R}_{CHO},\mathcal{I}_{MAC},\mathcal{R}_{MAC},\mathcal{B}_{CHO},\mathcal{S}_{VEC},\mathcal{I}_{VEC}\right),\\
{}^{CF}\mathcal{D}^{\alpha}\mathcal{R}_{MAC}(t) &= \mathcal{Q}_7\left(t,\mathcal{S}_{HB},\mathcal{I}_{MAL},\mathcal{R}_{MAL},\mathcal{I}_{CHO},\mathcal{R}_{CHO},\mathcal{I}_{MAC},\mathcal{R}_{MAC},\mathcal{B}_{CHO},\mathcal{S}_{VEC},\mathcal{I}_{VEC}\right),\\
{}^{CF}\mathcal{D}^{\alpha}\mathcal{B}_{CHO}(t) &= \mathcal{Q}_8\left(t,\mathcal{S}_{HB},\mathcal{I}_{MAL},\mathcal{R}_{MAL},\mathcal{I}_{CHO},\mathcal{R}_{CHO},\mathcal{I}_{MAC},\mathcal{R}_{MAC},\mathcal{B}_{CHO},\mathcal{S}_{VEC},\mathcal{I}_{VEC}\right),\\
{}^{CF}\mathcal{D}^{\alpha}\mathcal{S}_{VEC}(t) &= \mathcal{Q}_9\left(t,\mathcal{S}_{HB},\mathcal{I}_{MAL},\mathcal{R}_{MAL},\mathcal{I}_{CHO},\mathcal{R}_{CHO},\mathcal{I}_{MAC},\mathcal{R}_{MAC},\mathcal{B}_{CHO},\mathcal{S}_{VEC},\mathcal{I}_{VEC}\right),\\
{}^{CF}\mathcal{D}^{\alpha}\mathcal{I}_{VEC}(t) &= \mathcal{Q}_{10}\left(t,\mathcal{S}_{HB},\mathcal{I}_{MAL},\mathcal{R}_{MAL},\mathcal{I}_{CHO},\mathcal{R}_{CHO},\mathcal{I}_{MAC},\mathcal{R}_{MAC},\mathcal{B}_{CHO},\mathcal{S}_{VEC},\mathcal{I}_{VEC}\right),
\end{aligned}
\tag{10}
$$

where $\mathcal{Q}_j = \mathcal{Q}_j\left(t,\mathcal{S}_{HB},\mathcal{I}_{MAL},\mathcal{R}_{MAL},\mathcal{I}_{CHO},\mathcal{R}_{CHO},\mathcal{I}_{MAC},\mathcal{R}_{MAC},\mathcal{B}_{CHO},\mathcal{S}_{VEC},\mathcal{I}_{VEC}\right)$, for $j = 1,2,\ldots,10$ is given by

$$
\begin{cases}
\mathcal{Q}_1 = \Lambda_{HB} - \frac{\beta_{MAL} b \mathcal{I}_{VEC}}{N_h}\mathcal{S}_{HB} - \frac{\mathcal{B}_{CHO}\alpha}{\kappa+\mathcal{B}_{CHO}}\mathcal{S}_{HB} - \mu_{HB}\mathcal{S}_{HB} + \omega_{MAL}\mathcal{R}_{MAL} + \omega_{CHO}\mathcal{R}_{CHO} + \omega_{mc}\mathcal{R}_{MAC},\\
\mathcal{Q}_2 = \beta_{MAL} b \frac{\mathcal{I}_{VEC}}{\mathcal{N}_{HB}}(\mathcal{S}_{HB} + \mathcal{R}_{CHO}) - (\mu_{HB} + \delta_{MAL} + \gamma_{MAL})\mathcal{I}_{MAL} + \frac{\mathcal{B}_{CHO} q_{CHO}}{\kappa+\mathcal{B}_{CHO}}\mathcal{I}_{MAL},\\
\mathcal{Q}_3 = \gamma_{MAL}\mathcal{I}_{MAL} - (\mu + \omega_{MAL})\mathcal{R}_{MAL} - \frac{\mathcal{B}_{CHO}\alpha}{\kappa+\mathcal{B}_{CHO}}\mathcal{R}_{MAL},\\
\mathcal{Q}_4 = \frac{\beta_c \alpha}{\kappa+\mathcal{B}_{CHO}}(\mathcal{S}_{HB} + \mathcal{R}_{MAL}) - (\delta_{CHO} + \mu_{HB} + \gamma_{CHO})\mathcal{I}_{CHO} - \frac{\beta_{VEC} b \mathcal{I}_{VEC}}{\mathcal{N}_{HB}}\mathcal{I}_{CHO},\\
\mathcal{Q}_5 = \gamma_{CHO}\mathcal{I}_{CHO} - (\mu_{HB} + \omega_{CHO})\mathcal{R}_{CHO} - \frac{\beta_{MAL} b \mathcal{I}_{VEC}}{\mathcal{N}_{HB}}\mathcal{R}_{CHO},\\
\mathcal{Q}_6 = \frac{\mathcal{B}_{CHO}\alpha}{\kappa+\mathcal{B}_{CHO}}\mathcal{I}_{MAL} + \frac{\beta_{MAL} b \mathcal{I}_{VEC}}{\mathcal{N}_{HB}}\mathcal{I}_{CHO} - (\mu_{HB} + \delta_{MAC} + \gamma_{MAC})\mathcal{I}_{MAC},\\
\mathcal{Q}_7 = \gamma_{MAC}\mathcal{I}_{CHO} - (\mu_{HB} + \omega_{mc})\mathcal{R}_{MAC},\\
\mathcal{Q}_8 = r\mathcal{B}_{CHO}\left(1 - \frac{\mathcal{B}_{CHO}}{K}\right) + \xi_{MP1}\mathcal{I}_{CHO} + \xi_{MP2}\mathcal{I}_{MAC} - \mu_{DBR}\mathcal{B}_{CHO},\\
\mathcal{Q}_9 = \Lambda_{VEC} - \frac{\beta_{VEC} b(\mathcal{I}_{MAL}+\mathcal{I}_{MAC})}{\mathcal{N}_{HB}}\mathcal{S}_{VEC} - \mu_{VEC}\mathcal{S}_{VEC},\\
\mathcal{Q}_{10} = \frac{\beta_{VEC} b(\mathcal{I}_{MAL}+\mathcal{I}_{MAC})}{\mathcal{N}_{HB}}\mathcal{S}_{VEC} - \mu_{VEC}\mathcal{I}_{VEC}.
\end{cases}
\tag{11}
$$

Using the above illustration, malaria and cholera fractional order co–dynamic model (1) can be written as

$$
\begin{cases}
{}^{CF}\mathcal{D}_t^{\alpha}\Omega_{MC}(t) = \mathcal{K}(t,\Omega_{MC}(t)), & 0 < \alpha \leq 1, \qquad t \in \mathcal{J} = [0,T],\\
\Omega_{MC}(0) = \Omega_{MC0} \geq 0,
\end{cases}
\tag{12}
$$

where $\mathcal{K} : \mathcal{J} \times \mathbb{R} \to \mathbb{R}$ is continuous and

$$
\begin{cases}
\Omega_{MC}(t) = \left(\mathcal{S}_{HB},\mathcal{I}_{MAL},\mathcal{R}_{MAL},\mathcal{I}_{CHO},\mathcal{R}_{CHO},\mathcal{I}_{MAC},\mathcal{R}_{MAC},\mathcal{B}_{CHO},\mathcal{S}_{VEC},\mathcal{I}_{VEC}\right)^T,\\
\Omega_{MC0} = \left(S_{h0}, I_{m0}, R_{m0}, I_{c0}, R_{c0}, I_{MC0}, R_{MC0}, B_{c0}, S_{v0}, I_{v0}\right)^T,\\
\mathcal{K}(t,\Omega_{MC}(t)) = \mathcal{Q}_j\left(t,\mathcal{S}_{HB},\mathcal{I}_{MAL},\mathcal{R}_{MAL},\mathcal{I}_{CHO},\mathcal{R}_{CHO},\mathcal{I}_{MAC},\mathcal{R}_{MAC},\mathcal{B}_{CHO},\mathcal{S}_{VEC},\mathcal{I}_{VEC}\right)^T,
\end{cases}
\tag{13}
$$

where $j = 1,2,3,\ldots 10$, and $(.)^T$ denotes the transpose of the vector. Using Lemma (1), the initial value problem (12) is equivalent to the following fractional order Volterra integral equation

$$
\Omega_{MC}(t) = \Omega_{MC0} + \frac{2(1-\alpha)}{(2-\alpha)\mathcal{U}(\alpha)}\left(\mathcal{K}(t,\Omega_{MC}(t)) - \mathcal{K}_0\right) + \frac{2\alpha}{(2-\alpha)\mathcal{U}(\alpha)}\int_0^t \mathcal{K}(\zeta,\Omega_{MC}(\zeta))d\zeta, \tag{14}
$$

where $t \geq 0$.
Furthermore, let us define $C(\mathcal{J}, \mathbb{R})$ as the Banach space of continuous functions from $\mathcal{J} = [0, T]$ into $\mathbb{R}$ endowed with the Chebyshev norm

$$\|\Omega_{MC}\|_{\infty} := \sup_{t \in \mathcal{J}} \{|\Omega_{MC}(t)|\}, \qquad \mathcal{J} = [0, T].$$

Theorem 2 *Assume that* ***(B1):*** *There exists a Lipschitz constant* $\mathcal{L}_{MC} > 0$, *such that*

$$|\mathcal{K}(t, \Omega_{MC1}(t)) - \mathcal{K}(t, \Omega_{MC2}(t))| \leq \mathcal{L}_{MC} |\Omega_{MC1}(t) - \Omega_{MC2}(t)|, \quad t \in \mathcal{J} = [0, T], \quad \Omega_{MC1}, \Omega_{MC2} \in \mathbb{R},$$

then if

$$\mathcal{L}_{MC} \left(\frac{2(1-\alpha)}{(2-\alpha)\mathcal{U}(\alpha)} + \frac{2\alpha T_{\max}}{(2-\alpha)\mathcal{U}(\alpha)} \right) < 1, \tag{15}$$

the initial value problem (1) *has a unique solution on* $\mathcal{J} = [0, T]$.

Proof Consider the transformed initial value problem (12) plugged into a fixed point quantity under the operation

$$\Phi : C^m(\mathcal{J}, \mathbb{R}) \to C^m(\mathcal{J}, \mathbb{R}),$$

with the corresponding definition as follows,

$$\begin{aligned} \Phi\Omega_{MC}(t) &= \Omega_{MC0} + \frac{2(1-\alpha)}{(2-\alpha)\mathcal{U}(\alpha)} \left(\mathcal{K}(t, \Omega_{MC}(t)) - \mathcal{K}(0, \Omega_{MC}(0)) \right) \\ &\quad + \frac{2\alpha}{(2-\alpha)\mathcal{U}(\alpha)} \int_0^t \mathcal{K}(\zeta, \Omega_{MC}(\zeta)) d\zeta. \end{aligned} \tag{16}$$

Next, we apply the Banach contraction principle to prove that the quantity Φ has a unique fixed point. In that case, we let the two solutions $\Omega_{MC1}(t), \Omega_{MC2}(t) \in C^m(\mathcal{J}, \mathbb{R})$, where $\mathcal{J} = [0, T]$, then we have:

$$\begin{aligned} |\Phi\Omega_{MC1}(t) - \Phi\Omega_{MC2}(t)| &\leq \frac{2(1-\alpha)}{(2-\alpha)\mathcal{U}(\alpha)} |\mathcal{K}(t, \Omega_{MC1}(t)) - \mathcal{K}(t, \Omega_{MC2}(t))| \\ &+ \frac{2\alpha}{(2-\alpha)\mathcal{U}(\alpha)} \int_0^t |\mathcal{K}(\zeta, \Omega_{MC1}(\zeta)) - \mathcal{K}(\zeta, \Omega_{MC2}(\zeta))| \, d\zeta \\ &\leq \mathcal{L}_{MC} \left(\frac{2(1-\alpha)}{(2-\alpha)\mathcal{U}(\alpha)} + \frac{2\alpha T_{\max}}{(2-\alpha)\mathcal{U}(\alpha)} \right) |\Omega_{MC1}(t) - \Omega_{MC2}(t)|_{\infty}. \end{aligned}$$

Thus,

$$\|\Phi\Omega_{MC1}(t) - \Phi\Omega_{MC2}(t)\|_{\infty} \leq \mathcal{L}_{MC} \left(\frac{2(1-\alpha)}{(2-\alpha)\mathcal{U}(\alpha)} + \frac{2\alpha T_{\max}}{(2-\alpha)\mathcal{U}(\alpha)} \right) |\Omega_{MC1}(t) - \Omega_{MC2}(t)|_{\infty}.$$

Applying (15), we see that the operator Φ is a contraction and hence possesses a fixed point, and hence, (1) has a unique solution. ■

Theorem 3 *Assume that*
(B2): *The function* $\mathcal{K} : \mathcal{J} \times \mathbb{R} \to \mathbb{R}$ *is totally continuous.*
(B3): *There exists a constant* $\mathcal{G}_{MC} > 0$ *such that*

$$|\mathcal{K}(t, \Omega_{MC}(t))| \leq \mathcal{G}_{MC}, \quad \text{for all } t \in \mathcal{J} = [0, T], \quad \Omega_{MC} \in \mathbb{R},$$

then the malaria and cholera fractional order system (1) *with its corresponding initial condition* (2) *has at least one solution on* $\mathcal{J} = [0, T]$.

Proof Following a similar process in [15], we apply Schauder's fixed point theorem to illustrate that Φ, defined by (16) possesses a fixed point. Thus consider the following steps;
STEP (1): The operator $\Phi : C^m(\mathcal{J}, \mathbb{R}) \to C^m(\mathcal{J}, \mathbb{R})$ is totally continuous. Define the function Ω_{MC} as a sequence $\left\{\Omega_{MC(m)}\right\}$ such that $\Omega_{MC(m)} \to \Omega_{MC}$ in $C(\mathcal{J}, \mathbb{R})$. Thus, for each $t \in \mathcal{J} = [0, T]$, we have

$$\begin{aligned}
&\left|\Phi\Omega_{MC(m)}(t) - \Phi\Omega_{MC}(t)\right| \\
= &\left|\frac{2(1-\alpha)}{(2-\alpha)\mathcal{U}(\alpha)}\left(\mathcal{K}(t, \Omega_{MC(m)}(t)) - \mathcal{K}(0, \Omega_{MC}(0))\right) + \frac{2\alpha}{(2-\alpha)\mathcal{U}(\alpha)}\int_0^t \mathcal{K}(\zeta, \Omega_{MC(m)}(\zeta))d\zeta\right. \\
&\left. - \left(\frac{2(1-\alpha)}{(2-\alpha)\mathcal{U}(\alpha)}\left(\mathcal{K}(t, \Omega_{MC}(t)) - \mathcal{K}(0, \Omega_{MC}(0))\right) + \frac{2\alpha}{(2-\alpha)\mathcal{U}(\alpha)}\int_0^t \mathcal{K}(\zeta, \Omega_{MC}(\zeta))d\zeta\right)\right| \\
\leq &\frac{2(1-\alpha)}{(2-\alpha)\mathcal{U}(\alpha)}\left|\mathcal{K}(t, \Omega_{MC(m)}(t)) - \mathcal{K}(t, \Omega_{MC}(t))\right| \\
&+ \frac{2\alpha}{(2-\alpha)\mathcal{U}(\alpha)}\int_0^t \left|\mathcal{K}(\zeta, \Omega_{MC(m)}(\zeta)) - \mathcal{K}(\zeta, \Omega_{MC}(\zeta))\right| d\zeta \\
\leq &\frac{2(1-\alpha)}{(2-\alpha)\mathcal{U}(\alpha)}\sup_{t\in\mathcal{J}}\left|\mathcal{K}(\zeta, \Omega_{MC(m)}(\zeta)) - \mathcal{K}(t, \Omega_{MC}(t))\right| + \frac{2\alpha}{(2-\alpha)\mathcal{U}(\alpha)} \\
\times &\int_0^t \sup_{t\in\mathcal{J}}\left|\mathcal{K}(\zeta, \Omega_{MC(m)}(\zeta)) - \mathcal{K}(\zeta, \Omega_{MC}(\zeta))\right| d\zeta,
\end{aligned}$$

such that

$$\left|\Phi\Omega_{MC(m)}(t) - \Phi\Omega_{MC}(t)\right| \leq \left\|\mathcal{K}(., \Omega_{MC(m)}(.)) - \mathcal{K}(., \Omega_{MC}(.))\right\|_\infty \left(\frac{2(1-\alpha)}{(2-\alpha)\mathcal{U}(\alpha)} + \frac{2\alpha T_{\max}}{(2-\alpha)\mathcal{U}(\alpha)}\right).$$

Since $\mathcal{K}$ is continuous, clearly,

$$\left\|\Phi\Omega_{MC(m)}(t) - \Phi\Omega_{MC}(t)\right\|_\infty \leq \left(\frac{2(1-\alpha)}{(2-\alpha)\mathcal{U}(\alpha)} + \frac{2\alpha T_{\max}}{(2-\alpha)\mathcal{U}(\alpha)}\right)\left\|\mathcal{K}(., \Omega_{MC(m)}(.)) - \mathcal{K}(., \Omega_{MC}(.))\right\|_\infty.$$

Hence, $\left\|\Phi\Omega_{MC(m)}(t) - \Phi\Omega_{MC}(t)\right\|_\infty \to 0$ as $p \to \infty$.

STEP (2): Φ maps a "bounded set into another bounded" set in $C(\mathcal{J}, \mathbb{R})$.
Therefore, for every real number $\bar{k} > 0$, it can be shown that there exists an associated real number $\chi > o$ such that

$$\mathcal{B}_{\bar{k}} = \left\{\Omega_{MC} \in C(\mathcal{J}.\mathbb{R}) : \|\Omega_{MC}\|_\infty \leq \bar{k}\right\}, \quad \|\Phi\Omega_{MC}\|_\infty \leq \chi, \quad \forall \Omega_{MC} \in \mathcal{B}_{\bar{k}}.$$

Thus $\forall t \in \mathcal{J} = [0, T]$, from (16) and **(B3)** that

$$\begin{aligned} |\Phi\Omega_{MC}(t)| &\leq \frac{2(1-\alpha)}{(2-\alpha)\mathcal{U}(\alpha)} |\mathcal{K}(t, \Omega_{MC}(t))| + \frac{2\alpha}{(2-\alpha)\mathcal{U}(\alpha)} \int_0^t |\mathcal{K}(\zeta, \Omega_{MC}(\zeta))| \, d\zeta \\ &\leq \mathcal{G}_{MC} \left(\frac{2(1-\alpha)}{(2-\alpha)\mathcal{U}(\alpha)} + \frac{2\alpha T_{\max}}{(2-\alpha)\mathcal{U}(\alpha)} \right). \end{aligned}$$

Thus $\|\Phi\Omega_{MC}\|_\infty \leq \chi$, where

$$\chi = \mathcal{G}_{MC} \left(\frac{2(1-\alpha)}{(2-\alpha)\mathcal{U}(\alpha)} + \frac{2\alpha T_{\max}}{(2-\alpha)\mathcal{U}(\alpha)} \right).$$

STEP (3): The operator $\Phi : C^m(\mathcal{J}, \mathbb{R}) \to C^m(\mathcal{J}, \mathbb{R})$ maps a bounded set into equi-continuous set in $C(\mathcal{J}, \mathbb{R})$. Let $t_1, t_2 \in \mathcal{J} = [0, T]$ and $t_2 > t_1$ and let $\mathcal{B}_{\bar{k}}$ be bounded set of $C(\mathcal{J}, \mathbb{R})$ as defined above and $\Omega_{MC} \in \mathcal{B}_{\bar{k}}$, then using (16), **(B3)** and triangle inequality, we have

$$\begin{aligned} |\Phi\Omega_{MC}(t_2) - \Phi\Omega_{MC}(t_1)| &= \left| \frac{2(1-\alpha)}{(2-\alpha)\mathcal{U}(\alpha)} (\mathcal{K}(t_2, \Omega_{MC}(t_2))) + \frac{2\alpha}{(2-\alpha)\mathcal{U}(\alpha)} \int_0^{t_2} \mathcal{K}(\zeta, \Omega_{MC}(\zeta)) d\zeta \right. \\ &\quad \left. - \left(\frac{2(1-\alpha)}{(2-\alpha)\mathcal{U}(\alpha)} (\mathcal{K}(t_1, \Omega_{MC}(t_1))) + \frac{2\alpha}{(2-\alpha)\mathcal{U}(\alpha)} \int_0^{t_1} \mathcal{K}(\zeta, \Omega_{MC}(\zeta)) d\zeta \right) \right| \\ &= \left| \frac{2(1-\alpha)}{(2-\alpha)\mathcal{U}(\alpha)} (\mathcal{K}(t_2, \Omega_{MC}(t_2)) - \mathcal{K}(t_1, \Omega_{MC}(t_1))) + \frac{2\alpha}{(2-\alpha)\mathcal{U}(\alpha)} \right. \\ &\quad \left. \times \left(\int_0^{t_2} \mathcal{K}(\zeta, \Omega_{MC(m)}(\zeta)) - \int_0^{t_2} \mathcal{K}(\zeta, \Omega_{MC}(\zeta)) \right) d\zeta \right| \\ &\leq \frac{2(1-\alpha)}{(2-\alpha)\mathcal{U}(\alpha)} (|\mathcal{K}(t_2, \Omega_{MC}(t_2)) - \mathcal{K}(t_1, \Omega_{MC}(t_1))|) \\ &\quad + \frac{2\alpha}{(2-\alpha)\mathcal{U}(\alpha)} \int_{t_1}^{t_2} |\mathcal{K}(\zeta, \Omega_{MC}(\zeta))| \, d\zeta \\ &\leq \frac{2(1-\alpha)(2\mathcal{G}_{MC})}{(2-\alpha)\mathcal{U}(\alpha)} + \frac{2\alpha\mathcal{G}_{MC}}{(2-\alpha)\mathcal{U}(\alpha)} \int_{t_1}^{t_2} d\zeta \\ &= \mathcal{G}_{MC} \left(\frac{4(1-\alpha)}{(2-\alpha)\mathcal{U}(\alpha)} + \frac{2\alpha(t_2 - t_1)}{(2-\alpha)\mathcal{U}(\alpha)} \right). \end{aligned}$$

The right-hand side of the above inequality tends to zero as $t_1 \to t_2$. Thus, from **STEPS** (1) to (2) and also recalling the Arzela-Ascoli's theorem, the operator $\Phi : C^m(\mathcal{J}, \mathbb{R}) \to C^m(\mathcal{J}, \mathbb{R})$ is totally continuous.

STEP (4): The boundedness of priori: Let

$$\xi = \{\Omega_{MC} \in C(\mathcal{J}, \mathbb{R}) : \Omega_{MC} = \Lambda\Phi\Omega_{MC}\},$$

for some $\Lambda \in (0, 1)$. We show that set ξ is bounded. Let $\Omega_{MC} \in \xi$, then $\Omega_{MC} = \Lambda\Phi\Omega_{MC}$ for some $\Lambda \in (0, 1)$. Thus for all $t \in \mathcal{J}$, we have that

$$\begin{aligned} \Omega_{MC} &= \Lambda\Phi\Omega_{MC} \\ &= \Lambda \left(\frac{2(1-\alpha)}{(2-\alpha)\mathcal{U}(\alpha)} (\mathcal{K}(t_2, \Omega_{MC}(t_2))) + \frac{2\alpha}{(2-\alpha)\mathcal{U}(\alpha)} \int_0^{t_2} \mathcal{K}(\zeta, \Omega_{MC}(\zeta)) d\zeta \right). \end{aligned}$$

Using **(B3)** and **STEP (2)** we get

$$\begin{aligned}|\Omega_{MC}| &= \Lambda\left(\frac{2(1-\alpha)}{(2-\alpha)\mathcal{U}(\alpha)}|\mathcal{K}(t_2,\Omega_{MC}(t_2))| + \frac{2\alpha}{(2-\alpha)\mathcal{U}(\alpha)}\int_0^{t_2}|\mathcal{K}(\zeta,\Omega_{MC}(\zeta))|\,d\zeta\right)\\ &\leq \mathcal{G}\left(\frac{2(1-\alpha)}{(2-\alpha)\mathcal{U}(\alpha)} + \frac{2\alpha T_{\max}}{(2-\alpha)\mathcal{U}(\alpha)}\right).\end{aligned}$$

Thus, for every $t \in \mathcal{J} = [0, T]$,

$$\|\Omega_{MC}\|_\infty \leq \mathcal{G}\left(\frac{2(1-\alpha)}{(2-\alpha)\mathcal{U}(\alpha)} + \frac{2\alpha T_{\max}}{(2-\alpha)\mathcal{U}(\alpha)}\right) := \chi, \qquad \chi \in \mathbb{R},$$

which is the boundedness of set ξ. Applying Schauder's fixed point theorem, the operator Φ possesses a unique fixed point which is the solution of the IVP (12). Thus malaria and cholera co–dynamic fractional order system (1) solution exists. ■

5 Numerical scheme

In this section, we apply a numerical algorithm to the proposed malaria and cholera fractional order system to obtain the numerical solution of the proposed system. The numerical scheme proposed and proved by Toufik and Atangana [42] which has a tremendous convergence property is applied to approximate the fractional order malaria and cholera system. Using the initial condition (2) and the Atangana–Baleanu integral (5), we obtain the following Atangana–Baleanu fractional Volterra equation of the system (1) as;

$$\begin{aligned}
\mathcal{S}_{HB}(t) - \mathcal{S}_{HB}(0) &= \frac{(1-\alpha)}{\mathcal{U}(\alpha)}\mathcal{Q}_1\left(t, \mathcal{S}_{HB}(t)\right) + \frac{\alpha}{\mathcal{U}(\alpha)\Gamma(\alpha)}\int_0^t (t-\zeta)^{\alpha-1}\mathcal{Q}_1\left(\zeta, \mathcal{S}_{HB}(\zeta)\right)d\zeta,\\
\mathcal{I}_{MAL}(t) - \mathcal{I}_{MAL}(0) &= \frac{(1-\alpha)}{\mathcal{U}(\alpha)}\mathcal{Q}_2\left(t, \mathcal{I}_{MAL}(t)\right) + \frac{\alpha}{\mathcal{U}(\alpha)\Gamma(\alpha)}\int_0^t (t-\zeta)^{\alpha-1}\mathcal{Q}_2\left(\zeta, \mathcal{I}_{MAL}(\zeta)\right)d\zeta,\\
\mathcal{R}_{MAL}(t) - \mathcal{R}_{MAL}(0) &= \frac{(1-\alpha)}{\mathcal{U}(\alpha)}\mathcal{Q}_3\left(t, \mathcal{R}_{MAL}(t)\right) + \frac{\alpha}{\mathcal{U}(\alpha)\Gamma(\alpha)}\int_0^t (t-\zeta)^{\alpha-1}\mathcal{Q}_3\left(\zeta, \mathcal{R}_{MAL}(\zeta)\right)d\zeta,\\
\mathcal{I}_{CHO}(t) - \mathcal{I}_{CHO}(0) &= \frac{(1-\alpha)}{\mathcal{U}(\alpha)}\mathcal{Q}_4\left(t, \mathcal{I}_{CHO}(t)\right) + \frac{\alpha}{\mathcal{U}(\alpha)\Gamma(\alpha)}\int_0^t (t-\zeta)^{\alpha-1}\mathcal{Q}_4\left(\zeta, \mathcal{I}_{CHO}(\zeta)\right)d\zeta,\\
\mathcal{R}_{CHO}(t) - \mathcal{R}_{CHO}(0) &= \frac{(1-\alpha)}{\mathcal{U}(\alpha)}\mathcal{Q}_5\left(t, \mathcal{R}_{CHO}(t)\right) + \frac{\alpha}{\mathcal{U}(\alpha)\Gamma(\alpha)}\int_0^t (t-\zeta)^{\alpha-1}\mathcal{Q}_5\left(\zeta, \mathcal{R}_{CHO}(\zeta)\right)d\zeta,\\
\mathcal{I}_{MAC}(t) - \mathcal{I}_{MAC}(0) &= \frac{(1-\alpha)}{\mathcal{U}(\alpha)}\mathcal{Q}_6\left(t, \mathcal{I}_{MAC}(t)\right) + \frac{\alpha}{\mathcal{U}(\alpha)\Gamma(\alpha)}\int_0^t (t-\zeta)^{\alpha-1}\mathcal{Q}_6\left(\zeta, \mathcal{I}_{MAC}(\zeta)\right)d\zeta,\\
\mathcal{R}_{MAC}(t) - \mathcal{R}_{MAC}(0) &= \frac{(1-\alpha)}{\mathcal{U}(\alpha)}\mathcal{Q}_7\left(t, \mathcal{R}_{MAC}(t)\right) + \frac{\alpha}{\mathcal{U}(\alpha)\Gamma(\alpha)}\int_0^t (t-\zeta)^{\alpha-1}\mathcal{Q}_7\left(\zeta, \mathcal{R}_{MAC}(\zeta)\right)d\zeta,\\
\mathcal{B}_{CHO}(t) - \mathcal{B}_{CHO}(0) &= \frac{(1-\alpha)}{\mathcal{U}(\alpha)}\mathcal{Q}_8\left(t, \mathcal{B}_{CHO}(t)\right) + \frac{\alpha}{\mathcal{U}(\alpha)\Gamma(\alpha)}\int_0^t (t-\zeta)^{\alpha-1}\mathcal{Q}_8\left(\zeta, \mathcal{B}_{CHO}(\zeta)\right)d\zeta,\\
\mathcal{S}_{VEC}(t) - \mathcal{S}_{VEC}(0) &= \frac{(1-\alpha)}{\mathcal{U}(\alpha)}\mathcal{Q}_9\left(t, \mathcal{S}_{VEC}(t)\right) + \frac{\alpha}{\mathcal{U}(\alpha)\Gamma(\alpha)}\int_0^t (t-\zeta)^{\alpha-1}\mathcal{Q}_9\left(\zeta, \mathcal{S}_{VEC}(\zeta)\right)d\zeta,\\
\mathcal{I}_{VEC}(t) - \mathcal{I}_{VEC}(0) &= \frac{(1-\alpha)}{\mathcal{U}(\alpha)}\mathcal{Q}_{10}\left(t, \mathcal{I}_{VEC}(t)\right) + \frac{\alpha}{\mathcal{U}(\alpha)\Gamma(\alpha)}\int_0^t (t-\zeta)^{\alpha-1}\mathcal{Q}_{10}\left(\zeta, \mathcal{I}_{VEC}(\zeta)\right)d\zeta.
\end{aligned} \tag{17}$$

Next, setting $t = t_{m+1}$ for $m = 0, 1, 2, \ldots$ into the above equation (17), we get

$$\begin{aligned}
\mathcal{S}_{HB}(t_{m+1}) - \mathcal{S}_{HB}(0) &= \frac{(1-\alpha)}{\mathcal{U}(\alpha)}\mathcal{Q}_1\left(t_m, \mathcal{S}_{HB}(t_m)\right) \\
&\quad + \frac{\alpha}{\mathcal{U}(\alpha)\Gamma(\alpha)}\sum_{k=0}^{m}\int_0^{t_{k+1}}(t_{m+1}-\zeta)^{\alpha-1}\mathcal{Q}_1\left(\zeta, \mathcal{S}_{HB}(\zeta)\right)d\zeta, \\
\mathcal{I}_{MAL}(t_{m+1}) - \mathcal{I}_{MAL}(0) &= \frac{(1-\alpha)}{\mathcal{U}(\alpha)}\mathcal{Q}_2\left(t_m, \mathcal{I}_{MAL}(t_m)\right) \\
&\quad + \frac{\alpha}{\mathcal{U}(\alpha)\Gamma(\alpha)}\sum_{k=0}^{m}\int_0^{t_{k+1}}(t_{m+1}-\zeta)^{\alpha-1}\mathcal{Q}_2\left(\zeta, \mathcal{I}_{MAL}(\zeta)\right)d\zeta, \\
\mathcal{R}_{MAL}(t_{m+1}) - \mathcal{R}_{MAL}(0) &= \frac{(1-\alpha)}{\mathcal{U}(\alpha)}\mathcal{Q}_3\left(t_m, \mathcal{R}_{MAL}(t_m)\right) \\
&\quad + \frac{\alpha}{\mathcal{U}(\alpha)\Gamma(\alpha)}\sum_{k=0}^{m}\int_0^{t_{k+1}}(t_{m+1}-\zeta)^{\alpha-1}\mathcal{Q}_3\left(\zeta, \mathcal{R}_{MAL}(\zeta)\right)d\zeta, \\
\mathcal{I}_{CHO}(t_{m+1}) - \mathcal{I}_{CHO}(0) &= \frac{(1-\alpha)}{\mathcal{U}(\alpha)}\mathcal{Q}_4\left(t_m, \mathcal{I}_{CHO}(t_m)\right) \\
&\quad + \frac{\alpha}{\mathcal{U}(\alpha)\Gamma(\alpha)}\sum_{k=0}^{m}\int_0^{t_{k+1}}(t_{m+1}-\zeta)^{\alpha-1}\mathcal{Q}_4\left(\zeta, \mathcal{I}_{CHO}(\zeta)\right)d\zeta, \\
\mathcal{R}_{CHO}(t_{m+1}) - \mathcal{R}_{CHO}(0) &= \frac{(1-\alpha)}{\mathcal{U}(\alpha)}\mathcal{Q}_5\left(t_m, \mathcal{R}_{CHO}(t_m)\right) \\
&\quad + \frac{\alpha}{\mathcal{U}(\alpha)\Gamma(\alpha)}\sum_{k=0}^{m}\int_0^{t_{k+1}}(V-\zeta)^{\alpha-1}\mathcal{Q}_5\left(\zeta, \mathcal{R}_{CHO}(\zeta)\right)d\zeta, \\
\mathcal{I}_{MAC}(t_{m+1}) - \mathcal{I}_{MAC}(0) &= \frac{(1-\alpha)}{\mathcal{U}(\alpha)}\mathcal{Q}_6\left(t_m, \mathcal{I}_{MAC}(t_m)\right) \\
&\quad + \frac{\alpha}{\mathcal{U}(\alpha)\Gamma(\alpha)}\sum_{k=0}^{m}\int_0^{t_{k+1}}(t_{m+1}-\zeta)^{\alpha-1}\mathcal{Q}_6\left(\zeta, \mathcal{I}_{MAC}(\zeta)\right)d\zeta, \\
\mathcal{R}_{MAC}(t_{m+1}) - \mathcal{R}_{MAC}(0) &= \frac{(1-\alpha)}{\mathcal{U}(\alpha)}\mathcal{Q}_7\left(t_m, \mathcal{R}_{MAC}(t_m)\right) \\
&\quad + \frac{\alpha}{\mathcal{U}(\alpha)\Gamma(\alpha)}\sum_{k=0}^{m}\int_0^{t_{k+1}}(t_{m+1}-\zeta)^{\alpha-1}\mathcal{Q}_7\left(\zeta, \mathcal{R}_{MAC}(\zeta)\right)d\zeta, \\
\mathcal{B}_{CHO}(t_{m+1}) - \mathcal{B}_{CHO}(0) &= \frac{(1-\alpha)}{\mathcal{U}(\alpha)}\mathcal{Q}_8\left(t_m, \mathcal{B}_{CHO}(t_m)\right) \\
&\quad + \frac{\alpha}{\mathcal{U}(\alpha)\Gamma(\alpha)}\sum_{k=0}^{m}\int_0^{t_{k+1}}(t_{m+1}-\zeta)^{\alpha-1}\mathcal{Q}_8\left(\zeta, \mathcal{B}_{CHO}(\zeta)\right)d\zeta, \\
\mathcal{S}_{VEC}(t_{m+1}) - \mathcal{S}_{VEC}(0) &= \frac{(1-\alpha)}{\mathcal{U}(\alpha)}\mathcal{Q}_9\left(t_m, \mathcal{S}_{VEC}(t_m)\right) \\
&\quad + \frac{\alpha}{\mathcal{U}(\alpha)\Gamma(\alpha)}\sum_{k=0}^{m}\int_0^{t_{k+1}}(t_{m+1}-\zeta)^{\alpha-1}\mathcal{Q}_9\left(\zeta, \mathcal{S}_{VEC}(\zeta)\right)d\zeta, \\
\mathcal{I}_{VEC}(t_{m+1}) - \mathcal{I}_{VEC}(0) &= \frac{(1-\alpha)}{\mathcal{U}(\alpha)}\mathcal{Q}_{10}\left(t_m, \mathcal{I}_{VEC}(t_m)\right) \\
&\quad + \frac{\alpha}{\mathcal{U}(\alpha)\Gamma(\alpha)}\sum_{k=0}^{m}\int_0^{t_{k+1}}(t_{m+1}-\zeta)^{\alpha-1}\mathcal{Q}_{10}\left(\zeta, \mathcal{I}_{VEC}(\zeta)\right)d\zeta.
\end{aligned}$$

By two–point Lagrange interpolation polynomial, we approximate $\mathcal{Q}_1(\zeta, \mathcal{S}_{HB}(\zeta))$, $\mathcal{Q}_2(\zeta, \mathcal{I}_{MAL}(\zeta))$, $\mathcal{Q}_3(\zeta, \mathcal{R}_{MAL}(\zeta))$, $\mathcal{Q}_4(\zeta, \mathcal{I}_{CHO}(\zeta))$, $\mathcal{Q}_5(\zeta, \mathcal{R}_{CHO}(\zeta))$, $\mathcal{Q}_6(\zeta, \mathcal{I}_{MAC}(\zeta))$, $\mathcal{Q}_7(\zeta, \mathcal{R}_{MAC}(\zeta))$, $\mathcal{Q}_8(\zeta, \mathcal{B}_{CHO}(\zeta))$, $\mathcal{Q}_9(\zeta, \mathcal{S}_{VEC}(\zeta))$, $\mathcal{Q}_{10}(\zeta, \mathcal{I}_{VEC}(\zeta))$ in (18) on the interval $[t_k, t_{k+1}]$ and get

$$
\begin{aligned}
\mathcal{Q}_1(\zeta, \mathcal{S}_{HB}(\zeta)) &\approx \frac{\mathcal{Q}_1(t_k, \mathcal{S}_{HB}(t_k))}{h}(t - t_{k-1}) + \frac{\mathcal{Q}_1(t_{k-1}, \mathcal{S}_{HB}(t_{k-1}))}{h}(t - t_k),\\
\mathcal{Q}_2(\zeta, \mathcal{I}_{MAL}(\zeta)) &\approx \frac{\mathcal{Q}_2(t_k, \mathcal{I}_{MAL}(t_k))}{h}(t - t_{k-1}) + \frac{\mathcal{Q}_2(t_{k-1}, \mathcal{I}_{MAL}(t_{k-1}))}{h}(t - t_k),\\
\mathcal{Q}_3(\zeta, \mathcal{R}_{MAL}(\zeta)) &\approx \frac{\mathcal{Q}_3(t_k, \mathcal{R}_{MAL}(t_k))}{h}(t - t_{k-1}) + \frac{\mathcal{Q}_3(t_{k-1}, \mathcal{R}_{MAL}(t_{k-1}))}{h}(t - t_k),\\
\mathcal{Q}_4(\zeta, \mathcal{I}_{CHO}(\zeta)) &\approx \frac{\mathcal{Q}_4(t_k, \mathcal{I}_{CHO}(t_k))}{h}(t - t_{k-1}) + \frac{\mathcal{Q}_4(t_{k-1}, \mathcal{I}_{CHO}(t_{k-1}))}{h}(t - t_k),\\
\mathcal{Q}_5(\zeta, \mathcal{R}_{CHO}(\zeta)) &\approx \frac{\mathcal{Q}_5(t_k, \mathcal{R}_{CHO}(t_k))}{h}(t - t_{k-1}) + \frac{\mathcal{Q}_5(t_{k-1}, \mathcal{R}_{CHO}(t_{k-1}))}{h}(t - t_k),\\
\mathcal{Q}_6(\zeta, \mathcal{I}_{MAC}(\zeta)) &\approx \frac{\mathcal{Q}_6(t_k, \mathcal{I}_{MAC}(t_k))}{h}(t - t_{k-1}) + \frac{\mathcal{Q}_6(t_{k-1}, \mathcal{I}_{MAC}(t_{k-1}))}{h}(t - t_k),\\
\mathcal{Q}_7(\zeta, \mathcal{R}_{MAC}(\zeta)) &\approx \frac{\mathcal{Q}_7(t_k, \mathcal{R}_{MAC}(t_k))}{h}(t - t_{k-1}) + \frac{\mathcal{Q}_7(t_{k-1}, \mathcal{R}_{MAC}(t_{k-1}))}{h}(t - t_k),\\
\mathcal{Q}_8(\zeta, \mathcal{B}_{CHO}(\zeta)) &\approx \frac{\mathcal{Q}_8(t_k, \mathcal{B}_{CHO}(t_k))}{h}(t - t_{k-1}) + \frac{\mathcal{Q}_8(t_{k-1}, \mathcal{B}_{CHO}(t_{k-1}))}{h}(t - t_k),\\
\mathcal{Q}_9(\zeta, \mathcal{S}_{VEC}(\zeta)) &\approx \frac{\mathcal{Q}_9(t_k, \mathcal{S}_{VEC}(t_k))}{h}(t - t_{k-1}) + \frac{\mathcal{Q}_9(t_{k-1}, \mathcal{S}_{VEC}(t_{k-1}))}{h}(t - t_k),\\
\mathcal{Q}_{10}(\zeta, \mathcal{I}_{VEC}(\zeta)) &\approx \frac{\mathcal{Q}_{10}(t_k, \mathcal{I}_{VEC}(t_k))}{h}(t - t_{k-1}) + \frac{\mathcal{Q}_{10}(t_{k-1}, \mathcal{I}_{VEC}(t_{k-1}))}{h}(t - t_k),
\end{aligned}
\tag{18}
$$

so that system (18) becomes

$$
\begin{aligned}
\mathcal{S}_{HB}(t_{m+1}) - \mathcal{S}_{HB}(0) &= \frac{(1-\alpha)}{\mathcal{U}(\alpha)}\mathcal{Q}_1(t_m, \mathcal{S}_{HB}(t_m))\\
&\quad + \frac{\alpha}{\mathcal{U}(\alpha)\Gamma(\alpha)}\sum_{k=0}^{m}\left(\frac{\mathcal{Q}_1(t_k, \mathcal{S}_{HB}(t_k))}{h}\mathcal{P}_{k-1,\alpha} + \frac{\mathcal{Q}_1(t_{k-1}, \mathcal{S}_{HB}(t_{k-1}))}{h}\mathcal{P}_{k,\alpha}\right),\\
\mathcal{I}_{MAL}(t_{m+1}) - \mathcal{I}_{MAL}(0) &= \frac{(1-\alpha)}{\mathcal{U}(\alpha)}\mathcal{Q}_2(t_m, \mathcal{I}_{MAL}(t_m))\\
&\quad + \frac{\alpha}{\mathcal{U}(\alpha)\Gamma(\alpha)}\sum_{k=0}^{m}\left(\frac{\mathcal{Q}_2(t_k, \mathcal{I}_{MAL}(t_k))}{h}\mathcal{P}_{k-1,\alpha} + \frac{\mathcal{Q}_2(t_{k-1}, \mathcal{I}_{MAL}(t_{k-1}))}{h}\mathcal{P}_{k,\alpha}\right),\\
\mathcal{R}_{MAL}(t_{m+1}) - \mathcal{R}_{MAL}(0) &= \frac{(1-\alpha)}{\mathcal{U}(\alpha)}\mathcal{Q}_3(t_m, \mathcal{R}_{MAL}(t_m))\\
&\quad + \frac{\alpha}{\mathcal{U}(\alpha)\Gamma(\alpha)}\sum_{k=0}^{m}\left(\frac{\mathcal{Q}_3(t_k, \mathcal{R}_{MAL}(t_k))}{h}\mathcal{P}_{k-1,\alpha} + \frac{\mathcal{Q}_3(t_{k-1}, \mathcal{R}_{MAL}(t_{k-1}))}{h}\mathcal{P}_{k,\alpha}\right),\\
\mathcal{I}_{CHO}(t_{m+1}) - \mathcal{I}_{CHO}(0) &= \frac{(1-\alpha)}{\mathcal{U}(\alpha)}\mathcal{Q}_4(t_m, \mathcal{I}_{CHO}(t_m))\\
&\quad + \frac{\alpha}{\mathcal{U}(\alpha)\Gamma(\alpha)}\sum_{k=0}^{m}\left(\frac{\mathcal{Q}_4(t_k, \mathcal{I}_{CHO}(t_k))}{h}\mathcal{P}_{k-1,\alpha} + \frac{\mathcal{Q}_4(t_{k-1}, \mathcal{I}_{CHO}(t_{k-1}))}{h}\mathcal{P}_{k,\alpha}\right),
\end{aligned}
$$

$$
\begin{aligned}
\mathcal{R}_{CHO}(t_{m+1}) - \mathcal{R}_{CHO}(0) &= \frac{(1-\alpha)}{\mathcal{U}(\alpha)}\mathcal{Q}_5\left(t_m, \mathcal{R}_{CHO}(t_m)\right) \\
&\quad + \frac{\alpha}{\mathcal{U}(\alpha)\Gamma(\alpha)}\sum_{k=0}^{m}\left(\frac{\mathcal{Q}_5\left(t_k, \mathcal{R}_{CHO}(t_k)\right)}{h}\mathcal{P}_{k-1,\alpha} + \frac{\mathcal{Q}_5\left(t_{k-1}, \mathcal{R}_{CHO}(t_{k-1})\right)}{h}\mathcal{P}_{k,\alpha}\right), \\
\mathcal{I}_{MAC}(t_{m+1}) - \mathcal{I}_{MAC}(0) &= \frac{(1-\alpha)}{\mathcal{U}(\alpha)}\mathcal{Q}_6\left(t_m, \mathcal{I}_{MAC}(t_m)\right) \\
&\quad + \frac{\alpha}{\mathcal{U}(\alpha)\Gamma(\alpha)}\sum_{k=0}^{m}\left(\frac{\mathcal{Q}_6\left(t_k, \mathcal{I}_{MAC}(t_k)\right)}{h}\mathcal{P}_{k-1,\alpha} + \frac{\mathcal{Q}_6\left(t_{k-1}, \mathcal{I}_{MAC}(t_{k-1})\right)}{h}\mathcal{P}_{k,\alpha}\right), \\
\mathcal{R}_{MAC}(t_{m+1}) - \mathcal{R}_{MAC}(0) &= \frac{(1-\alpha)}{\mathcal{U}(\alpha)}\mathcal{Q}_7\left(t_m, \mathcal{R}_{MAC}(t_m)\right) \\
&\quad + \frac{\alpha}{\mathcal{U}(\alpha)\Gamma(\alpha)}\sum_{k=0}^{m}\left(\frac{\mathcal{Q}_1\left(t_k, \mathcal{R}_{MAC}(t_k)\right)}{h}\mathcal{P}_{k-1,\alpha} + \frac{\mathcal{Q}_7\left(t_{k-1}, \mathcal{R}_{MAC}(t_{k-1})\right)}{h}\mathcal{P}_{k,\alpha}\right), \\
\mathcal{B}_{CHO}(t_{m+1}) - \mathcal{B}_{CHO}(0) &= \frac{(1-\alpha)}{\mathcal{U}(\alpha)}\mathcal{Q}_8\left(t_m, \mathcal{B}_{CHO}(t_m)\right) \\
&\quad + \frac{\alpha}{\mathcal{U}(\alpha)\Gamma(\alpha)}\sum_{k=0}^{m}\left(\frac{\mathcal{Q}_8\left(t_k, \mathcal{B}_{CHO}(t_k)\right)}{h}\mathcal{P}_{k-1,\alpha} + \frac{\mathcal{Q}_8\left(t_{k-1}, \mathcal{B}_{CHO}(t_{k-1})\right)}{h}\mathcal{P}_{k,\alpha}\right), \\
\mathcal{S}_{VEC}(t_{m+1}) - \mathcal{S}_{VEC}(0) &= \frac{(1-\alpha)}{\mathcal{U}(\alpha)}\mathcal{Q}_9\left(t_m, \mathcal{S}_{VEC}(t_m)\right) \\
&\quad + \frac{\alpha}{\mathcal{U}(\alpha)\Gamma(\alpha)}\sum_{k=0}^{m}\left(\frac{\mathcal{Q}_9\left(t_k, \mathcal{S}_{VEC}(t_k)\right)}{h}\mathcal{P}_{k-1,\alpha} + \frac{\mathcal{Q}_9\left(t_{k-1}, \mathcal{S}_{VEC}(t_{k-1})\right)}{h}\mathcal{P}_{k,\alpha}\right), \\
\mathcal{I}_{VEC}(t_{m+1}) - \mathcal{I}_{VEC}(0) &= \frac{(1-\alpha)}{\mathcal{U}(\alpha)}\mathcal{Q}_{10}\left(t_m, \mathcal{I}_{VEC}(t_m)\right) \\
&\quad + \frac{\alpha}{\mathcal{U}(\alpha)\Gamma(\alpha)}\sum_{k=0}^{m}\left(\frac{\mathcal{Q}_{10}\left(t_k, \mathcal{I}_{VEC}(t_k)\right)}{h}\mathcal{P}_{k-1,\alpha} + \frac{\mathcal{Q}_{10}\left(t_{k-1}, \mathcal{I}_{VEC}(t_{k-1})\right)}{h}\mathcal{P}_{k,\alpha}\right),
\end{aligned}
\tag{19}
$$

where and using $t_k = kh$, we obtain

$$
\begin{aligned}
\mathcal{P}_{k-1,\alpha} &= \int_{t_k}^{t_{k+1}} (t - t_{k-1})(t_{m+1} - t)^{\alpha-1} dt \\
&= \frac{h^{\alpha+1}}{\alpha(\alpha+1)}\Big[(m+1-k)^{\alpha}(m-k+2+\alpha) - (m-k)^{\alpha}(m-k+2+2\alpha)\Big], \\
\mathcal{P}_{k,\alpha} &= \int_{t_k}^{t_{k+1}} (t - t_k)(t_{m+1} - t)^{\alpha-1} dt = \frac{h^{\alpha+1}}{\alpha(\alpha+1)}\Big[(m+1-k)^{\alpha+1} - (m-k)^{\alpha}(m-k+1+\alpha)\Big].
\end{aligned}
\tag{20}
$$

Substituting (20) into (19) gives

$$
\begin{aligned}
\mathcal{S}_{HB}(t_{m+1}) &= \mathcal{S}_{HB}(0) + \frac{(1-\alpha)}{\mathcal{U}(\alpha)}\mathcal{Q}_1\left(t_m, \mathcal{S}_{HB}(t_m)\right) + \frac{\alpha h^{\alpha}}{\mathcal{U}(\alpha)\Gamma(\alpha+2)} \\
&\quad \times \sum_{k=0}^{m}\Bigg[\mathcal{Q}_1\left(t_k, \mathcal{S}_{HB}(t_k)\right)\Big((m+1-k)^{\alpha}(m-k+2+\alpha) - (m-k)^{\alpha}(m-k+2+2\alpha)\Big) \\
&\quad + \mathcal{Q}_1\left(t_{k-1}, \mathcal{S}_{HB}(t_{k-1})\right)\Big((m+1-k)^{\alpha+1} - (m-k)^{\alpha}(m-k+1+\alpha)\Big)\Bigg].
\end{aligned}
$$

$$\mathcal{I}_{MAL}(t_{m+1}) = \mathcal{I}_{MAL}(0) + \frac{(1-\alpha)}{\mathcal{U}(\alpha)}\mathcal{Q}_2\left(t_m, \mathcal{I}_{MAL}(t_m)\right) + \frac{\alpha h^\alpha}{\mathcal{U}(\alpha)\Gamma(\alpha+2)}$$
$$\times \sum_{k=0}^{m}\left[\mathcal{Q}_2\left(t_k, \mathcal{I}_{MAL}(t_k)\right)\left((m+1-k)^\alpha(m-k+2+\alpha) - (m-k)^\alpha(m-k+2+2\alpha)\right)\right.$$
$$\left. + \mathcal{Q}_2\left(t_{k-1}, \mathcal{I}_{MAL}(t_{k-1})\right)\left((m+1-k)^{\alpha+1} - (m-k)^\alpha(m-k+1+\alpha)\right)\right].$$

$$\mathcal{R}_{MAL}(t_{m+1}) = \mathcal{R}_{MAL}(0) + \frac{(1-\alpha)}{\mathcal{U}(\alpha)}\mathcal{Q}_3\left(t_m, \mathcal{R}_{MAL}(t_m)\right) + \frac{\alpha h^\alpha}{\mathcal{U}(\alpha)\Gamma(\alpha+2)}$$
$$\times \sum_{k=0}^{m}\left[\mathcal{Q}_3\left(t_k, \mathcal{R}_{MAL}(t_k)\right)\left((m+1-k)^\alpha(m-k+2+\alpha) - (m-k)^\alpha(m-k+2+2\alpha)\right)\right.$$
$$\left. + \mathcal{Q}_3\left(t_{k-1}, \mathcal{R}_{MAL}(t_{k-1})\right)\left((m+1-k)^{\alpha+1} - (m-k)^\alpha(m-k+1+\alpha)\right)\right].$$

$$\mathcal{I}_{CHO}(t_{m+1}) = \mathcal{I}_{CHO}(0) + \frac{(1-\alpha)}{\mathcal{U}(\alpha)}\mathcal{Q}_4\left(t_m, \mathcal{I}_{CHO}(t_m)\right) + \frac{\alpha h^\alpha}{\mathcal{U}(\alpha)\Gamma(\alpha+2)}$$
$$\times \sum_{k=0}^{m}\left[\mathcal{Q}_4\left(t_k, \mathcal{I}_{CHO}(t_k)\right)\left((m+1-k)^\alpha(m-k+2+\alpha) - (m-k)^\alpha(m-k+2+2\alpha)\right)\right.$$
$$\left. + \mathcal{Q}_4\left(t_{k-1}, \mathcal{I}_{CHO}(t_{k-1})\right)\left((m+1-k)^{\alpha+1} - (m-k)^\alpha(m-k+1+\alpha)\right)\right].$$

$$\mathcal{R}_{CHO}(t_{m+1}) = \mathcal{R}_{CHO}(0) + \frac{(1-\alpha)}{\mathcal{U}(\alpha)}\mathcal{Q}_5\left(t_m, \mathcal{R}_{CHO}(t_m)\right) + \frac{\alpha h^\alpha}{\mathcal{U}(\alpha)\Gamma(\alpha+2)}$$
$$\times \sum_{k=0}^{m}\left[\mathcal{Q}_5\left(t_k, \mathcal{R}_{CHO}(t_k)\right)\left((m+1-k)^\alpha(m-k+2+\alpha) - (m-k)^\alpha(m-k+2+2\alpha)\right)\right.$$
$$\left. + \mathcal{Q}_5\left(t_{k-1}, \mathcal{R}_{CHO}(t_{k-1})\right)\left((m+1-k)^{\alpha+1} - (m-k)^\alpha(m-k+1+\alpha)\right)\right].$$

$$\mathcal{I}_{MAC}(t_{m+1}) = \mathcal{I}_{MAC}(0) + \frac{(1-\alpha)}{\mathcal{U}(\alpha)}\mathcal{Q}_6\left(t_m, \mathcal{I}_{MAC}(t_m)\right) + \frac{\alpha h^\alpha}{\mathcal{U}(\alpha)\Gamma(\alpha+2)}$$
$$\times \sum_{k=0}^{m}\left[\mathcal{Q}_6\left(t_k, \mathcal{I}_{MAC}(t_k)\right)\left((m+1-k)^\alpha(m-k+2+\alpha) - (m-k)^\alpha(m-k+2+2\alpha)\right)\right.$$
$$\left. + \mathcal{Q}_6\left(t_{k-1}, \mathcal{I}_{MAC}(t_{k-1})\right)\left((m+1-k)^{\alpha+1} - (m-k)^\alpha(m-k+1+\alpha)\right)\right].$$

$$\mathcal{R}_{MAC}(t_{m+1}) = \mathcal{R}_{MAC}(0) + \frac{(1-\alpha)}{\mathcal{U}(\alpha)}\mathcal{Q}_7\left(t_m, \mathcal{R}_{MAC}(t_m)\right) + \frac{\alpha h^\alpha}{\mathcal{U}(\alpha)\Gamma(\alpha+2)}$$
$$\times \sum_{k=0}^{m}\left[\mathcal{Q}_7\left(t_k, \mathcal{R}_{MAC}(t_k)\right)\left((m+1-k)^\alpha(m-k+2+\alpha) - (m-k)^\alpha(m-k+2+2\alpha)\right)\right.$$
$$\left. + \mathcal{Q}_7\left(t_{k-1}, \mathcal{R}_{MAC}(t_{k-1})\right)\left((m+1-k)^{\alpha+1} - (m-k)^\alpha(m-k+1+\alpha)\right)\right].$$

$$\mathcal{B}_{CHO}(t_{m+1}) = \mathcal{B}_{CHO}(0) + \frac{(1-\alpha)}{\mathcal{U}(\alpha)}\mathcal{Q}_8\left(t_m, \mathcal{B}_{CHO}(t_m)\right) + \frac{\alpha h^\alpha}{\mathcal{U}(\alpha)\Gamma(\alpha+2)}$$
$$\times \sum_{k=0}^{m}\left[\mathcal{Q}_8\left(t_k, \mathcal{B}_{CHO}(t_k)\right)\left((m+1-k)^\alpha(m-k+2+\alpha) - (m-k)^\alpha(m-k+2+2\alpha)\right)\right.$$
$$\left. + \mathcal{Q}_8\left(t_{k-1}, \mathcal{B}_{CHO}(t_{k-1})\right)\left((m+1-k)^{\alpha+1} - (m-k)^\alpha(m-k+1+\alpha)\right)\right].$$

$$\mathcal{S}_{VEC}(t_{m+1}) = \mathcal{S}_{VEC}(0) + \frac{(1-\alpha)}{\mathcal{U}(\alpha)}\mathcal{Q}_9\left(t_m, \mathcal{S}_{VEC}(t_m)\right) + \frac{\alpha h^\alpha}{\mathcal{U}(\alpha)\Gamma(\alpha+2)}$$
$$\times \sum_{k=0}^{m}\left[\mathcal{Q}_9\left(t_k, \mathcal{S}_{VEC}(t_k)\right)\left((m+1-k)^\alpha(m-k+2+\alpha) - (m-k)^\alpha(m-k+2+2\alpha)\right)\right.$$
$$\left. + \mathcal{Q}_9\left(t_{k-1}, \mathcal{S}_{VEC}(t_{k-1})\right)\left((m+1-k)^{\alpha+1} - (m-k)^\alpha(m-k+1+\alpha)\right)\right].$$

$$\mathcal{I}_{VEC}(t_{m+1}) = \mathcal{I}_{VEC}(0) + \frac{(1-\alpha)}{\mathcal{U}(\alpha)}\mathcal{Q}_{10}\left(t_m, \mathcal{I}_{VEC}(t_m)\right) + \frac{\alpha h^\alpha}{\mathcal{U}(\alpha)\Gamma(\alpha+2)}$$
$$\times \sum_{k=0}^{m}\left[\mathcal{Q}_{10}\left(t_k, \mathcal{I}_{VEC}(t_k)\right)\left((m+1-k)^\alpha(m-k+2+\alpha) - (m-k)^\alpha(m-k+2+2\alpha)\right)\right.$$
$$\left. + \mathcal{Q}_{10}\left(t_{k-1}, \mathcal{I}_{VEC}(t_{k-1})\right)\left((m+1-k)^{\alpha+1} - (m-k)^\alpha(m-k+1+\alpha)\right)\right].$$

6 Results and discussion

We present the results of the subject matter with the aid of the above numerical scheme for the numerical solution of the proposed malaria and cholera system. For this purpose, we will adopt the data in Table 1 and support it with the following initial conditions for each compartment $\mathcal{S}_{HB}(0) = 10000$, $\mathcal{I}_{MAL}(0) = 2000$, $\mathcal{R}_{MAL}(0) = 300$, $\mathcal{I}_{CHO}(0) = 400$, $\mathcal{R}_{CHO}(0) = 300$, $\mathcal{I}_{MAC}(0) = 200$, $\mathcal{R}_{MAC}(0) = 100$, $\mathcal{B}_{CHO}(0) = 2000$, $\mathcal{S}_{VEC}(0) = 2000$, $\mathcal{I}_{VEC}(0) = 2000$ and the fractional orders 0.50, 0.60, 0.70, 0.80, 0.90 to plot all the ten classes in malaria and cholera dynamic system. The dynamic behavior of all the compartments is shown in Figs. 1–10. The susceptible populations to these diseases represented in Fig. 1 increase mildly until infected by the diseases and transfer to other compartments within the system (1).

The mild increase of susceptible populations without interaction with the diseases occurs as the fractional order tends to one. Fig. 2 shows the infection with malaria caused a transitional increase with time in the population, then decreases and stabilizes after precautionary measures were applied. A considerable response within the infected class as individuals respond to treatment and necessary malaria control measures can be seen in Fig. 3.

As individuals recover from malaria and are infected by cholera, it can be seen from Fig. 4 that a sharp decrease occurs as the fractional order increases. As individuals recover from cholera after being infected through the necessary, an increase is recorded as depicted in Fig. 5. It can be seen in Figs. 6 and 8 that there is a decrease within the population as co-infection of malaria and cholera occurs.

The presence of the bacteria compartment facilitates this decrease as fractional order decreases and converges to a certain point as time increases. The increase is seen in Fig. 7. The numerous numbers of susceptible vectors show a correlation with the fractional order in Fig. 9. An increase in the fractional order increases the number of susceptible vectors. After a stable population of about a hundred individuals for the first three days, a decrease in the population of infectious vectors is noticed when the fractional order increases as shown in Fig. 10. This explains the level of infection in the vector population. Also, infection with cholera reduces more population of individuals compared to infection with malaria within the same time interval.

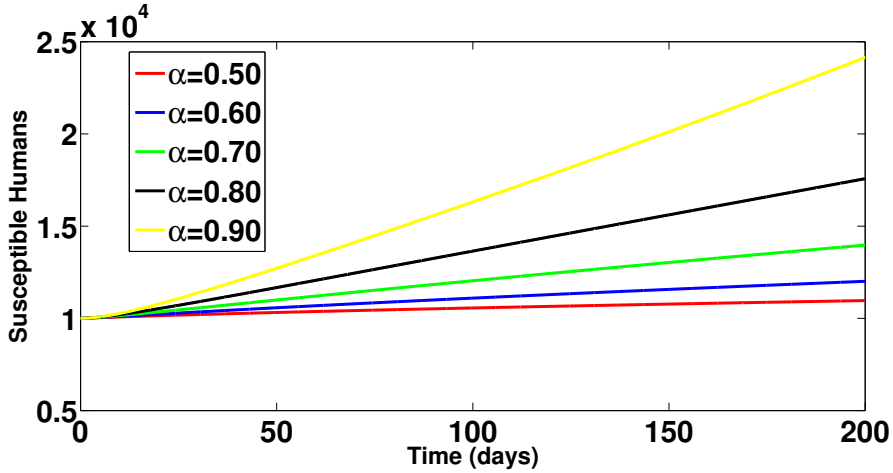

Figure 1. Simulations of the total number of $\mathcal{S}_{HB}(t)$ at different values of α on the interval of $(0, 1)$ with the stated initial data.

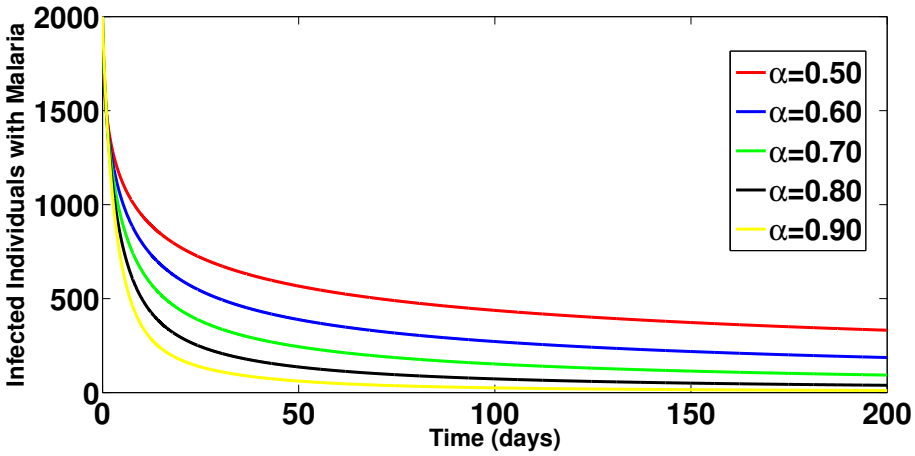

Figure 2. Simulations of the total number of $\mathcal{I}_{MAL}(t)$ at different values of α on the interval of $(0, 1)$ with the stated initial data.

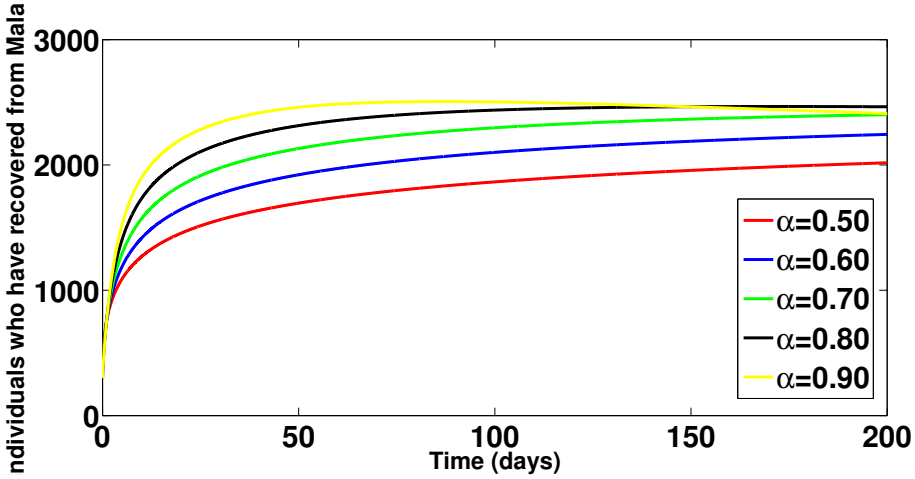

Figure 3. Simulations of the total number of $\mathcal{R}_{MAL}(t)$ at different values of α on the interval of $(0, 1)$ with the stated initial data.

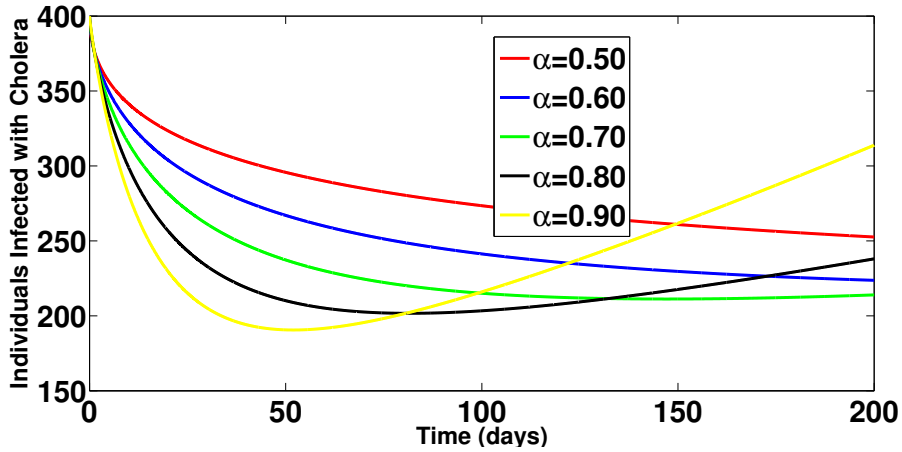

Figure 4. Simulations of the total number of $\mathcal{I}_{CHO}(t)$ at different values of α on the interval of $(0, 1)$ with the stated initial data.

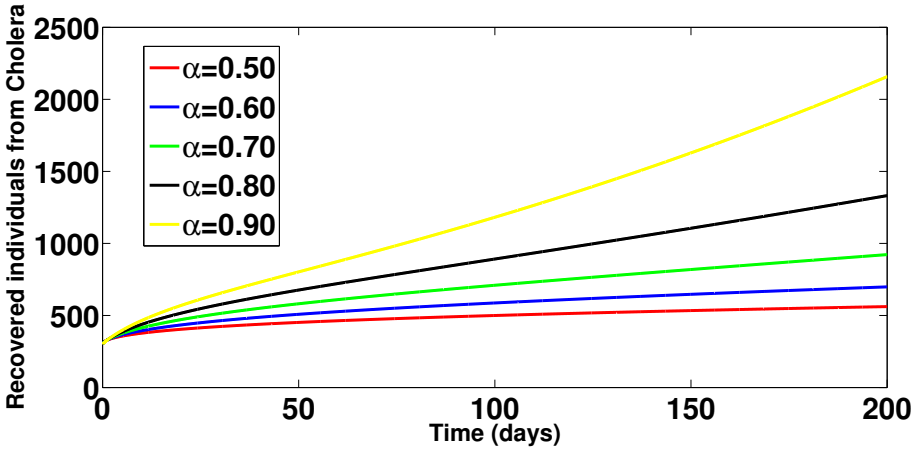

Figure 5. Simulations of the total number of $\mathcal{R}_{CHO}(t)$ at different values of α on the interval of $(0, 1)$ with the stated initial data.

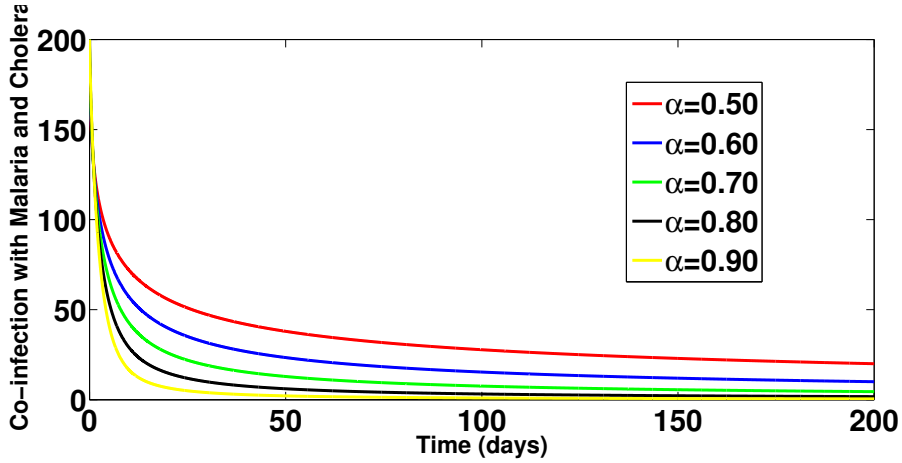

Figure 6. Simulations of the total number of $\mathcal{I}_{MAC}(t)$ at different values of α on the interval of $(0, 1)$ with the stated initial data.

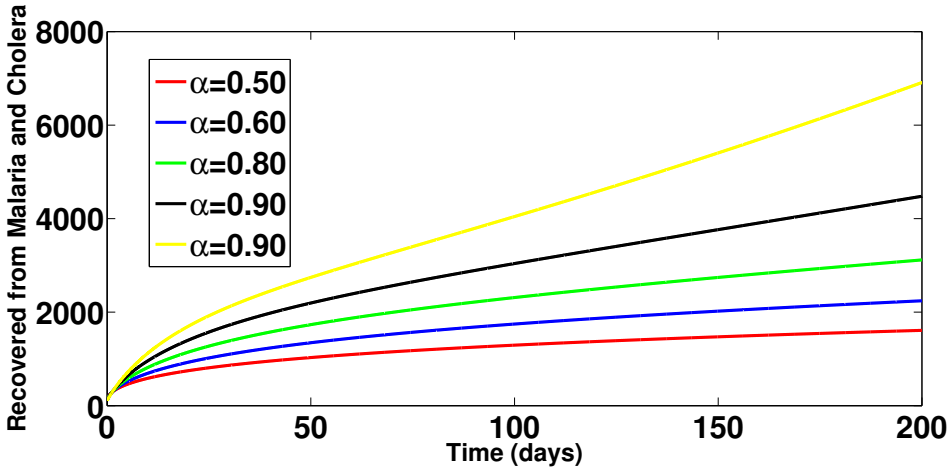

Figure 7. Simulations of the total number of $\mathcal{R}_{MAC}(t)$ at different values of α on the interval of $(0,1)$ with the stated initial data.

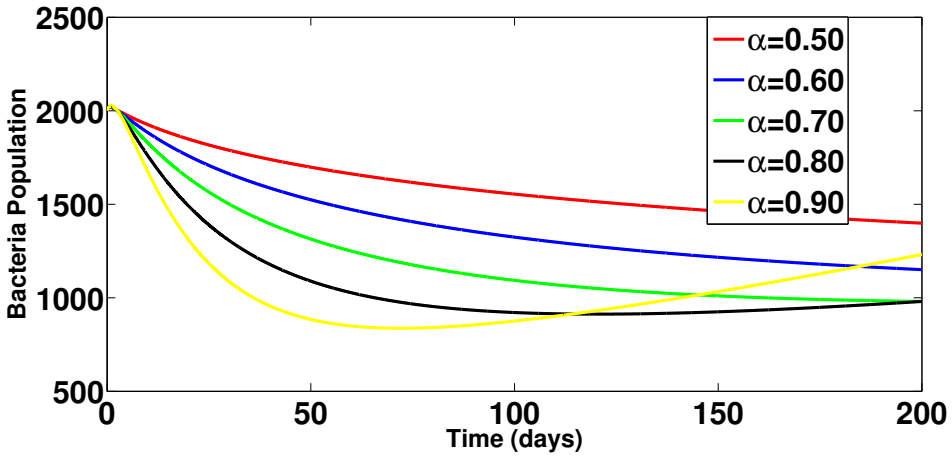

Figure 8. Simulations of the total number of $\mathcal{B}_{CHO}(t)$ at different values of α on the interval of $(0,1)$ with the stated initial data.

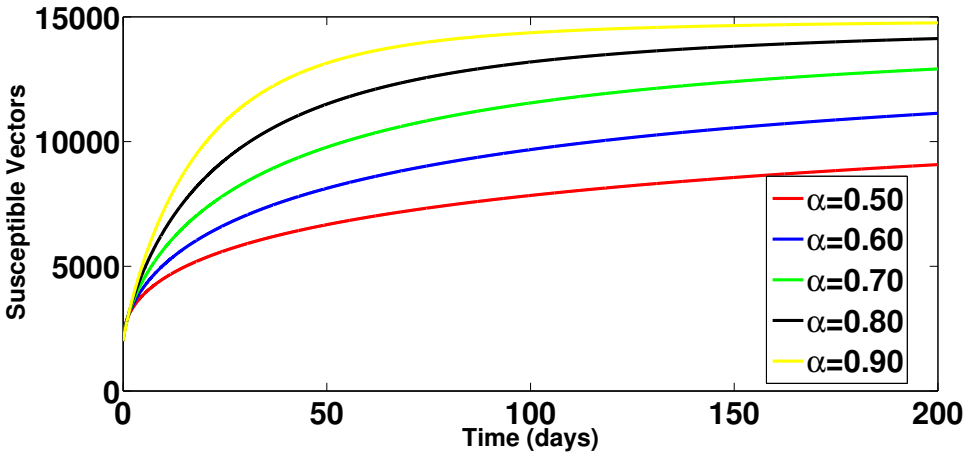

Figure 9. Simulations of the total number of $\mathcal{S}_{VEC}(t)$ at different values of α on the interval of $(0,1)$ with the stated initial data.

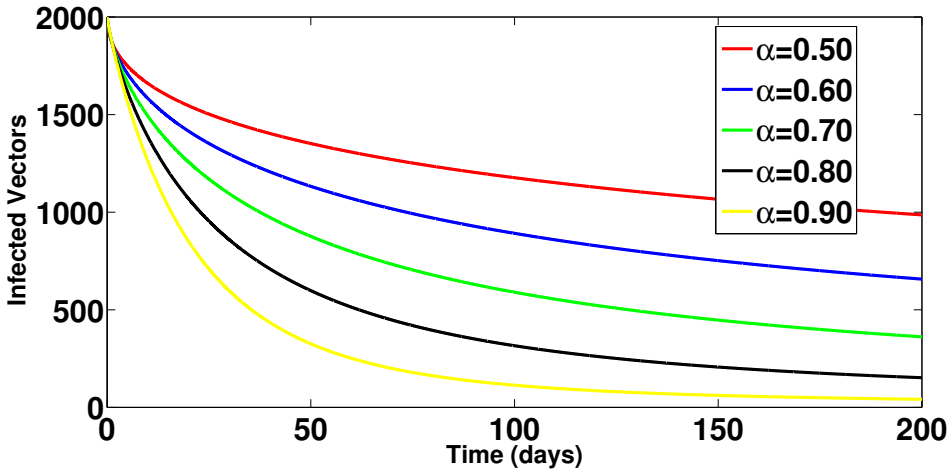

Figure 10. Simulations of the total number of $\mathcal{I}_{VEC}(t)$ at different values of α on the interval of $(0, 1)$ with the stated initial data.

7 Conclusion

In this paper, we investigated the fractional co-infection model of malaria and cholera in detail. We also established the existence and uniqueness of the solution using Banach and Schauder's fixed point theorems. The positivity and boundedness of the fractional system solution are stated and proved by using Mittag–Leffler function. The basic reproduction number R_0 is computed using the next-generation matrix method and it reveals that malaria–cholera model is locally asymptotically stable when $R_0 < 1$. Several simulations on the model were performed numerically and we obtained various graphical results that align with the theoretical result obtained. Further results revealed that infection with cholera reduces more population of individuals compared to infection with malaria during the same time interval. For the future research interests of this work, we recommend consideration of control measures and other fractional derivatives for this purpose.

Declarations

Consent for publication

Not applicable.

Conflicts of interest

The authors declare that they have no conflict of interest.

Funding

Not applicable.

Author's contributions

L.L.I.: Conceptualization, Software, Formal Analysis, Writing - Original draft, U.K.N.: Methodology, Supervision, Writing - Review and Editing, A.O.A.: Formal Analysis, Validation, A.B.P.: Formal Analysis, Validation, K.U.E.: Visualization, Data Curation, All authors discussed the results and contributed to the final manuscript.

Acknowledgements

Not applicable.

References

[1] Birhanie, M., Tessema, B., Ferede, G., Endris, M., & Enawgaw, B. Malaria, typhoid fever, and their coinfection among febrile patients at a rural health center in Northwest Ethiopia: a cross-sectional study. *Advances in Medicine*, 531074, (2014). [CrossRef]

[2] World malaria report 2019. https://www.who.int/malaria/publications/world-malaria-report-2019/en/.(2019), Meeting Report, Access date: 25th November 2022.

[3] World Health Organization, www.who.int/news-room, Access date: 30th March 2022.

[4] Centres for Disease Control and Prevention (CDC). Cholera - Vibrio cholera infection, (2020). https://www.cdc.gov/cholera/general/index.html. Access date: 12th August 2022.

[5] Ross, S. *The Prevention of Malaria* Dutton: New York, NY, USA, (1911).

[6] Okosun, K.O. & Makinde O.D. A co-infection model of malaria and cholera diseases with optimal control. *Mathematical Biosciences*, 258, 19-32, (2014). [CrossRef]

[7] Egeonu, K.U., Omame, A., & Inyama, S.C. A co-infection model for two-strain malaria and cholera with optimal control. *International Journal of Dynamics and Control*, 9, 1612–1632, (2021). [CrossRef]

[8] Mandal, S., Sarkar, R.R., & Sinha, S. Mathematical models of malaria-a review. *Malaria Journal*, 10, 202, (2011). [CrossRef]

[9] Oke, S.I., Ojo, M.M., Adeniyi, M.O., & Matadi, M.B. Mathematical modeling of malaria disease with control strategy. *Communication in Mathematical Biology and Neuroscience*, (2020). [CrossRef]

[10] Osman, M.A.E., Adu, I.K., Simple mathematical model for malaria transmission. *Journal of Advances in Mathematics and Computer Science*, 25(6), 1-24, (2017). [CrossRef]

[11] Tilahun, G.T., Woldegerima, W.A., & Wondifraw, A. Stochastic and deterministic mathematical model of cholera disease dynamics with direct transmission. *Advances in Difference Equation*, 2020, (2020). [CrossRef]

[12] Hntsa, K.H., & Kahsay, B.N. Analysis of cholera epidemic controlling using mathematical modeling. *International Journal of Mathematics and Mathematical Sciences*, 2020, 1-13, (2020). [CrossRef]

[13] Nwajeri, U.K., Panle, A.B., Omame, A., Obi M.C., & Onyenegecha, C.P. On the fractional order model for HPV and Syphilis using non-singular kernel. *Results in Physics*, 37, 105463, (2022). [CrossRef]

[14] Omame, A., Isah, M.E., Abbas, M., Abdel-Aty, A.H, & Onyenegecha, C.P. A fractional order model for Dual Variants of COVID-19 and HIV co-infection via Atangana-Baleanu derivative. *Alexandria Engineering Journal*, 61(12), 9715-9731, (2022). [CrossRef]

[15] Nwajeri, U.K., Omame, A., & Onyenegecha, C.P. Analysis of a fractional order model for HPV and CT co-infection. *Results in Physics*, 28, 104643, (2021). [CrossRef]

[16] Ogunrinde, R.B., Nwajeri, U.K., Fadugba, S.E., Ogunrinde, R.R., & Oshinubi, K.I. Dynamic model of COVID-19 and citizens reaction using fractional derivative. *Alexandria Engineering Journal*, 60(2), 2001-2012, (2021). [CrossRef]

[17] Ahmed, I., Baba, I.A., Yusuf, A., Kumam, P., & Kumam, W. Analysis of Caputo fractional-

order model for COVID-19 with lockdown. *Advances in Difference Equations*, 394, (2020). [CrossRef]

[18] Almeida, R., Cruz, A.M.C.B., Martins, N., & Monteiro, M.T.T. An epidemiological MSEIR model described by the Caputo fractional derivative. *International Journal of Dynamics and Control*, 7, 776-784, (2019). [CrossRef]

[19] Karaji, P.T., & Nyamoradi, N. Analysis of a fractional SIR model with general incidence function. *Applied Mathematics Letters*, 108, 106499, (2020). [CrossRef]

[20] Lin, W. Global existence theory and chaos control of fractional differential equations. *Journal of Mathematical Analysis and Applications*, 332(1), 709-726, (2007). [CrossRef]

[21] Tuan, N.H., Mohammadi, H., & Rezapour, S. A mathematical model for COVID-19 transmission by using the Caputo fractional derivative. *Chaos, Solitons & Fractals*, 140, 110107, (2020). [CrossRef]

[22] Alrabaiah, H., Ur-Rahman, M., Mahariq, I., Bushnaq, S., & Arfan, M. Fractional order analysis of HBV and HCV co-infection under ABC derivative. *Fractals*, 30(01), 2240036, (2022). [CrossRef]

[23] Wei-Yun, S., Yu-Ming, C., Ur-Rahman, M., Mahariq, I., & Zeb, A. Mathematical analysis of HBV and HCV co-infection model nonsingular fractional order derivative. *Results in Physics*, 28, 104582, (2021). [CrossRef]

[24] Arafa, A.A.M., Rida, S.Z, & Khalil, M. A fractional-order model of HIV infection with drug therapy effect. *Journal of the Egyptian Mathematical Society*,22(3), 538-543, (2014). [CrossRef]

[25] Baleanu, D., Jajarmi, A., Sajjadi, S.S., & Mozyrska, D. A new fractional model and optimal control of a tumor-immune surveillance with non-singular derivative operator. *Chaos: An Interdisciplinary Journal of Nonlinear Science*, 29(8), 083127, (2019). [CrossRef]

[26] Liu, X., Arfan, M., Ur Rahman, M., & Fatima, B. Analysis of SIQR type mathematical model under Atangana-Baleanu fractional differential operator. *Computer Methods in Biomechanics and Biomedical Engineering*, 26(1), 98-112, (2022). [CrossRef]

[27] Losada, J., & Nieto, J.J. Properties of a new fractional derivative without singular kernel. *Progress in Fractional Differentiation and Application*, 1(2), 87-92, (2015). [CrossRef]

[28] Özköse, F., Şenel, M.T., & Habbireeh, R. Fractional-order mathematical modelling of cancer cells-cancer stem cells-immune system interaction with chemotherapy. *Mathematical Modelling and Numerical Simulation with Applications*, 1(2), 67-83, (2021). [CrossRef]

[29] Omame, A., Abbas, M., & Onyenegecha, C.P. A fractional-order model for COVID-19 and tuberculosis co-infection using Atangana-Baleanu derivative. *Chaos Solitons & Fractals*, 153, 111486, (2021). [CrossRef]

[30] Uçar, E., Uçar, S., Evirgen, F., & Özdemir, N. A fractional SAIDR model in the frame of Atangana-Baleanu derivative. *Fractal and Fractional*, (2021). [CrossRef]

[31] Uçar, S. Analysis of a basic SEIRA model with Atangana-Baleanu derivative. *AIMS Mathematics*, (2020). [CrossRef]

[32] Omame, A., Abbas, M., & Abdel-Aty, A.H. Assessing the impact of SARS-CoV-2 infection on the dynamics of dengue and HIV via fractional derivatives. *Chaos Solitons & Fractals*, 162, 112427, (2022). [CrossRef]

[33] Blayneh, K.W., Cao, Y., & Kwon, H.D. Optimal control of vector-borne disease: treatment and prevention. *Discrete and Continuous Dynamical Systems B*, 11(3), 587-611, (2009). [CrossRef]

[34] Ishikawa, H., Ishii, A., Nagai, N., Ohmae, H., Harada, M., Suguri, S., & Leafasia, J. A mathematical model for the transmission of Plasmodium vivax malaria. *Parasitology International*, 52(1), 81-93, (2003). [CrossRef]

[35] Aron, J.L., & May, R.M. The population dynamics of malaria. In: *Anderson RM(ed) Population dynamics of infectious diseases* (pp. 139-179). London: Chapman and Hall, (1982). [CrossRef]

[36] Smith, R.J., & Hove-Musekwa, S.D. Determining effective spraying periods to control malaria via indoor residual spraying in Sub-Saharan Africa. *Journal of Applied Mathematics and Decision Sciences*, 745463, (2008). [CrossRef]

[37] Buonomo, B. Analysis of a malaria model with mosquito host choice and bed-net control. *International Journal of Biomathematics*, 8(6), 1550077, (2015). [CrossRef]

[38] Nielan, R.L.M., Schaefer, E., Gaff, H., Fister, K.R., & Lenhart, S. Modeling optimal control intervention strategies for cholera. *Bulletin of Mathematical Biology*, 72, 2004-2018, (2010). [CrossRef]

[39] Owolabi, K.M., & Atangana, A. *Numerical Methods for Fractional Differentiation*. Singapore: Springer Nature, (2019). [CrossRef]

[40] Thabet, S.T.M., Abdo, M.S., & Shah, K. Theoretical and numerical analysis for transmission dynamics of COVID-19 mathematical model involving Caputo–Fabrizio derivative. *Advances in Differential Equations*, 184, (2021). [CrossRef]

[41] Van den Driessche, P., & Watmough, J. Reproduction numbers and sub-threshold endemic equilibria for compartmental models of disease transmission. *Mathematical Biosciences*, 180(1-2), 29-48, (2002). [CrossRef]

[42] Toufik, M., & Atangana, A. New numerical approximation of fractional derivative with non-local and non-singular kernel: application to chaotic models. *The European Physical Journal Plus*, 132, 444, (2017). [CrossRef]

Mathematical Modelling and Numerical Simulation with Applications (MMNSA)
(https://dergipark.org.tr/en/pub/mmnsa)

How to cite this article: Iwa, L.L., Nwajeri, U.K., Atede, A.O., Panle, A.B. & Egeonu, K.U. (2023). Malaria and cholera co-dynamic model analysis furnished with fractional-order differential equations. *Mathematical Modelling and Numerical Simulation with Applications*, 3(1), 33-57. https://doi.org/10.53391/mmnsa.1273982

Mathematical Modelling and Numerical Simulation with Applications, 2023, 3(1), 58–73

https://dergipark.org.tr/en/pub/mmnsa
ISSN Online: 2791-8564 / Open Access
https://doi.org/10.53391/mmnsa.1274004

RESEARCH PAPER

Modelling Influenza A disease dynamics under Caputo–Fabrizio fractional derivative with distinct contact rates

Fırat Evirgen [1,*,‡], **Esmehan Uçar** [1,‡], **Sümeyra Uçar** [1,‡] **and Necati Özdemir** [1,‡]

[1]Department of Mathematics, Faculty of Arts and Sciences, Balıkesir University, 10145 Balıkesir, Türkiye

*Corresponding Author
‡fevirgen@balikesir.edu.tr (Fırat Evirgen); esucarr@gmail.com (Esmehan Uçar); sumeyraucar@balikesir.edu.tr (Sümeyra Uçar); nozdemir@balikesir.edu.tr (Necati Özdemir)

Abstract

The objective of this manuscript is to present a novel approach to modeling influenza A disease dynamics by incorporating the Caputo-Fabrizio (CF) fractional derivative operator into the model. Particularly distinct contact rates between exposed and infected individuals are taken into account in the model under study, and the fractional derivative concept is explored with respect to this component. We demonstrate the existence and uniqueness of the solution and obtain the series solution for all compartments using the Laplace transform method. The reproduction number of the Influenza A model, which was created to show the effectiveness of different contact rates, was obtained and examined in detail in this sense. To validate our approach, we applied the predictor-corrector method in the sense of the Caputo-Fabrizio fractional derivative and demonstrate the effectiveness of the fractional derivative in accurately predicting disease dynamics. Our findings suggest that the use of the Caputo-Fabrizio fractional derivative can provide valuable insights into the mechanisms underlying influenza A disease and enhance the accuracy of disease models.

Keywords: Fractional differential equations; fixed point theory; Caputo-Fabrizio derivative; influenza

AMS 2020 Classification: 34A08; 34A34; 93A30

1 Introduction

Influenza is an infectious respiratory disease caused by a single-stranded and segmented RNA virus in the Orthomyxoviridae family. Influenza is commonly known as "the flu". It has 3 different types, namely A, B, and C, and the type of virus responsible for large epidemics with high mortality

➤ **Received:** 14.02.2023 ➤ **Revised:** 25.03.2023 ➤ **Accepted:** 27.03.2023 ➤ **Published:** 31.03.2023

is often Influenza A. Influenza A viruses infect a range of mammalian (e.g. pigs and horses) and avian species, whereas type B and C infections are largely restricted to humans. Within this group of types, only types A and B are capable of causing severe illnesses in humans. Two glycoproteins, hemagglutinin (H) and neuraminidase (N), located on the outside of the viral particle, are used in the classification of influenza viruses. All 18 H and 11 R subtypes of influenza A viruses have been isolated from nature and described in the literature [1]. H1N1, H1N2, H2N2, H3N1, and others can be given as examples of this nomenclature. Like humans, every living thing has its own influenza virus. Influenza viruses in animals can be transmitted to humans and cause a pandemic that affects the whole world. The most important of these is the H1N1 subtype of influenza A, which caused the Spanish flu pandemic in 1918, the Russian flu pandemic in 1977, and the swine flu pandemic in 2009 [2]. These viruses lose their ability to cause an epidemic that will affect the whole world within a few years and take their place among seasonal influenza agents in the following years. Influenza viruses can easily be transmitted from sick people to other people, and the disease reaches its peak during the winter months when people spend more time indoors. Influenza is usually transmitted by the behavior of people who are sick, such as talking, coughing, and sneezing. More rarely, it can be transmitted by touching surfaces, tools, and equipment contaminated with virus-containing droplets. The flu is mild in many people and these people recover completely within a few days. However, it has a severe course in the elderly, young children, immune-deficient persons, and those with chronic diseases, and may cause hospitalizations and even death. This disease can cause a wide range of symptoms, ranging from mild to severe, including fever, sore throat, runny nose, headache, muscle pain, coughing, and fatigue, among others. Although drugs are used in the treatment of influenza, scientific studies have shown that the most effective way to prevent the disease is vaccination. However, the continuous mutation of the influenza virus requires that the vaccine be updated every year in order to be protected from the disease.

The course and effects of the disease can also be examined theoretically with mathematical models that will be created in the presence of up-to-date data. In addition, the fractional derivative concept has been adapted to add the memory effect to the mathematical models. Thereby, the instantaneous behavior of the dynamic system can be depicted with the effect of past accumulations. In this regard, many mathematical models, including integer and fractional order, have been created in the literature for the detailed analysis of various diseases such as cancer cells [3–5], varicella zoster virus [6], COVID-19 [7–9], plant disease [10], diabetes [11], prey-predator model [12], Nipah virus [13], childhood diseases [14], and hepatitis B [15]. Additionally, several studies have also been conducted regarding fractional derivative applications in various fields, such as optimal control [16, 17], fixed point theory [18–20], chaotic systems [21], and heat flow [22]. In the same way, a number of mathematical models developed in regard to influenza have attempted to contribute to the literature in this area. In 2004 Alexander et al. [23] created an SVIRS model and determined the threshold limit for vaccination, in order to reduce the spread of influenza in the community. Casagrandi et al. [24] adapted cross-immune individuals to the classical SIR model and examined its effects on the course of the disease. The transmission of the influenza virus between bird and human populations has been discussed in detail by the proposed model in [25]. With the model created in 2010 [26], the effects of wearing N95 and surgical masks on influenza were revealed with quantitative analyzes. To explain and understand the outbreaks of influenza A (H1N1), a nonlinear fractional order model is constructed in the Caputo sense [27], and the results are compared with the real data from 2009. A new model describing the transmission of the influenza virus by disease resistance in humans has been introduced in [28] and disease equilibrium points have been determined and stability analyses have been carried out. Furthermore, Jia and Xiao [29] discussed this model with nonlinear incidence rates. Partial differential equations have been

used in the study [30] to assess the impact of diffusion and advection on influenza A virus kinetics and localization in the human respiratory tract. Srivastava et al. [31] investigated the effect of the influenza virus on a cellular basis on a fractional order model, taking into account the components of the human immune system as antibodies, plasma cells, effector cells, and interferon. In [32] the authors, the influenza mathematical model is handled by considering two strains with two different incidence rates. The effects of COVID-19 and influenza diseases on each other were examined on a deterministic co-infection model created by Ojo et al. [33]. In addition, various control strategies have been developed with 3 control parameters added to the model. The course and quantitative analysis of the influenza A virus under the newly defined fractal-fractional operator is discussed in [34]. Derradji et al. [35] presented a fractional SEIRS model in the sense of Caputo-Fabrizio with disease resistance and a nonlinear generalized incidence rate. An influenza disease model with a cross-immune population was remodeled under the effect of the fractional order derivative and solved by the stochastic Levenberg-Marquardt backpropagation neural networks [36].

This study was motivated by the need to better understand the spread of influenza A, leading to the creation of an integer-order model. The model incorporates a novel approach whereby the contact rate for each exposed and infected individual is treated separately. Additionally, the model incorporates the use of the Caputo-Fabrizio fractional derivative operator.

This paper is organized in the following manner. In Section 2, some basic definitions of fractional calculus, which form the basis of the study, are reminded. In Section 3, the components of the proposed integer and fractional models and their biological meanings are described. The existence and uniqueness of the solution of the model under the CF derivative are detailed in Section 4. In Section 5, it is theoretically proven that the model components have a series solution using the Laplace transformed method. The effectiveness of contact rates corresponding to exposed and infected individuals on the reproduction number is discussed in Section 6. The effect of fractional derivatives of different order on the course of influenza disease is illustrated in Section 7. Moreover, in these simulations, the behavior of some model parameters under the fractional derivative was also examined in detail. Finally, the results are expressed in the conclusion section.

2 Some preliminaries

Here, we recall some fundamental notions.

Definition 1 *[37] Let $a < b, g \in H^1(a,b)$ and $\sigma \in (0,1)$, the Caputo-Fabrizio (CF) derivative is*

$$ {}^{CF}D_t^{\sigma}[g(t)] = \frac{F(\sigma)}{1-\sigma}\int_a^t g'(x)\exp\left[-\sigma\frac{(t-x)}{1-\sigma}\right]dx, $$

where $F(\sigma)$ is a normalization function and $F(0) = F(1) = 1$.

Definition 2 *[38] Let $\sigma \in (0,1)$. The fractional integral related to the CF derivative is defined by:*

$$ {}^{CF}I_t^{\sigma}[g(t)] = \frac{1-\sigma}{F(\sigma)}g(t) + \frac{\sigma}{F(\sigma)}\int_a^t g(\lambda)\,d\lambda. $$

Definition 3 *[38] The Laplace transform of CF derivative can be given*

$$ \mathfrak{L}\left[{}^{CF}D_t^{\sigma}[g(t)]\right] = \frac{s\mathfrak{L}[g(t)]}{s+\sigma(1-s)} - \frac{g(0)}{s+\sigma(1-s)}. $$

3 Mathematical model of Influenza A

In this section, an SEIRS model was developed by taking into account separate contact rates for exposed and infected individuals, as inspired by previous research [28, 29, 35]. The model compartments and the biological meanings of the parameters can be seen as follows:

$$\begin{aligned}
\frac{dS(t)}{dt} &= \Lambda - \gamma_1 S(t) E(t) - \gamma_2 S(t) I(t) + cE(t) + bI(t) + \alpha R(t) - \mu S(t), \\
\frac{dE(t)}{dt} &= \gamma_1 S(t) E(t) + \gamma_2 S(t) I(t) - (c + \varepsilon + \mu) E(t), \\
\frac{dI(t)}{dt} &= \varepsilon E(t) - (\beta + b + \mu) I(t), \\
\frac{dR(t)}{dt} &= \beta I(t) - (\alpha + \mu) R(t),
\end{aligned} \tag{1}$$

where $S(t)$ represents the number of susceptible individuals, $E(t)$ represents the number of exposed individuals, $I(t)$ represents the number of infected individuals, $R(t)$ represents the number of recovered individuals, Λ is a constant recruitment ratio of susceptible humans, γ_1 is the transmission rate of viruses by contact between susceptible and exposed individuals, γ_2 is the transmission rate of viruses by contact between susceptible and infected individuals, the rate at which an exposed person develops susceptibility without therapy is c, b is the rate at which an infected person develops into a susceptible person in the absence of therapy, $\varepsilon = \frac{1}{IIP}$ where IIP stands for the virus's intrinsic incubation period, the rate at which a recovered person becomes a vulnerable person once more is denoted by the symbol α, β is the rate at which the infectious person becomes to be the recovered person, and the population's natural death rate is expressed by the symbol μ.

The use of fractional derivatives in mathematical modeling has become increasingly popular in recent years. One of these fractional derivative definitions is the Caputo-Fabrizio fractional derivative which is a modification of the classical Caputo derivative by using an additional parameter to account for the non-locality of the fractional derivative. This additional parameter can help to better capture the complex behavior of real-world systems, such as in the spread of infectious diseases, where the contact rate between infected and susceptible individuals may vary over time and make more accurate predictions about their future behavior. Now, by replacing the time derivative with the CF fractional derivative operator, we moderate the system. As a result of this change, the dimensions on the right-hand side and the left-hand side of the page will differ. In order to resolve this issue, we adjust the fractional operator so that the sides are of the same dimension using an auxiliary parameter called κ [39]. Based on these explanations and CF fractional derivative, the model (1) take the following form:

$$\begin{aligned}
\kappa^{\sigma-1} {}^{CF}D_t^{\sigma} S(t) &= \Lambda - \gamma_1 S(t) E(t) - \gamma_2 S(t) I(t) + cE(t) + bI(t) + \alpha R(t) - \mu S(t), \\
\kappa^{\sigma-1} {}^{CF}D_t^{\sigma} E(t) &= \gamma_1 S(t) E(t) + \gamma_2 S(t) I(t) - (c + \varepsilon + \mu) E(t), \\
\kappa^{\sigma-1} {}^{CF}D_t^{\sigma} I(t) &= \varepsilon E(t) - (\beta + b + \mu) I(t), \\
\kappa^{\sigma-1} {}^{CF}D_t^{\sigma} R(t) &= \beta I(t) - (\alpha + \mu) R(t),
\end{aligned} \tag{2}$$

with the initial conditions $S(0) = S_0 \geq 0$, $E(0) = E_0 \geq 0$, $I(0) = I_0 \geq 0$ and $R(0) = R_0 \geq 0$.

4 Existence of solution

A natural question one might ask is whether the model we construct in order to describe a physical phenomenon appears accurate enough. In order to guarantee this, we can apply the theory of fixed points to our problem. We therefore use the aforementioned theory to demonstrate the existence of the solution for the relevant model (2).

$$\begin{aligned}
\Psi_1(t,S,E,I,R) &= \kappa^{1-\sigma}\left(\Lambda-\gamma_1 S(t)E(t)-\gamma_2 S(t)I(t)+cE(t)+bI(t)+\alpha R(t)-\mu S(t)\right),\\
\Psi_2(t,S,E,I,R) &= \kappa^{1-\sigma}\left(\gamma_1 S(t)E(t)+\gamma_2 S(t)I(t)-(c+\varepsilon+\mu)E(t)\right),\\
\Psi_3(t,S,E,I,R) &= \kappa^{1-\sigma}\left(\varepsilon E(t)-(\beta+b+\mu)I(t)\right),\\
\Psi_4(t,S,E,I,R) &= \kappa^{1-\sigma}\left(\beta I(t)-(\alpha+\mu)R(t)\right).
\end{aligned} \tag{3}$$

Applying the operator ${}^{CF}I_t^{\sigma}$ to the model (2) on both sides, we have

$$\begin{aligned}
S(t) &= S(0)+{}^{CF}I_t^{\sigma}\left[\Psi_1(t,S,E,I,R)\right],\\
E(t) &= E(0)+{}^{CF}I_t^{\sigma}\left[\Psi_2(t,S,E,I,R)\right],\\
I(t) &= I(0)+{}^{CF}I_t^{\sigma}\left[\Psi_3(t,S,E,I,R)\right],\\
R(t) &= R(0)+{}^{CF}I_t^{\sigma}\left[\Psi_4(t,S,E,I,R)\right].
\end{aligned} \tag{4}$$

Considering the right-hand side of the Eq. (4), we achieve

$$U(t)=U_0(t)+\frac{1-\sigma}{M(\sigma)}\left[\Psi(t,U(t))-\Psi_0(t)\right]+\frac{\sigma}{M(\sigma)}\int_0^t \Psi(\theta,U(\theta))\,d\theta, \tag{5}$$

where

$$U(t)=\begin{cases} S(t)\\ E(t)\\ I(t)\\ R(t)\end{cases},\quad U_0(t)=\begin{cases} S(0)\\ E(0)\\ I(0)\\ R(0)\end{cases},\quad \Psi(t,U(t))=\begin{cases} \Psi_1(t,S,E,I,R)\\ \Psi_2(t,S,E,I,R)\\ \Psi_3(t,S,E,I,R)\\ \Psi_4(t,S,E,I,R)\end{cases}. \tag{6}$$

Let

$$B_i=\sup_{t\in[t-d,t+d]}\left\|\Psi_i(t,S,E,I,R)\right\|,\ \text{for } i=1,2,3,4$$

and

$$C[d,b_i]=[t-d,t+d]\times[u-c_i,u+c_i]=D\times D_i \text{ for } i=1,2,3,4.$$

Suppose that a norm on $C[d,b_i]$ for $i=1,2,3,4$ as follows:

$$\left\|U(t)\right\|_{\infty}=\sup_{t\in[t-d,t+d]}\left|U(t)\right|. \tag{7}$$

Consider the Picard operator

$$\theta : C\left(D, D_1, D_2, D_3, D_4\right) \to C\left(D, D_1, D_2, D_3, D_4\right),$$

given as

$$\theta U\left(t\right) = U_0\left(t\right) + \frac{1-\sigma}{M\left(\sigma\right)}\Psi\left(t, U\left(t\right)\right) + \frac{\sigma}{M\left(\sigma\right)}\int_0^t \Psi\left(s, U\left(s\right)\right) ds. \tag{8}$$

Suppose that the solutions of the model Eq. (2) are bounded within a time period, that is

$$\|U\| \leq \max\{d_1, d_2, d_3, d_4\}. \tag{9}$$

Supposing that $d = \frac{1+\sigma t_0}{M(\sigma)}$, $B = \max\{B_i\}$ for $i = 1, 2, 3, 4$ and $t_0 = \max\{t \in D\}$

$$\begin{aligned}
\|\theta U\left(t\right) - U_0\left(t\right)\| &= \sup_{t\in D}\left|\frac{1-\sigma}{M\left(\sigma\right)}\Psi\left(t, U\left(t\right)\right) + \frac{\sigma}{M\left(\sigma\right)}\int_0^t \Psi\left(s, U\left(s\right)\right) ds\right| \\
&\leq \frac{1-\sigma}{M\left(\sigma\right)}\sup_{t\in D}\left|\Psi\left(t, U\left(t\right)\right)\right| + \frac{\sigma}{M\left(\sigma\right)}\sup_{t\in D}\left|\int_0^t \Psi\left(s, U\left(s\right)\right) ds\right| \\
&\leq \left(\frac{1-\sigma}{M\left(\sigma\right)} + \frac{\sigma}{M\left(\sigma\right)}\right) B \\
&\leq \left(\frac{1+\sigma\left(t_0 - 1\right)}{M\left(\sigma\right)}\right) B \\
&< dB \\
&\leq \bar{d},
\end{aligned} \tag{10}$$

which satisfies $d < \frac{\bar{d}}{B}$. Now, we consider the following inequality:

$$\|\theta U_1 - \theta U_2\| = \sup_{t\in D}\left|U_1 - U_2\right|. \tag{11}$$

$$\begin{aligned}
\|\theta U_1 - \theta U_2\| &= \sup_{t\in D}\left|\frac{1-\sigma}{M\left(\sigma\right)}\left(\Psi\left(s, U_1\left(t\right)\right) - \Psi\left(s, U_2\left(t\right)\right)\right)\right. \\
&\quad \left. + \frac{\sigma}{M\left(\sigma\right)}\int_0^t \left(\Psi\left(s, U_1\left(s\right)\right) - \Psi\left(s, U_2\left(s\right)\right)\right) ds\right| \\
&\leq \frac{1-\sigma}{M\left(\sigma\right)}k_1\left|U_1\left(t\right) - U_2\left(t\right)\right| + \frac{\sigma}{M\left(\sigma\right)}k_1\int_0^t \left|U_1\left(s\right) - U_2\left(s\right)\right| ds \\
&\leq \left(\frac{1-\sigma}{M\left(\sigma\right)}k_1 + \frac{\sigma k_1}{M\left(\sigma\right)}t_0\right)\left|U_1 - U_2\right| \\
&\leq dk_1\left|U_1 - U_2\right|,
\end{aligned}$$

where $k_1 < 1$. Since Ψ is a contraction, then we have $k_1 d < 1$. Thus, the operator θ is contraction. So the model (2) has a unique solution.

5 General algorithm for the fractional model

In this section, we give a series solution for our fractional model. Applying Laplace transform to the model (2), we find

$$\begin{aligned}
\mathfrak{L}\left[S\left(t\right)\right]-S\left(0\right) &= \frac{s+\sigma\left(1-s\right)}{s}\mathfrak{L}\left[\begin{array}{c}\kappa^{1-\sigma}\left(\Lambda-\gamma_1 S\left(t\right)E\left(t\right)-\gamma_2 S\left(t\right)I\left(t\right)\right.\\ \left.+cE\left(t\right)+bI\left(t\right)+\alpha R\left(t\right)-\mu S\left(t\right)\right)\end{array}\right],\\
\mathfrak{L}\left[E\left(t\right)\right]-E\left(0\right) &= \frac{s+\sigma\left(1-s\right)}{s}\mathfrak{L}\left[\kappa^{1-\sigma}\left(\gamma_1 S\left(t\right)E\left(t\right)+\gamma_2 S\left(t\right)I\left(t\right)-\left(c+\varepsilon+\mu\right)E\left(t\right)\right)\right],\\
\mathfrak{L}\left[I\left(t\right)\right]-I\left(0\right) &= \frac{s+\sigma\left(1-s\right)}{s}\mathfrak{L}\left[\kappa^{1-\sigma}\left(\varepsilon E\left(t\right)-\left(\beta+b+\mu\right)I\left(t\right)\right)\right],\\
\mathfrak{L}\left[R\left(t\right)\right]-R\left(0\right) &= \frac{s+\sigma\left(1-s\right)}{s}\mathfrak{L}\left[\kappa^{1-\sigma}\left(\beta I\left(t\right)-\left(\alpha+\mu\right)R\left(t\right)\right)\right].
\end{aligned} \tag{12}$$

Take into account the series solution in the shape of:

$$\begin{aligned}
S\left(t\right) &= \sum_{p=0}^{\infty} S_p\left(t\right),\ E\left(t\right) = \sum_{p=0}^{\infty} E_p\left(t\right),\\
I\left(t\right) &= \sum_{p=0}^{\infty} I_p\left(t\right),\ R\left(t\right) = \sum_{p=0}^{\infty} R_p\left(t\right).
\end{aligned} \tag{13}$$

Moreover, the nonlinear terms $E\left(t\right)S\left(t\right)$ and $I\left(t\right)S\left(t\right)$ are decomposed in form of polynomials:

$$E\left(t\right)S\left(t\right) = \sum_{p=0}^{\infty} A_p\left(E,S\right),\ I\left(t\right)S\left(t\right) = \sum_{p=0}^{\infty} B_p\left(I,S\right),$$

where the "Adomian polynomial" $A_p\left(E,S\right)$ may be defined as:

$$A_p\left(E,S\right) = \frac{1}{p!}\frac{d^p}{d\lambda^p}\left[\sum_{i=0}^{p}\lambda^i E_i\left(t\right)\sum_{i=0}^{p}\lambda^i S_i\left(t\right)\right]\Bigg|_{\lambda=0}.$$

In a similar way, the polynomial B_p can be given. The system (12) can be converted to

$$\mathfrak{L}\left[\sum_{p=0}^{\infty} S_p\left(t\right)\right] = \frac{S(0)}{s} + \frac{s+\sigma(1-s)}{s}\mathfrak{L}\left[\kappa^{1-\sigma}\left(\begin{array}{c}\Lambda-\gamma_1\sum_{p=0}^{\infty}A_p\left(E,S\right)-\gamma_2\sum_{p=0}^{\infty}B_p\left(I,S\right)+c\sum_{p=0}^{\infty}E_p\left(t\right)\\ +b\sum_{p=0}^{\infty}I_p\left(t\right)+\alpha\sum_{p=0}^{\infty}R_p\left(t\right)-\mu\sum_{p=0}^{\infty}S_p\left(t\right)\end{array}\right)\right],$$

$$\mathfrak{L}\left[\sum_{p=0}^{\infty} E_p\left(t\right)\right] = \frac{E(0)}{s} + \frac{s+\sigma(1-s)}{s}\mathfrak{L}\left[\kappa^{1-\sigma}\left(\begin{array}{c}\gamma_1\sum_{p=0}^{\infty}A_p\left(E,S\right)+\gamma_2\sum_{p=0}^{\infty}B_p\left(I,S\right)\\ -\left(c+\varepsilon+\mu\right)\sum_{p=0}^{\infty}E_p\left(t\right)\end{array}\right)\right],$$

$$\begin{aligned}
\mathfrak{L}\left[\sum_{k=0}^{\infty} I_p(t)\right] &= \frac{I(0)}{s} + \frac{s+\sigma(1-s)}{s}\mathfrak{L}\left[\kappa^{1-\sigma}\left(\varepsilon\sum_{p=0}^{\infty} E_p(t) - (\beta+b+\mu)\sum_{p=0}^{\infty} I_p(t)\right)\right], \\
\mathfrak{L}\left[\sum_{p=0}^{\infty} R_p(t)\right] &= \frac{R(0)}{s} + \frac{s+\sigma(1-s)}{s}\mathfrak{L}\left[\kappa^{1-\sigma}\left(\beta\sum_{p=0}^{\infty} I_p(t) - (\alpha+\mu)\sum_{p=0}^{\infty} R_p(t)\right)\right]. \qquad (14)
\end{aligned}$$

Now comparing both sides (14) term by term, we have

$$\begin{aligned}
&\mathfrak{L}[S_0(t)] = \frac{S_0}{s}, \mathfrak{L}[E_0(t)] = \frac{E_0}{s}, \mathfrak{L}[I_0(t)] = \frac{I_0}{s}, \mathfrak{L}[R_0(t)] = \frac{R_0}{s}. \\
&\mathfrak{L}[S_1(t)] = \frac{s+\sigma(1-s)}{s}\mathfrak{L}\left[\kappa^{1-\sigma}\left(\lambda - \gamma_1 A_0(E,S) - \gamma_2 B_0(I,S) - cE_0 + bI_0 + \alpha R_0 - \mu S_0\right)\right], \\
&\mathfrak{L}[E_1(t)] = \frac{s+\sigma(1-s)}{s}\mathfrak{L}\left[\kappa^{1-\sigma}\left(\gamma_1 A_0(E,S) + \gamma_2 B_0(I,S) - (c+\varepsilon+\mu)E_0\right)\right], \\
&\mathfrak{L}[I_1(t)] = \frac{s+\sigma(1-s)}{s}\mathfrak{L}\left[\kappa^{1-\sigma}\left(\varepsilon E_0 - (\beta+b+\mu)I_0\right)\right], \\
&\mathfrak{L}[R_1(t)] = \frac{s+\sigma(1-s)}{s}\mathfrak{L}\left[\kappa^{1-\sigma}\left(\beta I_0 - (\alpha+\mu)R_0\right)\right], \\
&\mathfrak{L}[S_2(t)] = \frac{s+\sigma(1-s)}{s}\mathfrak{L}\left[\kappa^{1-\sigma}\left(\Lambda - \gamma_1 A_1(E,S) - \gamma_2 B_1(I,S) - cE_1 + bI_1 + \alpha R_1 - \mu S_1\right)\right], \\
&\mathfrak{L}[E_2(t)] = \frac{s+\sigma(1-s)}{s}\mathfrak{L}\left[\kappa^{1-\sigma}\left(\gamma_1 A_1(E,S) + \gamma_2 B_1(I,S) - (c+\varepsilon+\mu)E_1\right)\right], \\
&\mathfrak{L}[I_2(t)] = \frac{s+\sigma(1-s)}{s}\mathfrak{L}\left[\kappa^{1-\sigma}\left(\varepsilon E_1 - (\beta+b+\mu)I_1\right)\right], \\
&\mathfrak{L}[R_2(t)] = \frac{s+\sigma(1-s)}{s}\mathfrak{L}\left[\kappa^{1-\sigma}\left(\beta I_1 - (\alpha+\mu)R_1\right)\right], \\
&\qquad\vdots \\
&\mathfrak{L}\left[S_{p+1}(t)\right] = \frac{s+\sigma(1-s)}{s}\mathfrak{L}\left[\kappa^{1-\sigma}\left(\gamma_1 A_p(E,S) - \gamma_2 B_p(I,S) - cE_p + bI_p + \alpha R_p - \mu S_p\right)\right], \\
&\mathfrak{L}\left[E_{p+1}(t)\right] = \frac{s+\sigma(1-s)}{s}\mathfrak{L}\left[\kappa^{1-\sigma}\left(\Lambda - \gamma_1 A_p(E,S) + \gamma_2 B_p(I,S) - (c+\varepsilon+\mu)E_p\right)\right], \\
&\mathfrak{L}\left[I_{p+1}(t)\right] = \frac{s+\sigma(1-s)}{s}\mathfrak{L}\left[\kappa^{1-\sigma}\left(\varepsilon E_p - (\beta+b+\mu)I_p\right)\right], \\
&\mathfrak{L}\left[R_{p+1}(t)\right] = \frac{s+\sigma(1-s)}{s}\mathfrak{L}\left[\kappa^{1-\sigma}\left(\beta I_p - (\alpha+\mu)R_p\right)\right],\ p \geq 0. \qquad (15)
\end{aligned}$$

Implementing the inverse Laplace transform to Eq. (15), we obtain

$$\begin{aligned}
&S_0(t) = S_0, E_0(t) = E_0, I_0(t) = I_0, R_0(t) = R_0. \\
&S_1(t) = \left[\kappa^{1-\sigma}\left(\Lambda - \gamma_1 A_0(E,S) - \gamma_2 B_0(I,S) - cE_0 + bI_0 + \alpha R_0 - \mu S_0\right)\right](1+\sigma(t-1)), \\
&E_1(t) = \left[\kappa^{1-\sigma}\left(\gamma_1 A_0(E,S) + \gamma_2 B_0(I,S) - (c+\varepsilon+\mu)E_0\right)\right](1+\sigma(t-1)), \\
&I_1(t) = \left[\kappa^{1-\sigma}\left(\varepsilon E_0 - (\beta+b+\mu)I_0\right)\right](1+\sigma(t-1)), \\
&R_1(t) = \left[\kappa^{1-\sigma}\left(\beta I_0 - (\alpha+\mu)R_0\right)\right](1+\sigma(t-1)), \qquad (16) \\
&\quad\vdots
\end{aligned}$$

Continuing in the same direction, we acquire the other terms. The desired outcome can be stated as:

$$S(t)=\sum_{p=0}^{\infty}S_p(t),E(t)=\sum_{p=0}^{\infty}E_p(t),$$
$$I(t)=\sum_{p=0}^{\infty}I_p(t),R(t)=\sum_{p=0}^{\infty}R_p(t). \tag{17}$$

6 Reproduction number

The reproduction number, denoted as R_0, is a mathematical term that is commonly used in epidemiology to represent the average number of people that one infected person will transmit a disease to in a population where everyone is susceptible to the disease, in the absence of any interventions like vaccines or treatment. The R_0 is determined by using the Next Generation Matrix Method (NGMM) [40, 41]. Firstly, the right side of the model (2) is considered as $\mathcal{F}$-$\mathcal{V}$, where $\mathcal{F}$ and $\mathcal{V}$ demonstrate the transmission part and the transition part, as follow respectively

$$\mathcal{F}=\kappa^{1-\sigma}\begin{pmatrix}E\,S\,\gamma_1+I\,S\,\gamma_2\\0\end{pmatrix}\quad\text{and}\quad\mathcal{V}=\kappa^{1-\sigma}\begin{pmatrix}E\,(c+\varepsilon+\mu)\\I\,(b+\beta+\mu)-E\,\varepsilon\end{pmatrix}.$$

Then, if the Jacobian matrices of the $\mathcal{F}$ and $\mathcal{V}$ are calculated according to the E and I compartments and written instead of the disease-free equilibrium point $\mathcal{E}_0=(S,E,I,R)=\left(\frac{\Lambda}{\mu},0,0,0\right)$ of the model, we get

$$\mathbb{F}=\kappa^{1-\sigma}\begin{pmatrix}\frac{\Lambda\,\gamma_1}{\mu}&\frac{\Lambda\,\gamma_2}{\mu}\\0&0\end{pmatrix}\quad\text{and}\quad\mathbb{V}=\kappa^{1-\sigma}\begin{pmatrix}c+\varepsilon+\mu&0\\-\varepsilon&b+\beta+\mu\end{pmatrix}.$$

Thus, the next generation matrix $\left(\mathbb{F}\mathbb{V}^{-1}\right)$ of the model (2) is obtained and its spectral radius gives the reproduction number R_0 as follow:

$$\mathbb{F}\mathbb{V}^{-1}=\begin{pmatrix}0\\\frac{\Lambda\,(b\,\gamma_1+\beta\,\gamma_1+\varepsilon\,\gamma_2+\gamma_1\,\mu)}{\mu\,(b+\beta+\mu)\,(c+\varepsilon+\mu)}\end{pmatrix}\rightarrow R_0=\frac{\Lambda\,(b\,\gamma_1+\beta\,\gamma_1+\varepsilon\,\gamma_2+\gamma_1\,\mu)}{\mu\,(b+\beta+\mu)\,(c+\varepsilon+\mu)}.$$

The critical value of contact rate refers to the threshold value of the average number of people that an infected individual comes into contact with per day, below which the reproduction number remains below 1. In other words, if the contact rate is lower than the critical value, then the disease will not spread widely in the population. In Figure 1 (a)-(b), the critical value of the contact rates is calculated as $\gamma_1=0.4637$ and $\gamma_2=0.72$ for the model (2). If the average number of contacts per exposed individual is less than 0.4637 and the average number of contacts per infected individual is less than 0.72, then the disease will not spread widely and the outbreak will be contained. However, if the contact rates γ_1 and γ_2 exceed the critical values, then the reproduction number will be greater than 1, and the disease will continue to spread in the population. This highlights the importance of public health measures such as social distancing, mask-wearing, and limiting large gatherings, which can reduce the contact rate and help bring the reproduction number below 1, leading to a decline in the number of new infections. In addition, the change in R_0 can also be observed in Figure 2 depending on the value of γ_1 and γ_2 that have been fixed in the range of 0 to

2. According to this simulation, γ_1 appears to spread the disease more effectively than γ_2, and considering the levels that R_0 can reach, it seems that influenza disease may have the potential to cause a pandemic again in the world in the future.

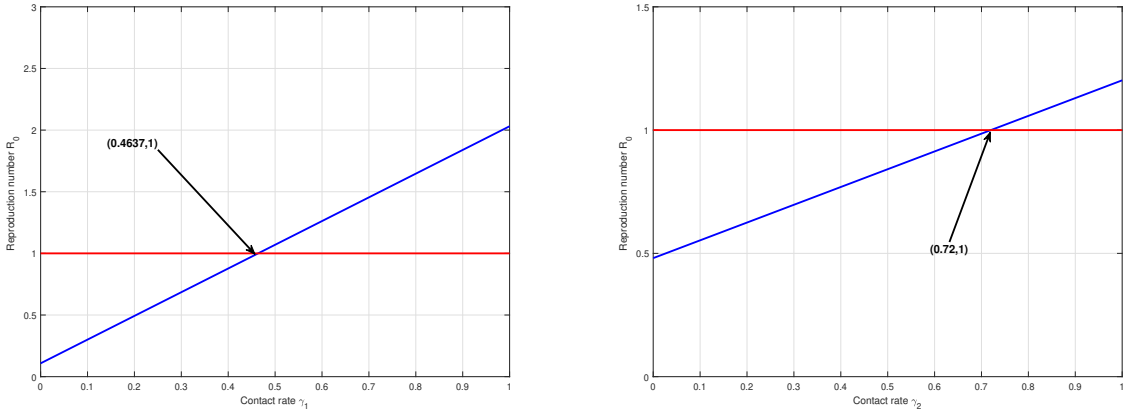

(a) γ_2 fixed as 0.15. **(b)**γ_1 fixed as 0.25.

Figure 1. The critical values of the contact rate γ_1 and γ_2 for the threshold value of $R_0 = 1$.

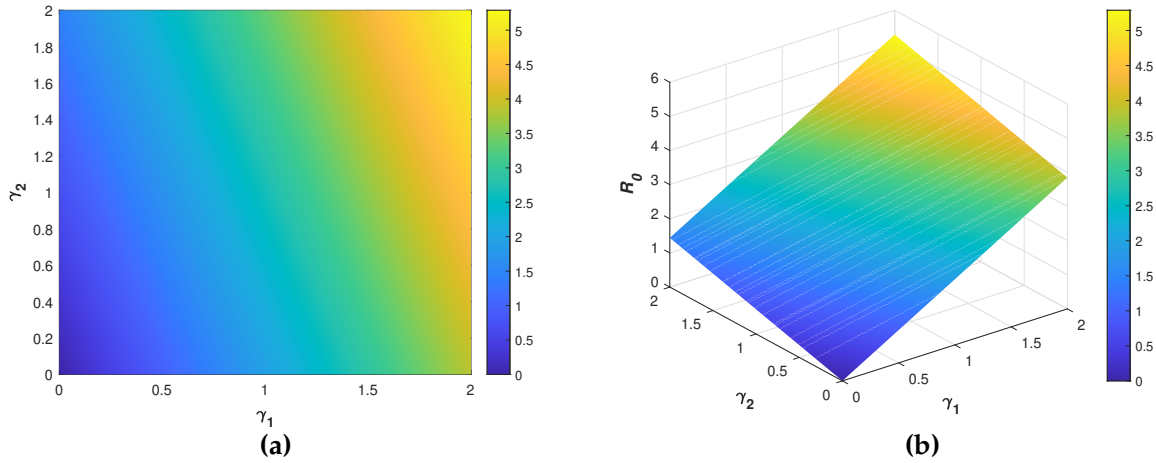

(a) **(b)**

Figure 2. Visualization of the variation in the reproduction number R_0 according to contact rates γ_1 and γ_2 with **(a)** Contour and **(b)** Surface plot.

7 Numerical results

In order to provide empirical evidence to support the theoretical findings obtained in this study, several numerical simulations were conducted. To approximate the solution to the differential equations in the model, we applied the predictor-corrector method in the sense of the Caputo-Fabrizio fractional derivative, which was introduced by Toh et al. [42]. To conduct these simulations, the initial conditions for the model components were set at $S(0) = 0.15$, $E(0) = 0.15$, $I(0) = 0.10$, and $R(0) = 0$.

Additionally, the values of the model parameters were assigned as $\Lambda = 0.25$, $\mu = 0.2$, $\gamma_1 = 0.25$, $\gamma_2 = 0.15$, $c = 0.15$, $b = 0.10$, $\alpha = 0.30$, $\epsilon = 0.30$, and $\beta = 0.5$. By utilizing these initial conditions

and parameter values, the simulations were able to provide insights into the behavior and characteristics of the model under distinct values of the fractional derivative. Through these simulations, it was possible to observe the impact of changes in the parameters and initial conditions on the model's predictions, thus allowing for a more comprehensive analysis of the model's dynamics. The impact of the fractional derivative of Caputo-Fabrizio sensitivity on the components of the influenza model is observed for arbitrarily selected orders, as shown in Figure 3-4. In addition to this, in Figure 5, a detailed explanation of the behavioral responses of exposed and infected individuals at various values of γ_1 and γ_2 contact rates is provided. There is a tendency for the number of exposed and infected individuals to increase when the threshold values for γ_1 and γ_2 contact rates are exceeded. When comparing the simulations in Figure 5 (a) and Figure 5 (b), it can be seen that the γ_1 contact rate is more dominant in the spread of the influenza virus compared to γ_2.

Moreover, this high transmission rate is achieved at lower values of γ_1 than γ_2. This result is also supported by the fact that γ_1 has a lower threshold value than γ_2, as seen in Figure 1 (a)-(b). This finding implies that the interaction with exposed individuals plays a more significant role in the spread of the influenza virus than the interaction with infected individuals.

There could be several reasons for this. One possible explanation is that exposed individuals may be more likely to transmit the virus to others due to their higher viral load or greater susceptibility to infection. Another possible explanation is that the timing of interactions with exposed individuals may be more critical for transmission than interactions with infected individuals. If individuals are more likely to interact with others during the early stages of the disease when they are exposed but not yet showing symptoms, this could contribute to the higher transmission rate among exposed individuals.

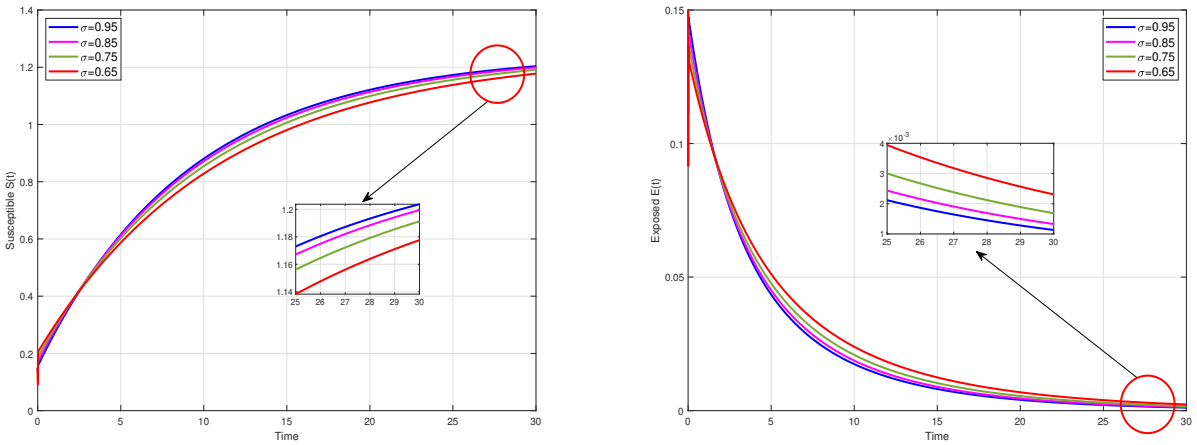

(a) **(b)**

Figure 3. The behavior of the model (2) compartments **(a)** Susceptible and **(b)** Exposed according to the different fractional orders $\sigma = 0.95, 0.85, 0.75, 0.65$.

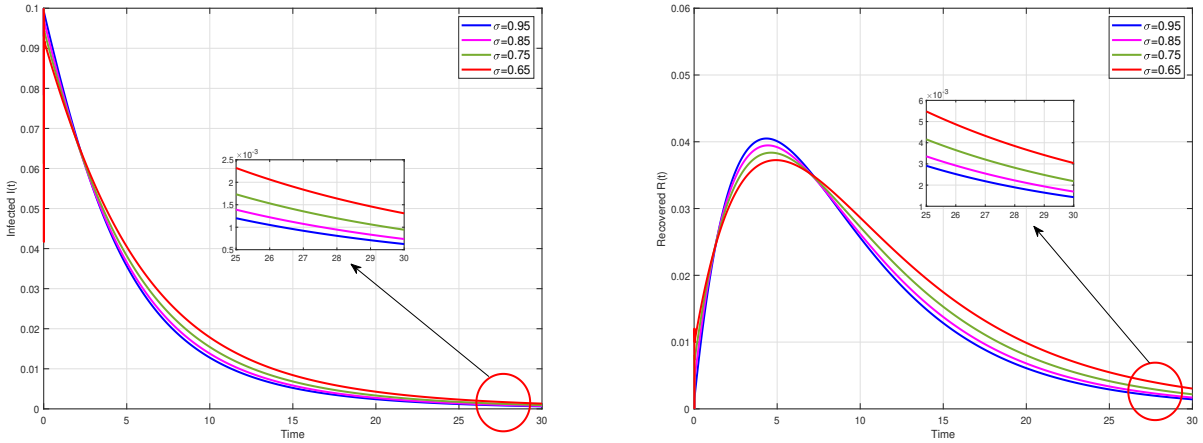

(a) **(b)**

Figure 4. The behavior of the model (2) compartments **(a)** Infected and **(b)** Recovered according to the different fractional orders $\sigma = 0.95, 0.85, 0.75, 0.65$.

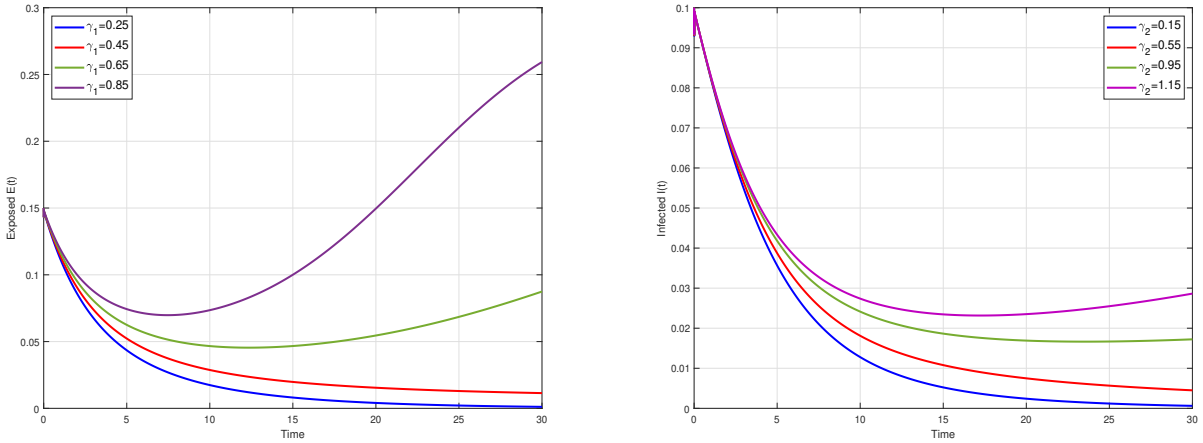

(a) **(b)**

Figure 5. The changes in the **(a)** Exposed $E(t)$ and **(b)** Infected $I(t)$ populations depending on the contact rates of virus transmission γ_1 and γ_2.

8 Conclusion

This manuscript presents a novel approach to modeling influenza A disease dynamics by incorporating the Caputo-Fabrizio fractional derivatives into the model. By considering distinct contact rates for exposed and infected individuals, the study explores the fractional derivative concept and demonstrates its effectiveness in predicting disease dynamics. The reproduction number of the influenza model was obtained and examined to show the effectiveness of different contact rates. In simulations, the γ_1 contact rate with exposed individuals played a more active role in disease spread. It can be thought that the reason for this was still at the beginning of the outbreak. Because, during the early stages of an outbreak, the contact rate with exposed individuals may be more important, as these individuals have not yet developed symptoms or been diagnosed with the disease, and therefore may not be aware that they are contagious. This makes them potentially

more dangerous to the population, as they may be spreading the disease unknowingly. Modeling the contact rate with exposed individuals can help to identify the potential spread of the disease before it is detected by traditional disease surveillance methods. The numerical simulations conducted in this study validate the proposed approach and suggest that the Caputo-Fabrizio fractional derivative can provide valuable insights into the mechanisms underlying influenza A disease. The findings of this study have important implications for improving the accuracy of disease models and developing more effective strategies for controlling the spread of influenza A. In future work, the model will be expanded to consider different incidence rates and further investigations will be conducted to examine the spread of Influenza A disease from different perspectives.

Declarations

Consent for publication

Not applicable.

Conflicts of interest

The authors declare that they have no conflict of interests.

Funding

Not applicable.

Author's contributions

F.E.: Conceptualization, Methodology, Software, Writing - Original Draft, E.U.: Conceptualization, Methodology, Writing - Original Draft, S.U.: Conceptualization, Methodology, Writing - Original Draft, N.O.: Methodology, Writing - Review and Editing. All authors discussed the results and contributed to the final manuscript.

Acknowledgements

Not applicable.

References

[1] Wu, Y., Wu, Y., Tefsen, B., Shi, Y. and Gao, G.F. Bat-derived influenza-like viruses H17N10 and H18N11. *Trends in Microbiology*, 22(4), 183-191, (2014). [CrossRef]

[2] Kilbourne, E.D. Influenza pandemics of the 20th century. *Emerging Infectious Diseases*, 12(1), 9-14, (2006). [CrossRef]

[3] Uçar, E., Ozdemir, N. and Altun, E. Fractional order model of immune cells influenced by cancer cells. *Mathematical Modeling Natural Phenomea*, 14(3), 12, (2019). [CrossRef]

[4] Özköse, F., Şenel, M.T. and Habbireeh, R. Fractional-order mathematical modelling of cancer cells-cancer stem cells-immune system interaction with chemotherapy. *Mathematical Modelling and Numerical Simulation with Applications*, 1(2), 67-83, (2021). [CrossRef]

[5] Uçar, E., Özdemir, N. and Altun, E. Qualitative analysis and numerical simulations of new model describing cancer. *Journal of Computational and Applied Mathematics*, 422, 114899, (2023). [CrossRef]

[6] Qureshi, S., Yusuf, A., Shaikh, A.A. and Inc, M. Transmission dynamics of varicella zoster

virus modeled by classical and novel fractional operators using real statistical data. *Physica A: Statistical Mechanics and its Applications*, 534, 122149, (2019). [CrossRef]

[7] Ahmad, S., Qiu, D. and ur Rahman, M. Dynamics of a fractional-order COVID-19 model under the nonsingular kernel of Caputo-Fabrizio operator. *Mathematical Modelling and Numerical Simulation with Applications*, 2(4), 228-243, (2022). [CrossRef]

[8] Hamou, A.A., Rasul, R.R.Q., Hammouch, Z. and Özdemir, N. Analysis and dynamics of a mathematical model to predict unreported cases of COVID-19 epidemic in Morocco. *Computational and Applied Mathematics*, 41, 289, (2022). [CrossRef]

[9] Okundalaye, O.O., Othman, W.A.M. and Oke, A.S. Toward an efficient approximate analytical solution for 4-compartment COVID-19 fractional mathematical model. *Journal of Computational and Applied Mathematics*, 416, 114506, (2022). [CrossRef]

[10] Koca, İ, Bulut, H. and Akçetin, E. A different approach for behavior of fractional plant virus model. *Journal of Nonlinear Sciences and Applications*, 15(3), 186-202, (2022). [CrossRef]

[11] Uçar, S., Ozdemir, N., Koca, I. and Altun, E. Novel analysis of the fractional glucose–insulin regulatory system with non-singular kernel derivative. *The European Physical Journal Plus*, 135(5), 1-18, (2020). [CrossRef]

[12] Naik, P.A., Eskandari, Z., Yavuz, M. and Zu, J. Complex dynamics of a discrete-time Bazykin-Berezovskaya prey-predator model with a strong Allee effect. *Journal of Computational and Applied Mathematics*, 413, 114401, (2022). [CrossRef]

[13] Evirgen, F. Transmission of Nipah virus dynamics under Caputo fractional derivative. *Journal of Computational and Applied Mathematics*, 418, 114654, (2023). [CrossRef]

[14] Olumide, O.O., Othman, W.A.M. and Ozdemir, N. Efficient solution of fractional-order SIR epidemic model of childhood diseases with optimal homotopy asymptotic method. *IEEE Access*, 10, 9395-9405, (2022). [CrossRef]

[15] Uçar, S. Analysis of hepatitis B disease with fractal-fractional Caputo derivative using real data from Turkey. *Journal of Computational and Applied Mathematics*, 419, 114692, (2023). [CrossRef]

[16] Tajadodi, H., Jafari, H. and Ncube, M.N. Genocchi polynomials as a tool for solving a class of fractional optimal control problems. *An International Journal of Optimization and Control: Theories & Applications (IJOCTA)*, 12(2), 160–168, (2022). [CrossRef]

[17] Chatterjee, A. and Pal, S. A predator-prey model for the optimal control of fish harvesting through the imposition of a tax. *An International Journal of Optimization and Control: Theories & Applications (IJOCTA)*, 13(1), 68–80, (2023). [CrossRef]

[18] Kaliraj, K., Viswanath, K.S., Logeswari, K. and Ravichandran, C. Analysis of Ffractional integro–differential equation with robin boundary conditions using topological degree method. *International Journal of Applied and Computational Mathematics*, 8(4), 176, (2022). [CrossRef]

[19] Manjula, M., Kaliraj, K., Botmart, T., Nisar, K.S. and Ravichandran, C. Existence, uniqueness and approximation of nonlocal fractional differential equation of sobolev type with impulses. *AIMS Mathematics*, 8(2), 4645-4665, (2023). [CrossRef]

[20] Vijayaraj, V., Ravichandran, C., Sawangtong, P. and Nisar, K.S. Existence results of Atangana-Baleanu fractional integro-differential inclusions of Sobolev type. *Alexandria Engineering Journal*, 66, 249-255, (2023). [CrossRef]

[21] Sene, N. Theory and applications of new fractional-order chaotic system under Caputo Operator. *An International Journal of Optimization and Control: Theories & Applications (IJOCTA)*, 12(1), 20-38, (2022). [CrossRef]

[22] Koca, I. Modeling the heat flow equation with fractional-fractal differentiation. *Chaos, Solitons & Fractals*, 128, 83-91, (2019). [CrossRef]

[23] Alexander, M.E., Bowman, C., Moghadas, S.M., Summers, R., Gumel, A.B. and Sahai, B.M. A vaccination model for transmission dynamics of influenza. *SIAM Journal on Applied Dynamical Systems*, 3(4), 503-524, (2004). [CrossRef]

[24] Casagrandi, R., Bolzoni, L., Levin, S.A. and Andreasen, V. The SIRC model and influenza A. *Mathematical Biosciences*, 200(2), 152-169, (2006). [CrossRef]

[25] Iwami, S., Takeuchi, Y. and Liu, X. Avian–human influenza epidemic model. *Mathematical Biosciences*, 207(1), 1-25, (2007). [CrossRef]

[26] Tracht, S.M., Del Valle, S.Y. and Hyman, J.M. Mathematical modeling of the effectiveness of facemasks in reducing the spread of novel influenza A (H1N1). *PloS One*, 5(2), e9018, (2010). [CrossRef]

[27] González-Parra, G., Arenas, A.J. and Chen-Charpentier, B.M. A fractional order epidemic model for the simulation of outbreaks of influenza A (H1N1). *Mathematical Methods in the Applied Sciences*, 37(15), 2218-2226, (2014). [CrossRef]

[28] Khanh, N.H. Stability analysis of an influenza virus model with disease resistance. *Journal of the Egyptian Mathematical Society*, 24, 193-199, (2016). [CrossRef]

[29] Jia, J. and Xiao, J. Stability analysis of a disease resistance SEIRS model with nonlinear incidence rate. *Advances in Difference Equations*, 75, (2018). [CrossRef]

[30] Quirouette, C., Younis, N.P., Reddy, M.B. and Beauchemin, C.A. A mathematical model describing the localization and spread of influenza A virus infection within the human respiratory tract. *PLoS Computational Biology*, 16(4), e1007705, (2020). [CrossRef]

[31] Srivastava, H.M., Saad, K.M., Gómez-Aguilar, J.F. and Almadiy, A.A. Some new mathematical models of the fractional-order system of human immune against IAV infection. *Mathematical Biosciences and Engineering*, 17(5), 4942-4969, (2020). [CrossRef]

[32] Baba, I.A., Ahmad, H., Alsulami, M.D., Abualnaja, K.M. and Altanji, M. A mathematical model to study resistance and non-resistance strains of influenza. *Results in Physics*, 26, 104390, (2021). [CrossRef]

[33] Ojo, M.M., Benson, T.O., Peter, O.J. and Goufo, E.F.D. Nonlinear optimal control strategies for a mathematical model of COVID-19 and influenza co-infection. *Physica A: Statistical Mechanics and its Applications*, 607, 128173, (2022). [CrossRef]

[34] Etemad, S., Avci, I., Kumar, P., Baleanu, D. and Rezapour, S. Some novel mathematical analysis on the fractal–fractional model of the AH1N1/09 virus and its generalized Caputo-type version. *Chaos, Solitons & Fractals*, 162, 112511, (2022). [CrossRef]

[35] Derradji, L.S., Hamidane, N. and Aouchal, S. A fractional SEIRS model with disease resistance and nonlinear generalized incidence rate in Caputo–Fabrizio sense. *Rendiconti del Circolo Matematico di Palermo Series 2*, 72(1), 81-98, (2023). [CrossRef]

[36] Sabir, Z., Said, S.B. and Al-Mdallal, Q. A fractional order numerical study for the influenza disease mathematical model. *Alexandria Engineering Journal*, 65, 615-626, (2023). [CrossRef]

[37] Caputo, M. and Fabrizio, M. A new definition of fractional derivative without singular kernel. *Progress in Fractional Differentiation and Applications*, 1, 73-85, (2015). [CrossRef]

[38] Atangana, A. and Talkahtani, B.S. Extension of the resistance, inductance, capacitance electrical circuit to fractional derivative without singular kernel. *Advances in Mechanical Engineering*,

7, 1-6, (2015). [CrossRef]

[39] Gomez-Aguilar, J.F., Rosales-García, J.J. and Bernal-Alvarado, J.J. Fractional mechanical oscillators. *Revista Mexicana Física*, 58, 348-352, (2012). [CrossRef]

[40] Driessche, V.P. and Watmough, J. Reproduction numbers and sub-threshold endemic equilibria for compartmental models of disease transmission. *Mathematical Biosciences*, 180(2), 29-48, (2002). [CrossRef]

[41] Diekmann, O., Heesterbeek, J.A.P. and Roberts, M.G. The construction of next-generation matrices for compartmental epidemic models. *Journal of the Royal Society Interface*, 7(47), 873-885, (2010). [CrossRef]

[42] Toh, Y.T., Phang, C. and Loh, J.R. New predictor-corrector scheme for solving nonlinear differential equations with Caputo-Fabrizio operator. *Mathematical Methods in the Applied Sciences*, 42, 175-185, (2019). [CrossRef]

Mathematical Modelling and Numerical Simulation with Applications (MMNSA)
(https://dergipark.org.tr/en/pub/mmnsa)

How to cite this article: Evirgen, F., Uçar, E., Uçar, S. & Özdemir, N. (2023). Modelling Influenza A disease dynamics under Caputo-Fabrizio fractional derivative with distinct contact rates. *Mathematical Modelling and Numerical Simulation with Applications*, 3(1), 58-73. https://doi.org/10.53391/mmnsa.1274004

Mathematical Modelling and Numerical Simulation with Applications, 2023, 3(1), 74–100

https://dergipark.org.tr/en/pub/mmnsa
ISSN Online: 2791-8564 / Open Access
https://doi.org/10.53391/mmnsa.1280184

RESEARCH PAPER

A modelling of bioconvective flow existing with tiny particles and quartic autocatalysis reaction across stratified upper horizontal surface of a paraboloid of revolution

Nehad Ali Shah [1,‡], **Amos Oladele Popoola** [2,‡], **Tosin Oreyeni** [3,*,‡], **Emmanuel Omokhuale** [4,‡] **and Muhammad Muhammad Altine** [5,‡]

[1]Department of Mechanical Engineering, Sejong University, Seoul 05006, South Korea, [2]Department of Mathematical Sciences, Osun State University, Osogbo, Nigeria, [3]Department of Physical Sciences, Mathematics Programme Unit, Precious Cornerstone University, Ibadan, Nigeria, [4]Department of Mathematical Sciences, Federal University Gusau, Nigeria, [5]Department of Mathematics, Federal University Birnin Kebbi, Kalgo, Nigeria

*Corresponding Author
‡nehadali199@sejong.ac.kr (Nehad Ali Shah); amos.popoola@uniosun.edu.ng (Amos Oladele Popoola); oreyenitos@gmail.com (Tosin Oreyeni); emmanuelomokhuale@yahoo.com (Emmanuel Omokhuale); altine@fubk.edu.ng (Muhammad Muhammad Altine)

Abstract

The study considers the case of the unequal diffusion coefficients of reactant A (bulk fluid) and reactant B (catalyst at the wall) with the dispersion of both nanoparticles and gyrotactic microorganisms of Erying-Powell fluid flow over a surface with non-uniform thickness in the presence of variable fluid properties and stratification. The numerical solution of the transformed governing equations is obtained by using the Runge-Kutta method and shooting techniques. The outcome of this study is that the increasing values of temperature-dependent thermal conductivity parameter lead to the augmentation of the kinetic energy which thereafter causes a significant enhancement of the fluid temperature.

Keywords: Darcy-Forchheimer; bioconvection; Erying-Powell fluid; stratification; nanofluids; autocatalysis; paraboloid of revolution

AMS 2020 Classification: 76D50; 35Q35; 76A05

1 Introduction

Stratification is an important component of heat and mass transfer which is referred to as the scientific or natural process that describes the production of layers of fluids as a result of the

➤ **Received:** 18.02.2023 ➤ **Revised:** 25.03.2023 ➤ **Accepted:** 27.03.2023 ➤ **Published:** 31.03.2023

mixing of various fluids with varied densities, temperature variances, and concentration differences. The idea behind this stratification phenomenon is useful in both natural and industrial processes such as the occurrence of flows in lakes, oceans, rivers, groundwater reservoirs, thermal energy storage systems, and heat release into the atmosphere. Recently, the effect of stratification on the hydromagnetic nanofluid flow along an exponentially stretching sensor plate was presented by Shamshuddin et al. [1]. Tamilzharasan et al. [2] discussed the mixed convention flow of Williamson fluid in a stratified porous medium. The impact of triple stratification on hydromagnetic flow with Soret and Dufour over a stretching cylinder was analyzed by Jagan et al. [3] Rehman et al. [4] studied thermally stratified Eyring-Powel fluid with melting heat phenomenon.

Oreyeni et al. [5] demonstrated the importance of triple stratifications in the dynamics of a micropolar fluid with nanoparticles and exponential heat production. They observed that increased stratification minimizes the temperature difference between the surface and the free stream, resulting in declination of fluid velocity and temperature. Olanrewaju et al. [6] analyzed the impact of double stratification and variable fluid properties on a chemically reacting upper-convected Maxwell fluid utilizing an analytic approach. The effect of stratification phenomena on a Sutterby nanofluid was discussed by Khan et al. [7]. Chen et al. [8] investigated thermophoretic Casson fluid flow with a magnetic dipole in a stratified environment. The bioconvective flow of Casson over a stratified cylinder was addressed by Dawar et al. [9]. Verma et al. [10] presented the existence of mixed convection and double stratification in Darcy-Forchheimer porous medium. The magnetohydrodynamic mixed convective flow of nanofluid with thermal stratification was considered by Mahmood et al. [11].

Nanofluid is defined as fluid with nanometer-sized particles suspended in conventional heat transfer fluids characterized by low thermal conductivity in order to improve the fluid's heat transfer efficiency. Researchers are interested in the flow of fluid when nanometer-sized particles are annotated in the flow field because of its vast variety of applications in biomedical and technical disciplines such as microelectronics, polymer extrusion, cancer treatment, safer surgery procedures, and microfluidics. Owing to a wide range of applications, nanofluid flow over various geometries has emerged as a fascinating and significant research area among academics. Koriko et al. [12] investigated the bioconvection flow of shear-thinning fluid employing active and passive controls of nanoparticles. It was observed that the presence of Brownian motion encourages the warming of particle molecules and increases thermal conductivity, resulting in an increase in fluid temperature. Shah et al. [13] analyzed the significance of Brownian motion and thermophoretic diffusion effects as major mechanisms for heat transfer in their study. Nadeem et al. [14] considered the numerical analysis for elastico-viscous fluid with the suspension of nanoparticles. Boundary layer flow of a nanofluid in the presence of variable suction and viscous dissipation over an exponentially stretched wall was discussed by Rao et al. [15]. Rasheed et al. [16] presented the significance of Joule heating on the hydromagnetic flow of Jeffery nanofluid flow over a stretching cylinder. Abbas et al. [17] studied the heat transfer of nanofluid along a vertical sheet with a magnetic effect. Other studies relating to the dynamics of nanofluid can be seen in [18–21].

The process by which one or more substances are changed into one or more new substances is known as a chemical reaction. During the course of a chemical reaction catalysis is known to be the process of accelerating the rate of the reaction by introducing a chemical component known as a catalyst which is frequently used to accelerate a chemical reaction. It is therefore believed that catalyzed reactions are classified into two types: homogeneously catalyzed reactions and heterogeneously catalyzed reactions. Both the reactant and the catalyst are present in the same phase in a homogeneously catalyzed reaction. This has a wide range of applications in

industry as it allows an increase in reaction rate without an increase in temperature. An example of homogeneous catalysis is the decomposition of ozone when Nitric oxide (NO) acts as a catalyst that affects the rate of the decomposition reaction. That is, $NO+O_3 \rightarrow NO_2+O_2$. When the reactant and catalyst are in separate stages the reaction is called heterogeneous catalyzed. The catalyst stays solid in this type of reaction whereas the reactants are gaseous or liquid. Example is the preparation of Ammonia (NH_3) when iron (Fe) is used as catalyst, i.e. $N_2+3H_2 \rightarrow 2NH_3$.
Researchers have looked into the analysis of boundary layer flow with homogeneous-heterogeneous reaction because of its importance in the industry. Sravanthi et al. [22] recently examined the flow of a magnetite-water nanofluid in the presence of homogeneous and heterogeneous effects. Alzahrani et al. [23] investigated the influence of thermosolutal Marangoni convection and nanoparticle aggregation on Oldyroyd-B fluid with homogeneous and heterogeneous catalytic reactions. Sarojamma et al. [24] investigated the Cattaneo-Christov model in the homogeneous-heterogeneous autocatalytic chemical reaction of micropolar fluid. They observed that with diffusion ratios, the concentration of homogenous bulk fluid with microstructures drops, and the concentration of catalyst at the surface augments. Animasaun et al. [25] described a boundary layer generated on the surface with a changeable thickness of Erying-Powel liquid subject to equal diffusivity. Hayat et al. [26] considered the impacts of homogeneous and heterogeneous reactions on nanofluid flow over a surface with non-uniform thickness. Zhao et al. [27] utilized Buongiorno's model in the analysis of nanofluid flow characteristics in the presence of homogeneous and heterogeneous reactions.
Bioconvection is a pattern generation process that happens in the suspension of motile microorganisms when they swim in a given direction in response to certain stimuli Platt [28]. Because of density stratification, motile gyrotactic bacteria swim in large numbers to the upper layer of the fluid causing instability. Unlike motile gyrotactic microorganisms, the flow of nanoparticles immersed in the base fluid is induced by both thermophoresis and the Brownian motion mechanisms in the nanofluid Ramzan et al. [29]. The fact that the dispersion of nanoparticles in the base fluid can maintain the stability of the suspension in light of the instability caused by the motile microbes must also be emphasized. Bioconvection phenomena are essential in meteorological and medicinal applications such as pharmaceutical formulation, biopolymer synthesis, and microbial-enhanced oil recovery. Zhang et al. [30] examined the relevance of bioconvection flow with nanoparticles in the presence of Lorentz force. Rao et al. [31] investigated the bioconvection flow of nanofluid across an isothermal vertical cone with a chemical reaction. Sankad et al. [32] demonstrated boundary layer bioconvective flow with variable wall temperatures and thermal radiation effects. Parveen [33] investigated the effect of Brownian and thermophoresis motion on the peristaltic mechanism of conductive nanofluid flow via an asymmetric channel. Naganthran et al. [34] investigated scaling group analysis of bioconvective micropolar fluid in a porous regime.
To the best of the authors' knowledge, the hydromagnetic flow of nanofluid bioconvection with stratifications has been examined. However, researchers have not studied the impact of bioconvection flow of an electrically conducting Erying-Powel fluid containing nanoparticles in the presence of variable fluid characteristics and a quartic autocatalytic type of chemical reaction subjected to stratification over a surface with non-uniform thickness. Furthermore, the work addresses the role of thermophoresis and Brownian motion effects in nanofluid bioconvection flow. Two unique forms of stratification, thermal and motile microorganisms are integrated into the model which has a wide variety of applications in thermal energy storage systems, lakes, reservoirs, and the removal of residual pollutants. During the course of the inquiry, the current communication gives answers to the following questions:

- What effect does Darcy-Forchheimer have on velocity and temperature distributions?

- What impact does the Brownian motion parameter have on the homogeneous bulk fluid and heterogeneous catalyst surface concentration distributions?
- What impact does space-based internal heat generation parameter pose on the temperature distribution and concentration distribution of heterogeneous catalysts at the surface?
- What effect do the temperature-dependent viscous and thermal conductivity parameters have on velocity and temperature distributions, respectively?

2 Mathematical formulation of governing equation

The paper delves into the two-dimensional steady flow of bioconvective Erying-Powell fluid containing nanoparticles along the upper horizontal surface of a paraboloid of revolution. The Cauchy stress tensor in an Eyring-Powell fluid model studied by Ramzan et al. [35] is regulated by the relation

$$\tau_{ij} = \mu \frac{\partial u_i}{\partial x_j} + \frac{1}{\beta} \sinh^{-1}\left(\frac{1}{g}\frac{\partial u_i}{\partial x_j}\right), \tag{1}$$

The first term depicts the viscosity effect while the second term depicts the elastic part. Here μ is viscosity and β and g are the Eyring-Powell and rheological fluid parameters. Following Hayat et al. [36], Using Maclaurin series expansion of the hyperbolic sine is sufficient to describe the fluid,

$$\sinh^{-1}\left(\frac{1}{g}\frac{\partial u_i}{\partial x_j}\right) \cong \frac{1}{g}\frac{\partial u_i}{\partial x_j} - \frac{1}{6}\left(\frac{1}{g}\frac{\partial u_i}{\partial x_j}\right)^3, \quad \left|\frac{1}{g}\frac{\partial u_i}{\partial x_j}\right| \ll 1, \tag{2}$$

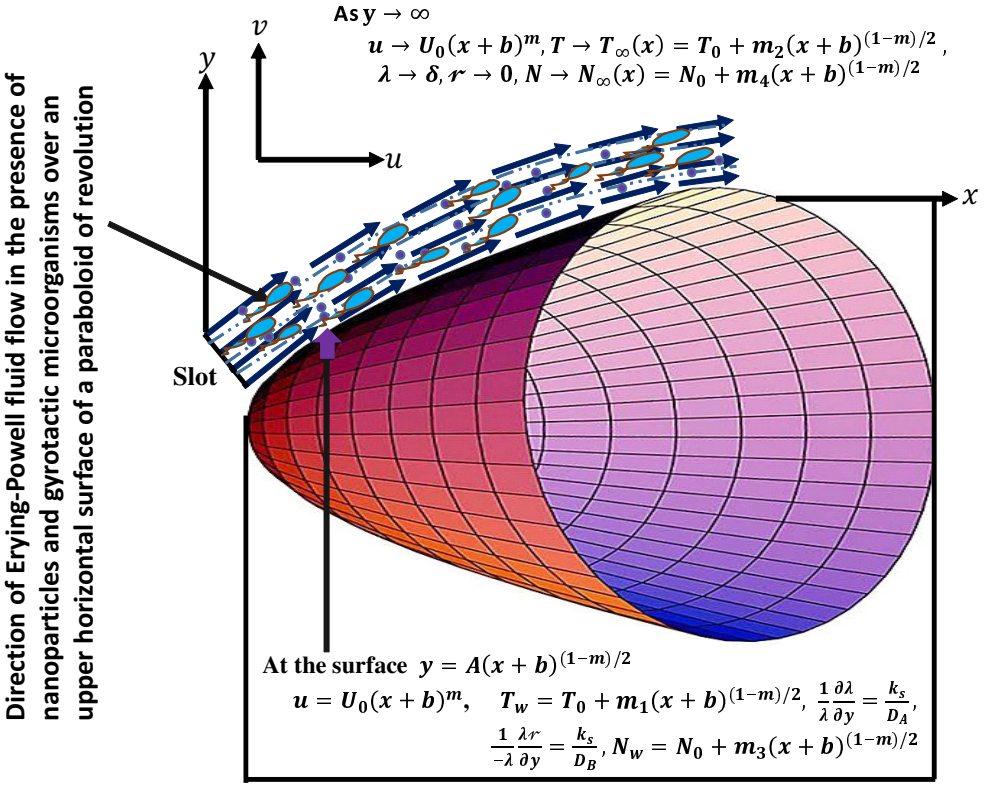

Figure 1. Geometry of Erying-Powell fluid flow over upper horizontal surface of a paraboloid of revolution

As the fluid flows along the upper horizontal surface of a paraboloid of revolution in a stratified domain, it is assumed that a quartic autocatalysis chemical reaction occurs between the reactant (bulk fluid) and concentrated catalyst on the wall. The chemical process is explained by Koriko and Animasaun [37] as a kind in which the homogeneous reaction is assumed to be by isothermal quartic autocatalytic kinetics and the heterogeneous reaction is considered to be by first-order kinetics. The concentrations of chemical species homogeneous bulk fluid (Eyring-Powell) A and heterogeneous catalyst B at the wall are denoted by λ and r, respectively. It is important to note that the Erying-Powell fluid flow over the surface with non-uniform thickness is assumed to occupy the domain $A(x+b)^{\frac{1-m}{2}} \leq y < \infty$, where $A \geq 0$. A and b are arbitrary constants associated with the thickness of the surface, m is velocity power index (see Fig. 1). In this study, m is less than 1. However, it is necessary to note that the flow of fluid along an upper horizontal surface of a paraboloid of revolution corresponds to $m < 1$(i.e$= 0.75$), Koriko et al. [25]. The upper horizontal surface of the paraboloid of revolution can be likened to the pointed upper surface of an aircraft, or the bonnet of a car. The fluid layers on an upper horizontal surface of the paraboloid of revolution are stretched with the velocity of $U_w = U_o(x+b)^m$, where U_o is the reference velocity. However, the velocities along $x, y-$ directions are $u(x,y)$ and $v(x,y)$, temperature is $T(x,y)$, concentrations of reactant A and reactant B are $\lambda(x,y)$ and $r(x,y)$ density of motile microorganisms is $N(x,y)$. To allow the microbes to live, water is assumed to be the base fluid. It is assumed that the suspension of nanoparticles inside the base fluid containing motile microorganisms will reduce bioconvection instability. Following Kuznetsov and Nield [38] and Rees et al. [39], microorganisms flux can be expressed as

$$\nabla . j = 0, \tag{3}$$

Following the idea of the homogeneous-heterogeneous reaction model proposed by Chaudhary and Merkin [40], Koriko et al. [41], Animasaun et al. [25], an isothermal quartic autocatalytic reaction in the homogeneous case is expressed as

$$A + 3B \rightarrow 4B, \tag{4}$$

where the chemical reaction rate $= k_h \lambda r^3$ while the chemical reaction on the surface of the catalyst is expressed as

$$A \rightarrow B, \tag{5}$$

where the chemical reaction rate $= k_s \lambda$. The concentrations of chemical reactants A and B are λ and r. Coefficient of chemical reaction rate are k_h and k_s. Following Kuznetsov [42], microorganisms flux j relating to the concentration of the homogeneous chemical reactant A is expressed as

$$j = Nv + N\widetilde{v} - D_m \nabla N, \qquad \widetilde{v} = \left(\frac{bW_c}{\Delta\lambda}\right)\nabla\lambda\,, \tag{6}$$

in which v is the velocity vector of the flow, $\widetilde{v}$ is the average swimming velocity vector of oxytactic microorganism, b is the chemotaxis contant, W_c is the maximum cell swimming speed and D_m is the diffusivity of microorganisms. With all the aforementioned assumptions, the governing equation that is suitable to analyze the bioconvective flow of Erying-Powell fluid with nanoparticles following the formulations of Refs. [25, 31, 36, 41] is presented as continuity

equation:

$$\frac{\partial u}{\partial x} + \frac{\partial v}{\partial y} = 0. \tag{7}$$

The momentum equation with the non-Newtonian fluid term and the magnetic field term takes the form

$$u\frac{\partial u}{\partial x} + v\frac{\partial u}{\partial y} = \frac{1}{\rho_f}\frac{\partial}{\partial y}\left[\left(\mu_f(T) + \frac{1}{\beta_j C}\right)\frac{\partial u}{\partial y}\right] - \frac{1}{2\beta_j C^3 \rho}\frac{\partial u}{\partial y}\frac{\partial u}{\partial y}\frac{\partial^2 u}{\partial y^2} - \frac{\sigma_f {B_o}^2 u}{\rho_f} - \frac{\mu(T)}{\rho}\frac{1}{k}u - \frac{b^*}{k}u^2. \tag{8}$$

The energy equation in which the exponential space-based heat generation, stratification, thermophoresis, and Brownian motion are incorporated and take the form

$$u\frac{\partial T}{\partial x} + v\frac{\partial T}{\partial y} = \frac{1}{(\rho C_p)_f}\frac{\partial}{\partial y}\left(\kappa_f(T)\frac{\partial T}{\partial y}\right) + \tau\left[D_B\frac{\partial T}{\partial y}\frac{\partial \lambda}{\partial y} + \frac{D_T}{T_\infty}\left(\frac{\partial T}{\partial y}\right)^2\right] + \frac{Q_o(T_w - T_0)}{(\rho C_p)_f} Exp^{-ny\sqrt{\frac{c(m+1)}{2\vartheta}}(x+b)^{\frac{m-1}{2}}}. \tag{9}$$

The effect of thermophoresis and the homogeneous-heterogeneous reaction model on reactant A and B concentrations is given as

$$u\frac{\partial \lambda}{\partial x} + v\frac{\partial \lambda}{\partial y} = D_A\frac{\partial^2 \lambda}{\partial y^2} - \frac{D_T}{T_\infty}\frac{\partial^2 T}{\partial y^2} - k_h \lambda r^3, \tag{10}$$

$$u\frac{\partial r}{\partial x} + v\frac{\partial r}{\partial y} = D_B\frac{\partial^2 r}{\partial y^2} + \frac{D_T}{T_\infty}\frac{\partial^2 T}{\partial y^2} + k_h \lambda r^3. \tag{11}$$

Density of gyrotactic microorganisms equation in the homogeneous bulk fluid is presented as

$$u\frac{\partial N}{\partial x} + v\frac{\partial N}{\partial y} + \frac{bW_c}{\Delta\lambda}\left[\frac{\partial}{\partial y}\left(N\frac{\partial \lambda}{\partial y}\right)\right] = D_n\frac{\partial^2 N}{\partial y^2}. \tag{12}$$

The associated boundary conditions that connect chemical changes of the reactants A and B at the surface, the thermal and motile microorganisms stratifications are expressed as

$$u = U_o(x+b)^m,\ v = 0,\ T = T_w,\ \frac{1}{\lambda}\frac{\partial \lambda}{\partial y} = \frac{k_s}{D_A},\ \frac{1}{-\lambda}\frac{\partial r}{\partial y} = \frac{k_s}{D_B}, N = N_w \text{ at } y = A(x+b)^{\frac{1-m}{2}}, \tag{13}$$

$$u \to 0, \quad T \to T_\infty, \quad \lambda \to \delta, \quad r \to 0 \quad N \to N_\infty \quad \text{as} \quad y \to \infty, \tag{14}$$

where β_j is the Erying-Powell fluid parameter κ is thermal conductivity, σ is the fluid electrical conductivity, ρ is the fluid density, B_o is the magnetic field strength, T is the fluid temperature, Q_o

is the heat generation/absorption, ρC_p is the heat capacity of the fluid.
The temperature-dependent viscosity mathematical model was developed using Batchelor's experimental data [43], as well as the mathematical model of temperature-dependent thermal conductivity of Charraudeau [44] and Yook et al. [45] as;

$$\mu_f(T) = \mu_f^*[1 + b(T_w - T)] \quad \text{and} \quad \kappa_f(T) = \kappa_f^*[1 + \delta(T - T_\infty)]. \tag{15}$$

Following [46–48], it is essential to indicate how stratification is incorporated into the energy and concentration equations as we express the thermal stratification at the wall (T_w) and solutal stratification at the wall (C_w) and the free stream temperature and concentration $(T_\infty,\ C_\infty)$ as

$$\begin{aligned} T_w - T_0 &= m_1(x+b)^{\frac{1-m}{2}} \quad \text{and} \quad T_\infty - T_0 = m_2(x+b)^{\frac{1-m}{2}}, \\ N_w - N_0 &= m_3(x+b)^{\frac{1-m}{2}} \quad \text{and} \quad N_\infty - N_0 = m_4(x+b)^{\frac{1-m}{2}}, \end{aligned} \tag{16}$$

where T_0 is the reference temperature, it is worth noting that stratification occurs for all points of x on the wall at $y = A(x+b)^{\frac{1-m}{2}}$ and also for all points of x at the ambient as $y \to \infty$.

The essential physical quantities of engineering in the Erying-Powell are expressed as in Animasaun et al. [25]

$$\begin{aligned} C_f &= \left[\left(\frac{\mu_f(T)}{\rho_f} + \frac{1}{\beta_j C}\right)\frac{\partial u}{\partial y} - \frac{2}{m+1}\frac{1}{\beta_j C^3}\left(\frac{\partial u}{\partial y}\right)^3\right]_{y=A(x+b)^{\frac{1-m}{2}}}, \\ Nu_x &= \frac{(x+b)\,q_w}{\kappa(T_w(x) - T_0)\left(\frac{m+1}{2}\right)^{\frac{1}{2}}}, \quad where \ \ q_w = -\kappa\frac{\partial T}{\partial y}\bigg|_{y=A(x+b)^{\frac{1-m}{2}}}. \end{aligned} \tag{17}$$

For the sake of transformation, the following similar transformations can be expressed as

$$u = \frac{\partial \psi}{\partial y},\ v = -\frac{\partial \psi}{\partial x},\ \eta = y\left(\frac{U_o(m+1)}{2\vartheta}\right)^{1/2}(x+b)^{\frac{m-1}{2}},\ \psi = \left(\frac{2\vartheta U_o}{m+1}\right)^{1/2}(x+b)^{\frac{m+1}{2}} f(\eta),$$

$$\theta(\eta) = \frac{T - T_\infty}{T_w - T_0}, \qquad \frac{\lambda}{\delta} = q(\eta), \quad \frac{r}{\delta} = s(\eta), \qquad \omega(\eta) = \frac{N - N_\infty}{N_w - N_0}. \tag{18}$$

Using the similar transformation, stream function $\psi(x,\ y)$ satisfies the continuity equation, the governing partial differential equations (8)-(12) together with the boundary conditions (13)-(14) are converted to the system of nonlinear differential equations expressed as

$$\begin{aligned} &\left([1 + (1 - \theta(\eta))\,\xi] + \varsigma - \varsigma\mathcal{H}\frac{(m+1)}{2}\frac{d^2f}{d\eta^2}\frac{d^2f}{d\eta^2}\right)\frac{d^3f}{d\eta^3} - \xi\frac{d^2f}{d\eta^2}\frac{d\theta}{d\eta} - \frac{2m}{m+1}\frac{df}{d\eta}\frac{df}{d\eta} \\ &+ f(\eta)\frac{d^2f}{d\eta^2} - \frac{2}{m+1}M\frac{df}{d\eta} - \frac{2}{m+1}[1 + (1-\theta)\,\xi]\,P_s\frac{df}{d\eta} - \frac{2}{m+1}F_sD_a^{-1}\frac{df}{d\eta}\frac{df}{d\eta} = 0, \end{aligned} \tag{19}$$

$$[1+\theta(\eta)\varepsilon]\frac{d^2\theta}{d\eta^2}-\frac{2}{m+1}P_r\theta(\eta)\frac{df}{d\eta}-\frac{2}{m+1}S_tP_r\frac{df}{d\eta}+P_rf(\eta)\frac{d\theta}{d\eta}+\varepsilon\frac{d\theta}{d\eta}\frac{d\theta}{d\eta}+P_rN_b\frac{d\theta}{d\eta}\frac{dq}{d\eta}$$
$$+P_rN_t\frac{d\theta}{d\eta}\frac{d\theta}{d\eta}+\frac{2}{m+1}\zeta P_re^{-n\eta}=0, \tag{20}$$

$$\frac{d^2q}{d\eta^2}+S_{cA}f(\eta)\frac{dq}{d\eta}-\frac{N_t}{N_b}\frac{d^2\theta}{d\eta^2}-\frac{2}{m+1}S_{cA}\mathcal{R}q(\eta)s^3(\eta)=0, \tag{21}$$

$$\gamma\frac{d^2s}{d\eta^2}+S_{cB}f(\eta)\frac{ds}{d\eta}+\frac{N_t}{N_b}\frac{d^2\theta}{d\eta^2}+\frac{2}{m+1}S_{cB}\mathcal{R}q(\eta)s^3(\eta)=0, \tag{22}$$

$$\frac{d^2\omega}{d\eta^2}-\frac{2}{m+1}S_{cm}\omega(\eta)\frac{df}{d\eta}-\frac{2}{m+1}S_{cm}S_g\frac{df}{d\eta}+S_{cm}f(\eta)\frac{d\omega}{d\eta}-P_e\omega\frac{d^2q}{d\eta^2}-P_e\frac{dq}{d\eta}\frac{d\omega}{d\eta}$$
$$-P_e\beth\frac{d^2q}{d\eta^2}-P_eS_g\frac{d^2q}{d\eta^2}=0. \tag{23}$$

It is important to note that at the surface $y=A(x+b)^{\frac{1-m}{2}}$, the minimum value of y which corresponds to minimum value of the similarity variable

$$\eta=\sqrt{\frac{U_o(m+1)}{2\vartheta}}=\Im. \tag{24}$$

Then the boundary conditions become

$$f(\Im)=\Im\frac{1-m}{1+m},\ \frac{df}{d\Im}=1,\ \theta(\Im)=1-S_t,\ \frac{1}{\mathcal{J}}\frac{dq}{d\Im}=q(\Im),$$
$$\frac{\gamma}{\mathcal{J}}\frac{ds}{d\Im}=-q(\Im),\ \omega(\Im)=1-S_g\quad at\ \Im=\eta, \tag{25}$$

$$\frac{df}{d\Im}\to 0,\ \theta(\Im)\to 0,\ q(\Im)\to 1,\ s(\Im)\to 0,\ \omega(\Im)\to 0\quad as\ \eta\to\Im. \tag{26}$$

The transformed governing equations (19)-(23) are dependent on η while the boundary conditions are dependent on $\Im$. It is therefore, necessary to change the domain from $[\Im,\infty]$ to $[0,\infty]$ which is done by defining $F(\aleph)=F(\eta-\Im)=f(\eta)$, $\Theta(\aleph)=\Theta(\eta-\Im)=\theta(\eta)$, $\mathrm{Q}(\aleph)=\mathrm{Q}(\eta-\Im)=q(\eta)$, $\mathrm{S}(\aleph)=\mathrm{S}(\eta-\Im)=s(\eta)$ and $\mathrm{W}(\aleph)=\mathrm{W}(\eta-\Im)=w(\eta)$. The dimensionless governing equations (19)-(23) take a new form

$$\left([1+(1-\Theta(\aleph))\xi]+\varsigma-\varsigma\mathcal{H}\frac{(m+1)}{2}\frac{d^2F}{d\aleph^2}\frac{d^2F}{d\aleph^2}\right)\frac{d^3F}{d\aleph^3}-\xi\frac{d^2F}{d\aleph^2}\frac{d\Theta}{d\aleph}$$
$$-\frac{2m}{m+1}\frac{dF}{d\aleph}\frac{dF}{d\aleph}+F(\aleph)\frac{d^2F}{d\aleph^2}-\frac{2}{m+1}M\frac{dF}{d\aleph}-\frac{2}{m+1}[1+(1-\Theta)\xi]P_s\frac{dF}{d\aleph} \tag{27}$$
$$-\frac{2}{m+1}F_sD_a^{-1}\frac{dF}{d\aleph}\frac{dF}{d\aleph}=0,$$

$$[1+\Theta(\aleph)\varepsilon]\frac{d^2\Theta}{d\aleph^2}-\frac{2}{m+1}P_r\Theta(\aleph)\frac{df}{d\aleph}-\frac{2}{m+1}S_tP_r\frac{dF}{d\aleph}+P_rF(\aleph)\frac{d\Theta}{d\aleph}$$
$$+\varepsilon\frac{d\Theta}{d\aleph}\frac{d\Theta}{d\aleph}+P_rN_b\frac{d\Theta}{d\aleph}\frac{dQ}{d\aleph}+P_rN_t\frac{d\Theta}{d\aleph}\frac{d\Theta}{d\aleph}+\frac{2}{m+1}\zeta P_re^{-n\eta}=0, \tag{28}$$

$$\frac{d^2Q}{d\aleph^2}+S_{cA}F(\aleph)\frac{dQ}{d\aleph}-\frac{N_t}{N_b}\frac{d^2\Theta}{d\aleph^2}-\frac{2}{m+1}S_{cA}\mathcal{R}Q(\aleph)S^3(\aleph)=0, \tag{29}$$

$$\gamma\frac{d^2S}{d\aleph^2}+S_{cB}F(\aleph)\frac{dS}{d\aleph}+\frac{N_t}{N_b}\frac{d^2\Theta}{d\aleph^2}+\frac{2}{m+1}S_{cB}\mathcal{R}q(\aleph)S^3(\aleph)=0, \tag{30}$$

$$\frac{d^2W}{d\eta^2}-\frac{2}{m+1}S_{cm}W(\aleph)\frac{dF}{d\aleph}-\frac{2}{m+1}S_{cm}S_g\frac{dF}{d\aleph}+S_{cm}F(\aleph)\frac{dW}{d\aleph}-P_eW\frac{d^2Q}{d\aleph^2}$$
$$-P_e\frac{dQ}{d\aleph}\frac{dW}{d\aleph}-P_e\beth\frac{d^2Q}{d\aleph^2}-P_eS_g\frac{d^2Q}{d\aleph^2}=0, \tag{31}$$

The boundary conditions become

$$F(\aleph)=\Im\frac{1-m}{1+m},\quad \frac{dF}{d\aleph}=1,\quad \Theta(\aleph)=1-S_t,\quad \frac{1}{\mathcal{J}}\frac{dQ}{d\aleph}=Q(\aleph)$$
$$\frac{\gamma}{\mathcal{J}}\frac{dS}{d\aleph}=-Q(\aleph),\qquad W(\aleph)=1-S_g\quad at\quad \aleph=0, \tag{32}$$

$$\frac{dF}{d\aleph}\to 0,\Theta(\aleph)\to 0,\ Q(\aleph)\to 1,\ S(\aleph)\to 0,\ W(\aleph)\to 0\quad as\quad \aleph\to\infty. \tag{33}$$

Through the usage of the similarity variables in Eqs. (17), Eqs. (18) can be non-dimensionalized to obtain

$$Re_x^{\frac{1}{2}}C_{f=}\left[[(1+(\xi-\xi\Theta))+\varsigma]\frac{d^2F}{d\aleph^2}-\xi\frac{dF}{d\aleph}\frac{d\Theta}{d\aleph}-\varsigma\mathcal{H}\frac{d^2F}{d\aleph^2}\frac{d^2F}{d\aleph^2}\frac{d^2F}{d\aleph^2}\right]_{\aleph=0},$$
$$Re_x^{-\frac{1}{2}}Nu_x=-\frac{\mathrm{d}\Theta}{d\aleph}\bigg|_{\aleph=0}, \tag{34}$$

where Re_x is the local Reynolds number.

Erying-Powell fluid parameters are $\varsigma=\frac{1}{\beta_jC\mu}$, $\mathcal{H}=\frac{U_0^3(x+b)^{3m-1}}{2C^2\vartheta}$, temperature-dependent viscous parameter $\xi=\varpi(T_w-T_0)$, magnetic parameter $\frac{\sigma{B_o}^2}{\rho U_0}(x+b)^{-m+1}$, temperature-dependent thermal conductivity parameter $\varepsilon=\delta(T_w-T_0)$, thermophoresis parameter $N_t=\frac{\tau(T_w-T_0)}{\alpha}\frac{D_T}{T_\infty}$, Brownian motion parameter $N_b=\frac{\tau D_A\delta}{\alpha}$, thermal stratification $S_t=\frac{m_2}{m_1}$, space-dependent internal heat source parameter $\zeta=\frac{Q_o}{\rho C_pc(x+b)^{m-1}}$, n is the intensity of internal heat generation parameter, Schmidt number for reactant A $S_{cA=}\frac{\vartheta}{D_A}$, Schmidt number for reactant B $S_{cB}=\frac{\vartheta}{D_B}$, homogeneous reaction parameter $\mathcal{R}=\frac{k_h\delta^3}{U_0(x+b)^{m-1}}$, Porosity parameter $P_s=\frac{\vartheta}{kU_o}(x+b)^{1-m}$, local Forchheimer pa-

rameter $F_s = \frac{b^*}{(x+b)}$, local Darcy parameter $D_a = \frac{k}{(x+b)^2}$, Gyrotactic microorganisms concentration difference parameter $\beth = \frac{N_o}{N_w - N_0}$, Schmidt number for diffusing motile microorganisms $S_{cm} = \frac{\vartheta}{D_n}$, Peclet number $P_e = \frac{bW_c}{\mathrm{D_n}\acute{\lambda}}$, gyrotactic microorganisms density stratification parameter $S_g = \frac{m_4}{m_3}$, heterogeneous reaction parameter $\mathcal{J} = \frac{k_s}{D_A\sqrt{\frac{U_0(m+1)}{2\vartheta}}\,(x+b)^{\frac{m-1}{2}}}$, ratio of diffusion coefficient $\gamma = \frac{D_A}{D_B}$.

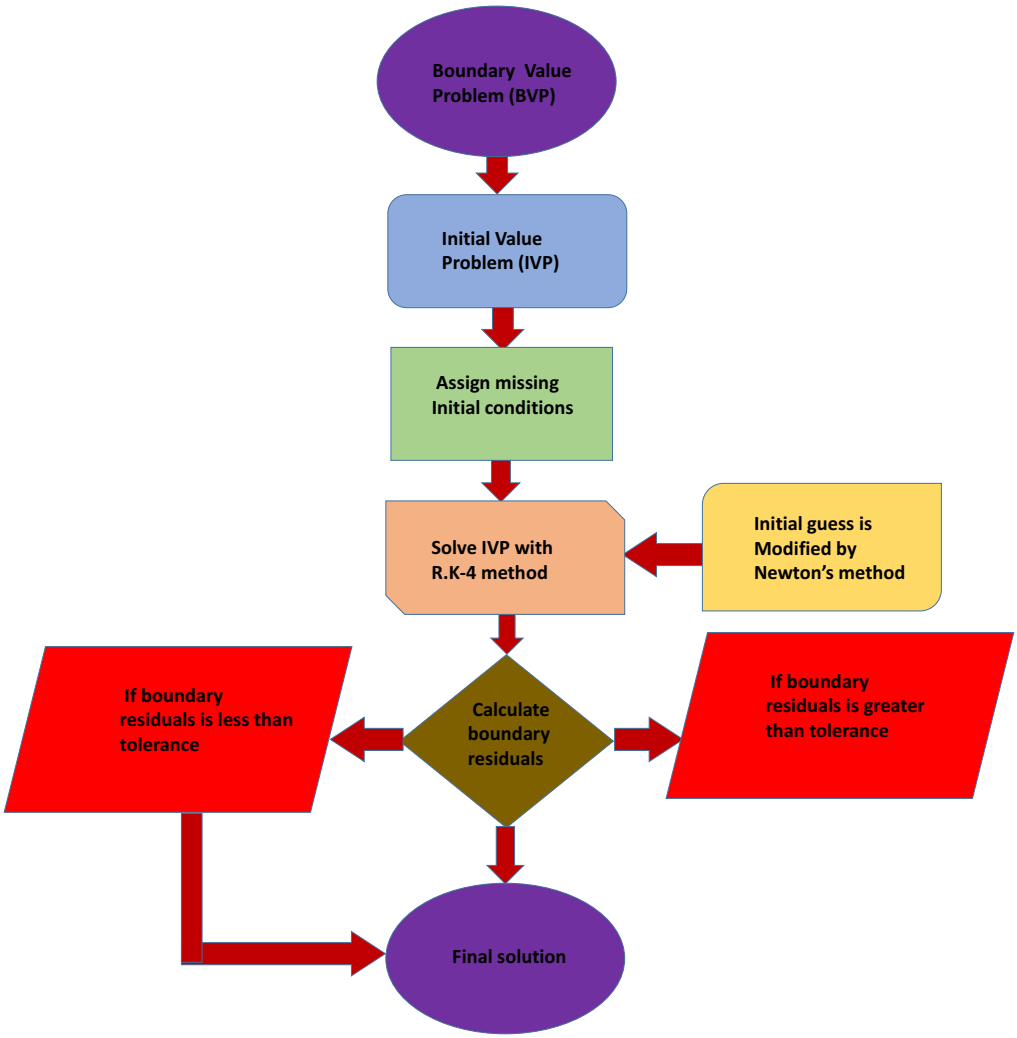

Figure 2. Flow chart of the problem

3 Numerical solution: procedure of the shooting technique

The procedure for obtaining the numerical solutions with the aid of $RK-4$ alongside with shooting technique is expressed in Fig. 2. To be able to carry out the operation of the shooting technique, the system of dimensionless Eqs. (27)-(31) is reduced to the following system of first-order ordinary differential equations;

$$F = y_1,$$

$$\frac{dF}{d\aleph} = y_2,$$

$$\frac{d^2F}{d\aleph^2} = y_3,$$

$$\frac{d^3f}{d\aleph^3} = y_3' = \frac{\xi y_3 y_5 + \frac{2m}{m+1} y_2 y_2 - y_1 y_3 + \frac{2}{m+1} M y_2 + \frac{2}{m+1} P_s \left[1 + \left(1 - y_4\right) \xi\right] y_2 + \frac{2}{m+1} F_s D_a^{-1} y_2 y_2}{\left(\left[1 + (1 - y_4)\, \xi\right] + \varsigma - \varsigma \mathcal{H} \frac{(m+1)}{2} y_3 y_3\right)},$$

$$\Theta = y_4,$$

$$\frac{d\Theta}{d\aleph} = y_5,$$

$$\frac{d^2\Theta}{d\aleph^2} = y_5' = \frac{\left(\frac{2}{m+1} P_r y_4 y_2 + \frac{2}{m+1} S_t P_r y_2 - P_r y_1 y_5 - \varepsilon y_5 y_5 - P_r N_b y_5 y_7 - P_r N_t y_5 y_5 - \frac{2}{m+1} \zeta P_r \mathrm{e}^{-n\aleph}\right)}{[1 + y_4 \varepsilon]}$$

$$Q = y_6,$$

$$\frac{dQ}{d\aleph} = y_7,$$

$$\begin{aligned}
&\frac{d^2Q}{d\aleph} = y_7' \\
&= \frac{N_t}{N_b} \left(\frac{\left(\frac{2}{m+1} P_r y_4 y_2 + \frac{2}{m+1} S_t P_r y_2 - P_r y_1 y_5 - \varepsilon y_5 y_5 - P_r N_b y_5 y_7 - P_r N_t y_5 y_5 - \frac{2}{m+1} \zeta P_r \mathrm{e}^{-n\aleph}\right)}{[1 + y_4 \varepsilon]} \right) \\
&- S_{cA} y_1 y_7 + \frac{2}{m+1} S_{cA} \mathcal{R} y_6 y_8 y_8 y_8,
\end{aligned}$$

$$S = y_8,$$

$$\frac{dS}{d\aleph} = y_9,$$

$$\frac{d^2S}{d\aleph} = y_9' = \frac{\left(\frac{N_t}{N_b} \frac{dy_5}{d\eta} - S_{cB} y_1 y_9 - \frac{2}{m+1} S_{cB} \mathcal{R} y_6 y_8 y_8 y_8\right)}{\gamma}$$

$$W = y_{10},$$

$$\frac{dW}{d\aleph} = y_{11},$$

$$\frac{d^2W}{d\aleph^2} = y'_{11} = \frac{2}{m+1}S_{cm}y_{10}y_2 + \frac{2}{m+1}S_{cm}S_g y_2 - S_{cm}y_1 y_{11} + \frac{dy_7}{d\eta}\left(P_e y_{10} + P_e S_g + P_e \beth\right) + P_e y_7 y_{11}, \tag{35}$$

Subject to boundary conditions:

$$y_1(0) = \Im\frac{1-m}{1+m}, \quad y_2(0) = 1, \quad y_4(0) = 1 - S_t,$$
$$\frac{1}{\mathcal{J}}y_7(0) = y_6(0), \quad \frac{\gamma}{\mathcal{J}}y_9(0) = -y_6(0), \quad y_{10}(0) = 1 - S_g \quad at\ \aleph = 0, \tag{36}$$

$$y_2(0) \to 0,\ y_4(0) \to 0, y_6(0) \to 1, y_8(0) \to 0,\ y_{10}(0) \to 0 \quad as\ \aleph \to \infty.$$

Initial approximations were selected and Eqs. (35) and (36) are integrated numerically as an initial value problem with the tolerance level of 10^{-6} and the boundary condition at a finite point considered as $\aleph = 6$.

4 Analysis of results and discussion

The values of pertinent parameters have been carefully selected during the process of computations as $\varsigma = \mathcal{H} = 0.1, m = 0.75,\ \Im = 0.25,\ S_t = S_g = 0.1, P_s = F_s = D_a = 0.3,\ P_r = 1.0,\ P_e = 1.0$ so as to be able to properly observe the impacts on fluid flow within the boundary layer. Table 1 depicts the numerical values of physical quantities of engineering interest expressed in Eq. (34). Likewise, Table 2 shows the validation of results with two different techniques. It is noticed that there is reasonable agreement with both *shooting technique* and *Bvp4c*. The effect of Darcy-Forchheimer

Table 1. Variation in local skin friction coefficients, local heat transfer rate with various parameters when $m = 0.25,\ \varsigma = \mathcal{H} = 0.1, \Im = 0.25,\ S_t = S_g = 0.1,\ P_e = 1.0,\ \zeta = 0.4,\ L_e = 0.1,\ \gamma = 1.0,\ \mathcal{R} = 0.2, \mathcal{J} = 0.1$

F_s	D_a	ξ	ε	M	P_r	N_t	N_b	$C_f Re_x^{1/2}$	$Nu_x\ Re_x^{-\frac{1}{2}}$
0.1	0.1	0.3	0.4	0.5	1.0	0.1	0.1	−3.68398	−0.335823
0.3								−4.89971	−0.060089
	0.4							−3.501747	−0.382399
	0.6							−3.30933	−0.433187
		0.4						−3.30171	−0.438490
		0.7						−3.280692	−0.454088
			0.5					−3.279882	−0.430422
			0.8					−3.278111	−0.374863
				0.6				−3.385541	−0.321764
				1.0				−3.785906	−0.143243
					1.2			−3.778422	−0.146725
					2.0			−3.754425	−0.187570
						0.3		−3.733414	−0.067809
						0.6		−3.686839	0.214499
							0.2	−3.714673	0.051744
							0.5	−3.778341	−0.298297

Table 2. Validation of results and variations in $Nu_x\ Re_x^{-\frac{1}{2}}$ when $m = 0.25,\ \varsigma = \mathcal{H} = 0.1, \mathfrak{I} = 0.25,\ S_t = S_g = 0.1,\ P_r = 2.0,\ P_e = 1.0,\ N_t = 0.1,$ $\xi = \varepsilon = 0.3,\ \zeta = 0.4,\ L_e = 0.1,\ \gamma = 1.0,\ \mathcal{R} = 0.2, \mathcal{J} = 0.1,\ P_s = F_s = D_a = 0.3$

M	$Nu_x\ Re_x^{-\frac{1}{2}}$ (Shooting Technique)	$Nu_x\ Re_x^{-\frac{1}{2}}$ (Bvp4c)
0.1	−1.097833	−1.097831
0.4	−0.732341	−0.732340
0.5	−0.399743	−0.399742
0.7	−0.102830	−0.102829

parameter $(F_s,\ D_a)$ is revealed in Figs. 3(a) and 3(b), it is revealed in Fig. 3(a) that incremental values of $F_s,\ D_a$ cause a slight decline in the velocity distribution while an enhancement is noticed in the temperature distribution in Fig. 3(b).

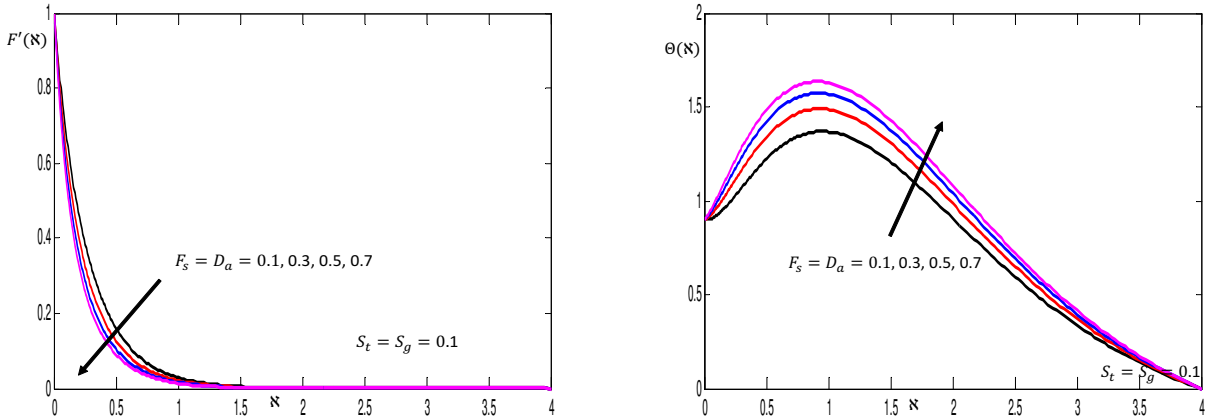

(a) **(b)**

Figure 3. The changes in the **(a)** contribution of F_s, D_a on velocity distribution and **(b)** contribution of F_s, D_a on temperature distribution

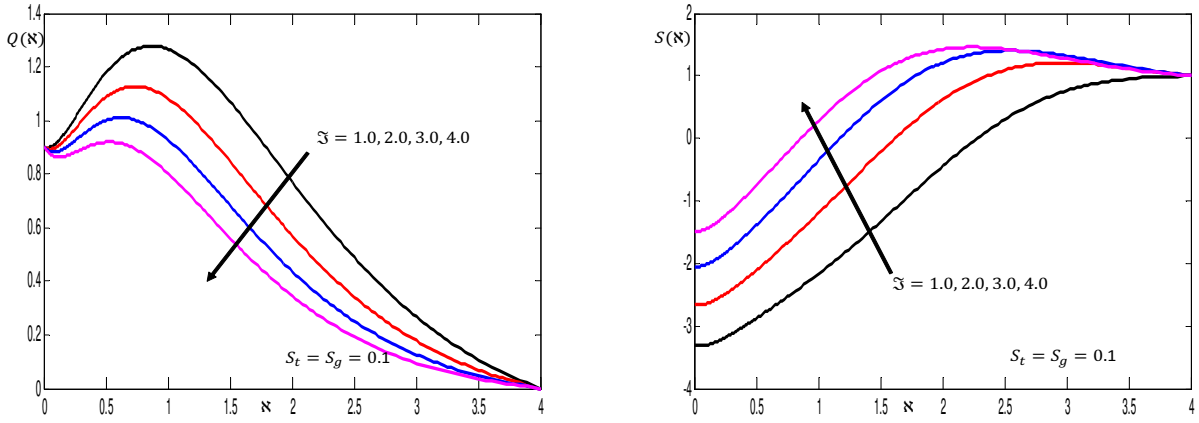

(a) **(b)**

Figure 4. The changes in the **(a)** contribution of $\mathfrak{I}$ on concentration distribution of homogeneous bulk fluid and **(b)** contribution of $\mathfrak{I}$ on concentration distribution of heterogeneous catalysts at the surface

It is observed in Fig. 4(a) that there is a diminution in the concentration distribution of homogeneous bulk fluid with increased thickness parameter $\Im$, while in Fig. 4(b) augmentation in the concentration distribution of heterogeneous catalyst at the surface is noticed as thickness parameter increases. In Figs. 5(a) and 5(b) incremental values of space-based internal heat generation parameter ζ correspond to augmentation of both the temperature distribution and concentration distribution of heterogeneous catalyst at the surface, respectively. Physically, this observation is due to the fact that there is a provision of sufficient heat energy required to break down the strong intermolecular bond binding the molecules of the particles of the fluid together which permits the free flow of the fluid over the upper horizontal surface of a paraboloid of revolution.

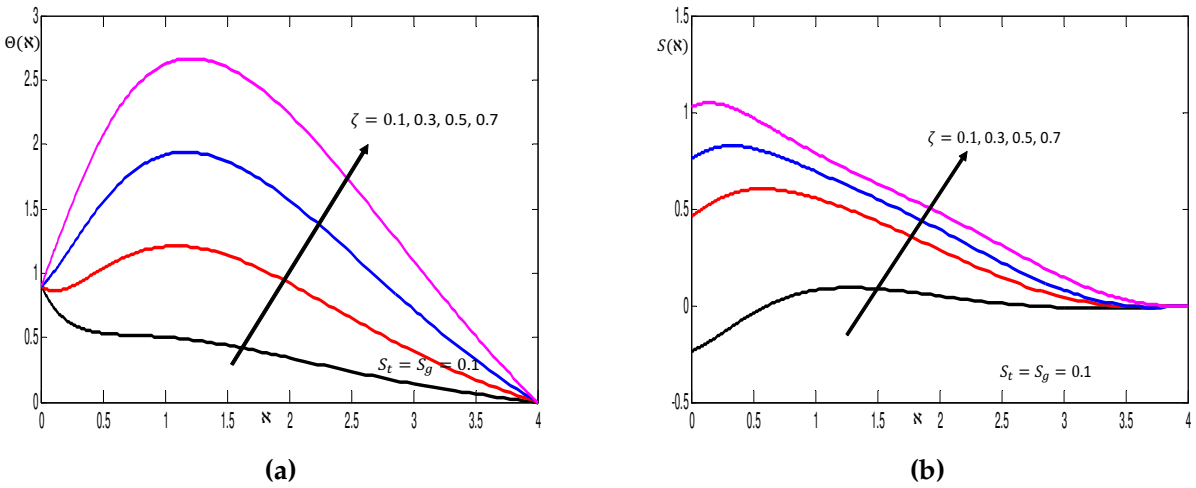

Figure 5. The changes in the **(a)** contribution of ζ on temperature distribution and **(b)** contribution of ζ on concentration distribution of heterogeneous catalysts at the surface

The impact of the thermal stratification parameter S_t is observed in Figs. 6(a),6(b),7(a). In Fig. 6(a), it is observed that incremental values of S_t lead to a diminution of the temperature distribution, while an enhancement in the concentration of reactant is noticed in Fig. 6(b).

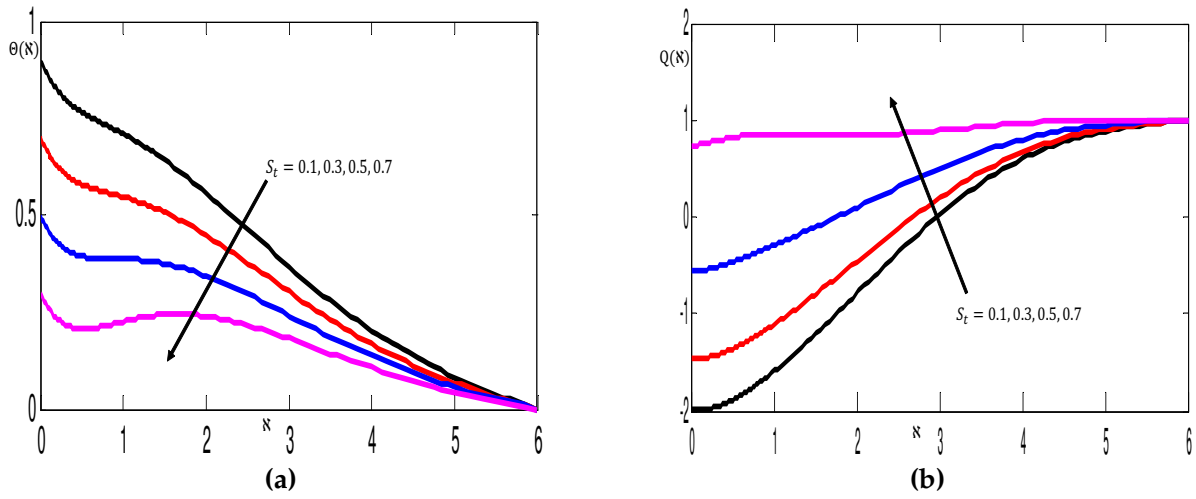

Figure 6. The changes in the **(a)** contribution of S_t on temperature distribution and **(b)** contribution of S_t on concentration distribution of homogeneous bulk fluid

It is visualized in Fig. 7(a) that increasing S_t corresponds to a decline in the bioconvection distribution, while a different behaviour is noticed in Fig. 7(b) in the sense that, as S_g is raised, the bioconvection distribution diminishes within the domain $0 \leq \aleph \leq 2.4$ and thereafter, an augmentation is noticed within the domain $2.4 \leq \aleph \leq 6.0$.

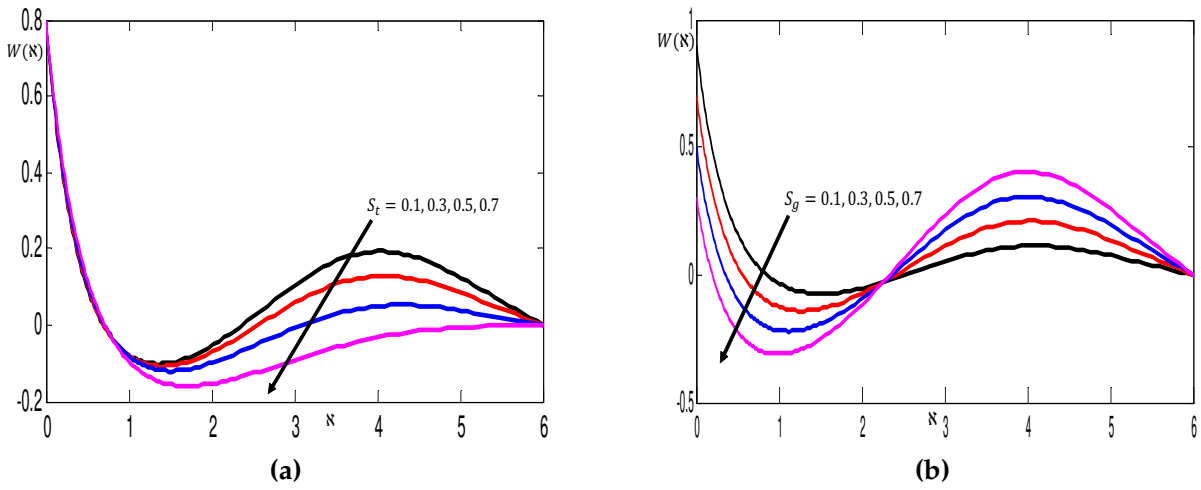

Figure 7. The changes in the **(a)** contribution of S_t bioconvection distribution and **(b)** contribution of S_g bioconvection distribution

The influence of material parameter ς is reflected in Figs. 8-10 when $S_t = S_g = 0.1$ (that is, at the hypolimnion layer of stratification). It is observed in Fig. 8(a) that the velocity of the fluid is enhanced as it flows over the upper horizontal surface of the paraboloid of revolution. The observed trend is due to the fact that $\varsigma = \frac{1}{\beta_j C\mu}$ means if ς increases, automatically the viscosity of the Erying-Powell fluid is subsided, thereby boosting the motion of the fluid across the upper horizontal surface of the paraboloid of revolution. An opposite effect is noticed in temperature distribution in Fig. 8(b) as ς increases.

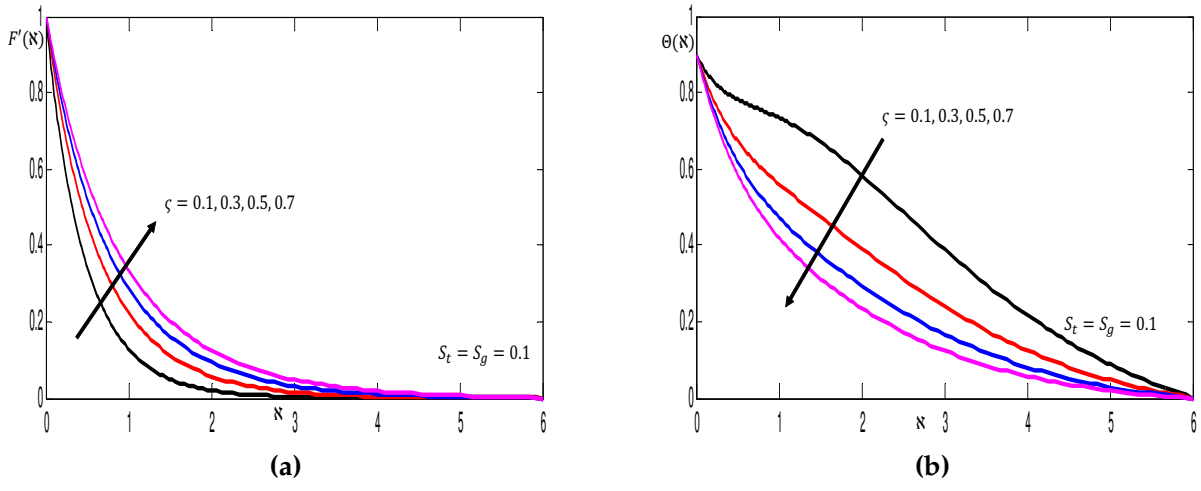

Figure 8. The changes in the **(a)** contribution of ς on velocity distribution and **(b)** contribution of ς on temperature distribution

Fig. 9(a) unravels the contribution of ς on the concentration of reactant A that is also known as the homogeneous bulk fluid. It is deduced that the magnitude of ς leads to a significant enhancement of the concentration of reactant A at the initial stage of the stratification, meanwhile, with the same magnitude of ς large diminution is noticed in the concentration of reactant B and bioconvection distribution.

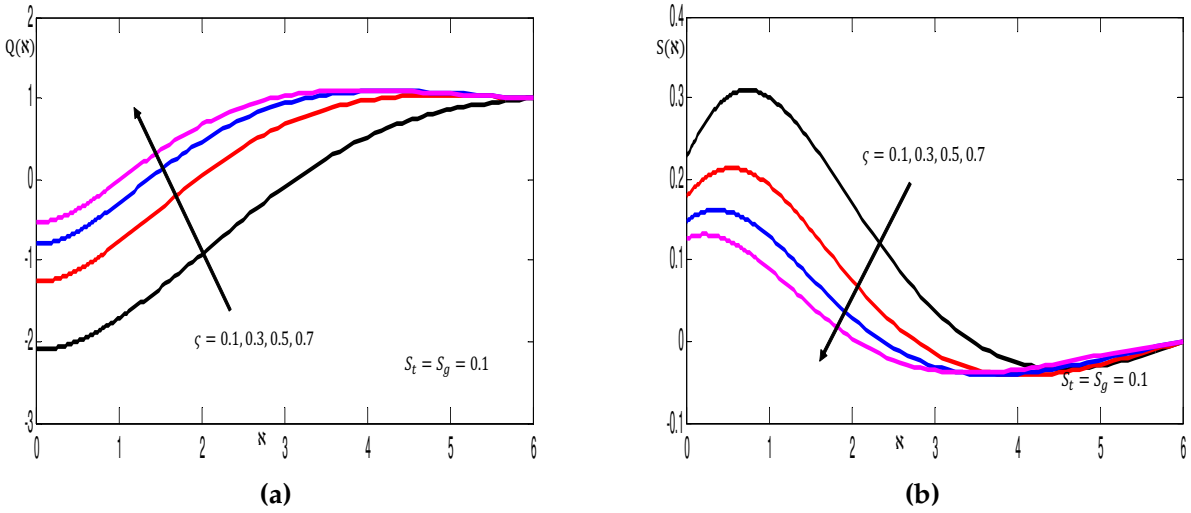

Figure 9. The changes in the **(a)** contribution of ς on concentration distribution of homogeneous bulk fluid and **(b)** contribution of ς on concentration distribution of heterogeneous catalyst at the surface

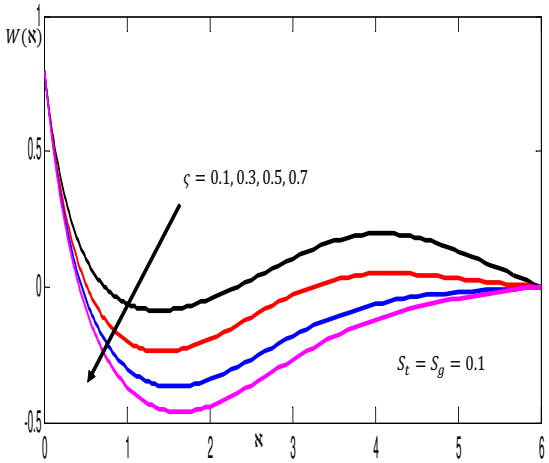

Figure 10. Contribution of ς on bioconvection distribution

The variations in profiles of concentration of reactant A and concentration of reactant B with increasing values of homogeneous reaction material $\mathcal{R}$ are computed in Figs. 11(a) and 11(b) when $S_t = S_g = 0.1$. It is discovered that an increase in the magnitude of $\mathcal{R}$ produces a significant increase in the concentration of reactant A and a slight elevation is deduced in the concentration of reactant B at the hypolimnion stratified layer of the upper horizontal surface of the paraboloid of revolution.

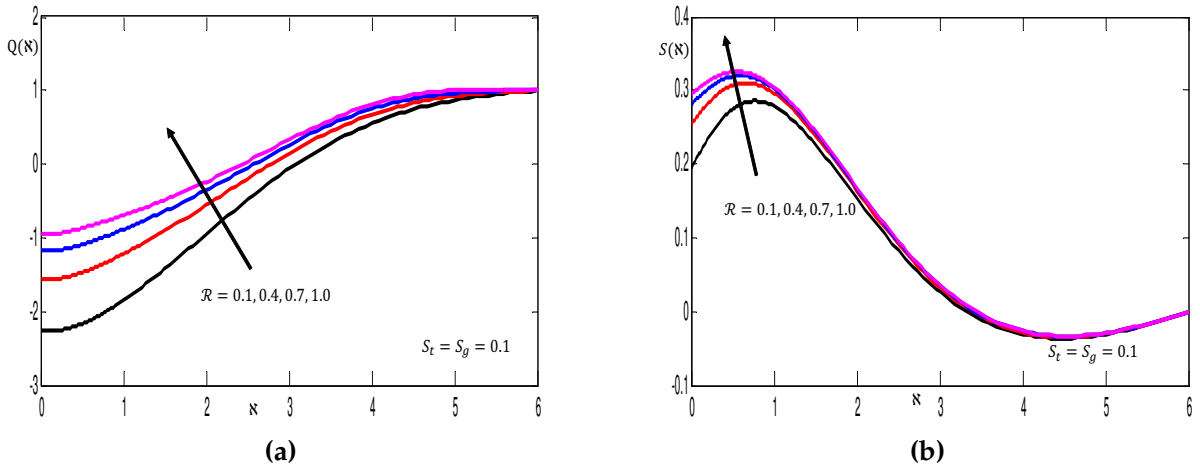

Figure 11. The changes in the **(a)** Contribution of $\mathcal{R}$ on concentration distribution of homogeneous bulk fluid and **(b)** contribution of $\mathcal{R}$ on concentration distribution of heterogeneous catalysts at the surface

Figs. 12(a) and 12(b) delineates impact of heterogeneous reaction parameter $\mathcal{J}$ on profiles of concentration of reactant A and concentration of reactant B when $S_t = S_g = 0.1$ and $\mathcal{R} = 1.0$. It is seen from the Fig. 12(a) that concentration of reactant A is an increasing function of $\mathcal{J}$ while in Fig. 12(b) it is noticed that the concentration of reactant B is a decreasing function of $\mathcal{J}$.

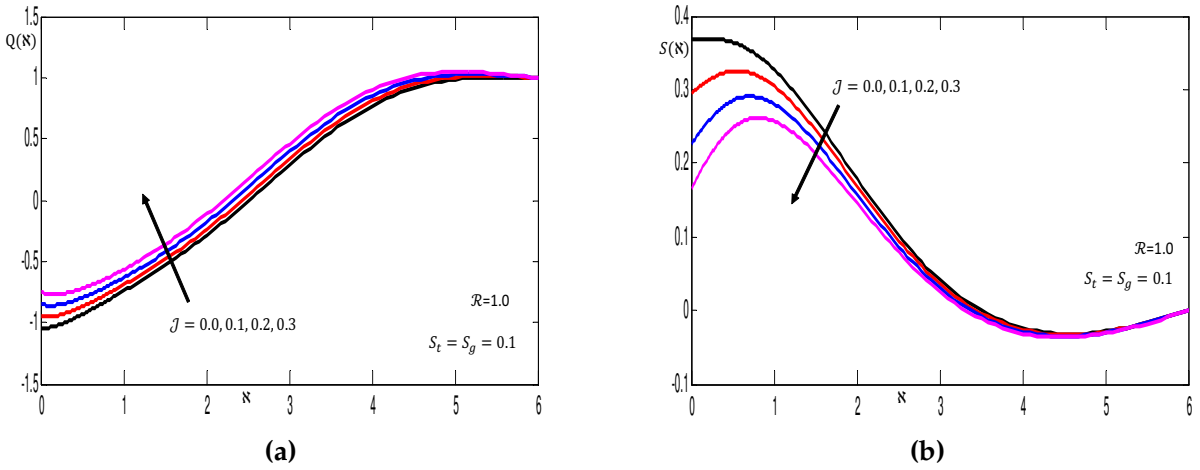

Figure 12. The changes in the **(a)** contribution of $\mathcal{J}$ on concentration distribution of homogeneous bulk fluid and **(b)** contribution of $\mathcal{J}$ on concentration distribution of heterogeneous catalysts at the surface

The impact of the bioconvection Schmidt number S_{cm} is plotted in Fig. 13 when $S_t = S_g = 0.1$ and $\beth = 2.0$. It is seen that the bioconvection distribution exhibits decelerating characteristics within the domain $0 \leq \aleph \leq 2.4$ and further shows a diminution within the domain $2.8 \leq \aleph \leq 6.0$ of the upper horizontal surface of a paraboloid of revolution when S_{cm} is raised. Physically, the observed development is attributable to the fact that the bioconvection Schmidt number S_{cm} corresponds to the ratio of momentum diffusivity to the diffusivity of microorganisms. It is worth noting that, raising S_{cm} correlates to a decrease in microorganisms' diffusion, which reduces both the density and the thickness of the boundary layer for motile microorganisms.

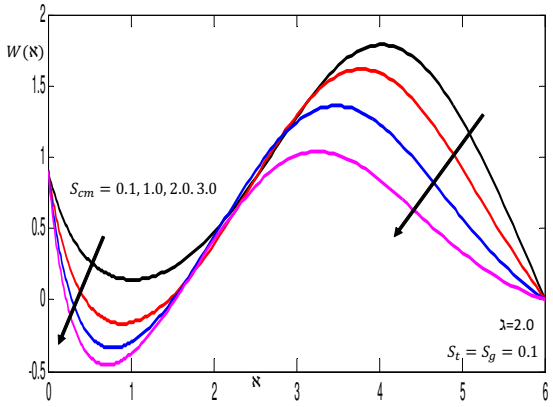

Figure 13. Contribution of S_{cm} on bioconvection distribution

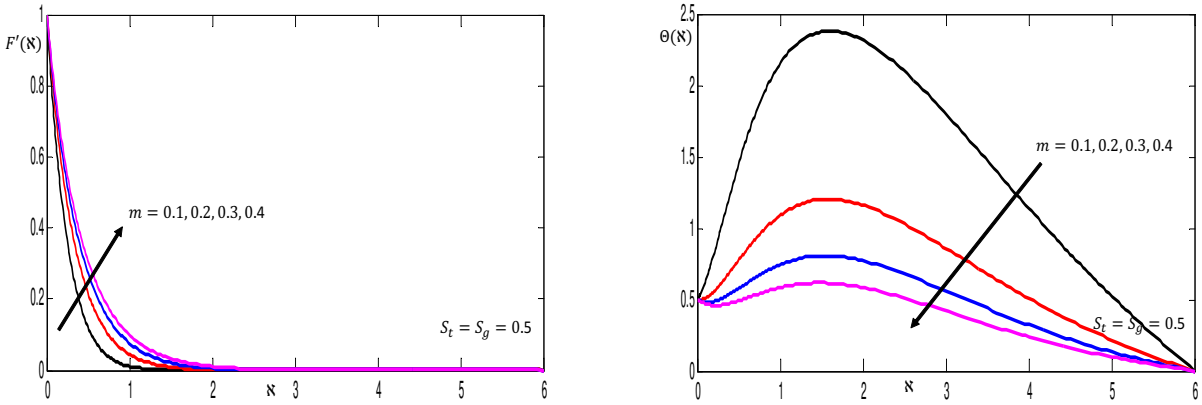

Figure 14. The changes in the **(a)** contribution of m on velocity distribution and **(b)** contribution of m on temperature distribution

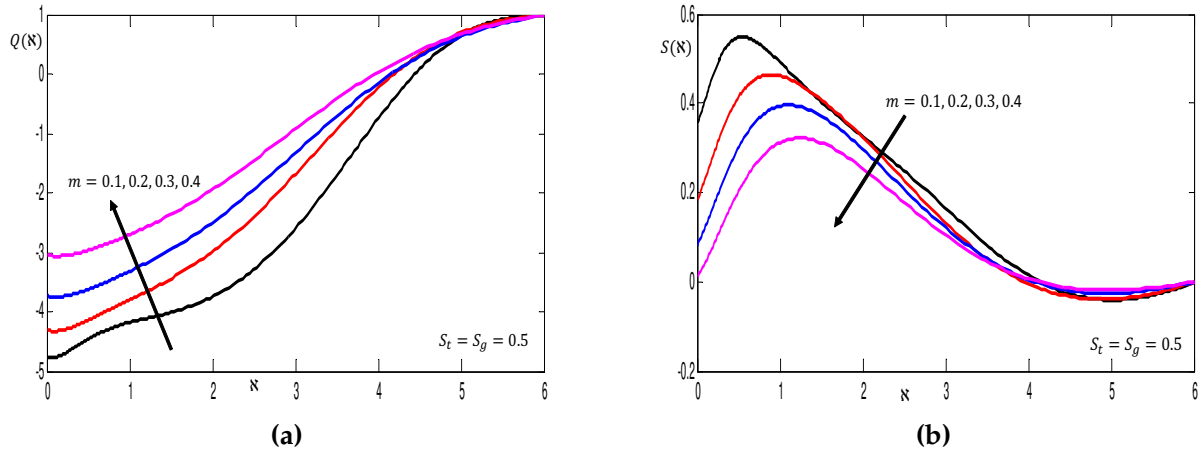

Figure 15. The changes in the **(a)** contribution of m on concentration distribution of homogeneous bulk fluid and **(b)** contribution of m on concentration distribution of heterogeneous catalysts at the surface

The effect of the velocity index parameter m is revealed in Figs. 14-15 when $S_t = S_g = 0.5$. It is noticed in Fig. 14(a) that incremental values of m lead to augmentation of the velocity distribution while a decline in the temperature distribution is noticed in Fig. 14(b). In Fig. 15(a)-15(b) it is obvious that the concentration of homogeneous (bulk fluid) and concentration of heterogeneous (catalyst at the surface) are increasing and decreasing functions of m respectively. Figs. 16(a)-17(a) are plotted to view the variations in the concentration of homogeneous (bulk fluid), concentration of heterogeneous (catalyst at the surface), and bioconvection distribution with rising values of thermophoretic parameter $N_t(N_t = 0.1,\ 0.2,\ 0.3,\ 0.4)$. In Fig. 16(a), it is envisioned that within the domain $0 \leq \aleph \leq 2.7$ a diminution is noticed in the concentration of homogeneous (bulk fluid) for larger values of N_t and thereafter an enhancement is observed for $2.8 \leq \aleph \leq 6.0$. While in Fig. 16(b) a quite different behaviour is envisioned in the aspect of concentration of homogenous catalyst at the surface in the sense that, as N_t is raised, there is a substantial enhancement within the domain $0 \leq \aleph \leq 2.7$ of the concentration of heterogeneous catalyst at the surface and decline is later noticed when $2.8 \leq \aleph \leq 6.0$. Physically, the apparent trend results from the abrupt movement of heated particles from a location of high heat energy to a region of low heat energy in thermophoresis. In reality, thermophoresis may be witnessed in a heated fluorescent bulb, where heated particles tend to move to a location with a lower temperature gradient. In Fig. 17(a) it is observed that incremental values of N_t lead to an enhancement of the bioconvection distribution. Figs. 17(b)-18 present the influence of Brownian motion parameter N_b on the concentration of homogeneous bulk fluid and concentration of heterogeneous catalyst at the surface, respectively. In Fig. 17(b) it is observed that there is an obvious augmentation in the concentration of homogeneous bulk fluid with an increment in $N_b(N_b = 0.1,\ 0.2,\ 0.3,\ 0.4)$. Physically, these characteristics result from the collision of particles caused by the random motion of nanoparticles within the wall of the upper horizontal surface of the paraboloid of rotation. As a result of this development, kinetic energy is converted into thermal energy, resulting in improved behavior of homogenous concentrations (bulk fluid). In Fig. 18, a decline effect is noticed in the concentration of heterogeneous catalyst at the surface when N_b is raised, thereafter within the domain $3.4 \leq \aleph \leq 6.0$ a slight augmentation is noticed towards the freestream.

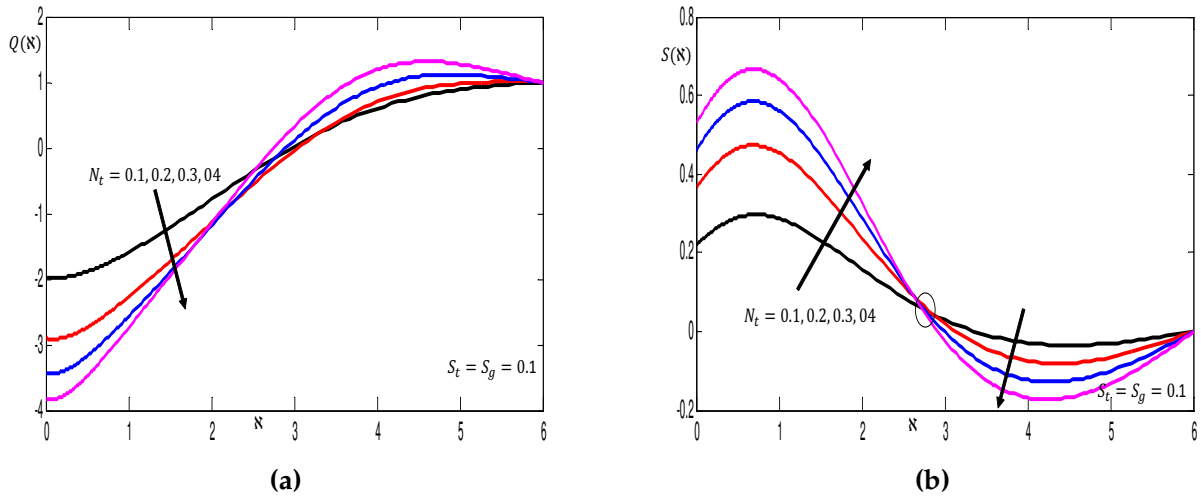

Figure 16. The changes in the **(a)** contribution of N_t on concentration distribution of homogeneous bulk fluid and **(b)** contribution of N_t on concentration distribution of heterogeneous catalysts at the surface

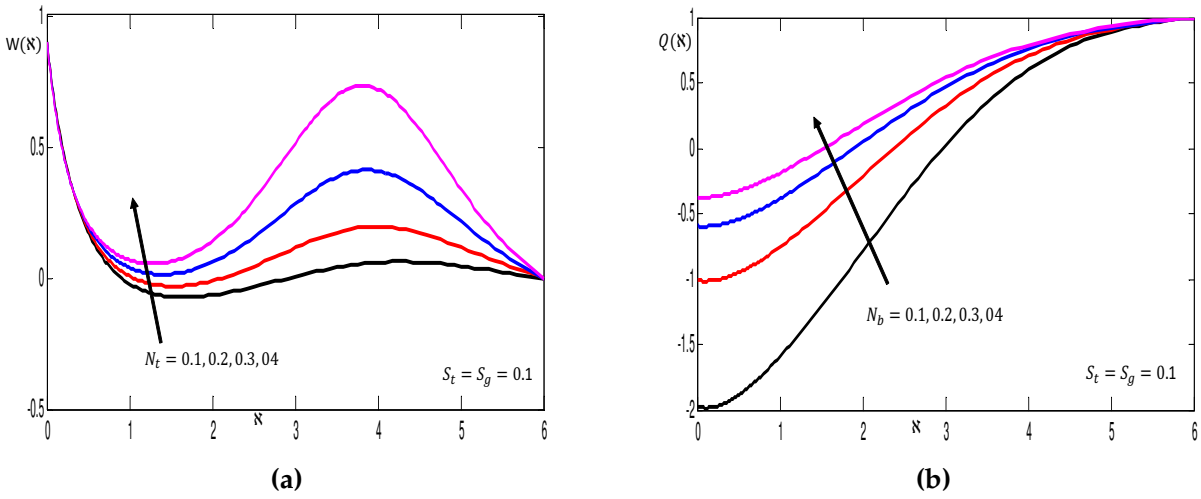

Figure 17. The changes in the **(a)** contribution of N_t on bioconvection distribution and **(b)** contribution of N_b on concentration distribution of homogeneous bulk fluid

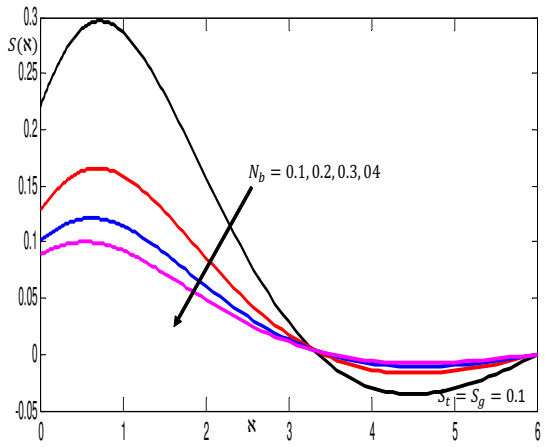

Figure 18. The changes in the contribution of N_b on concentration distribution of heterogeneous catalysts at the surface

Figs. 19-20 are prepared to demonstrate the significance of Prandtl number P_r when $S_t = S_g = 0.1$. In Fig. 19(a), increasing values of $P_r (P_r = 0.1,\ 0.7,\ 1.5,\ 2.0)$ cause the diminution of temperature distribution. It is physically justifiable since the Prandtl number represents the connection between a fluid's momentum transfer and thermal transport capacity.
In other words, Prandtl number $P_r = \frac{\vartheta}{\alpha} = \frac{\frac{\mu}{\rho}}{\frac{k}{\rho C_p}}$ reveals the relationship between kinematic viscosity and thermal diffusivity of the fluid. Therefore as P_r increases the viscosity of the Erying-Powel fluid magnifies leading to declining in the temperature of the fluid as it flows along the upper horizontal surface of a paraboloid of revolution. The impact of P_r on $Q(ℵ)$ is manifested in Fig. 19(b). It is observed that an increment in P_r corresponds to the decline in the concentration of homogeneous bulk fluid. In Fig. 20(a), an increase in P_r leads to the enhancement of the concentration of heterogeneous catalyst at the surface. Likewise, from Fig. 20(b) it is observed that the concentration of bioconvection lifts up as P_r is raised.

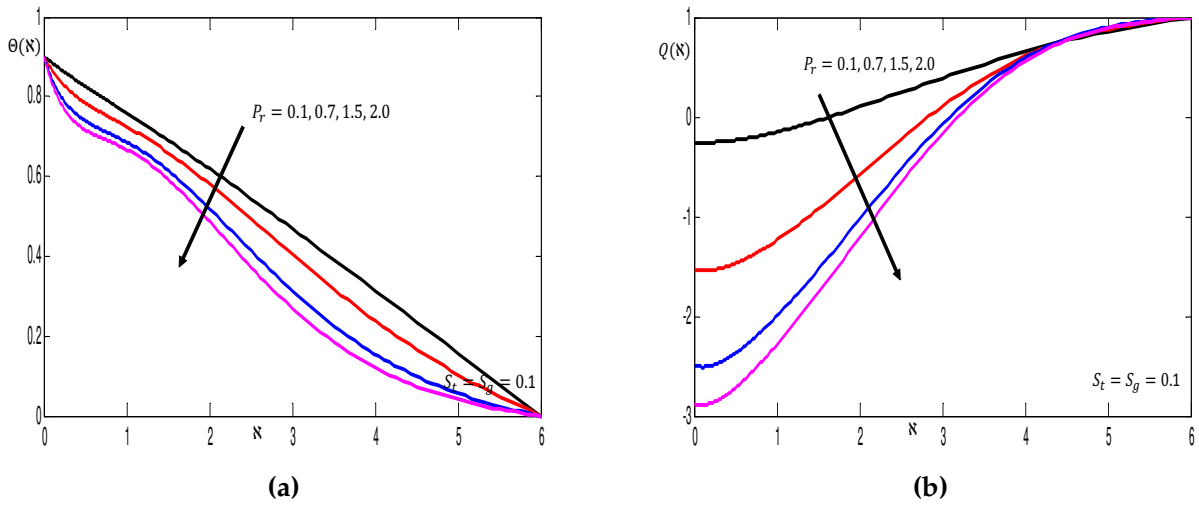

Figure 19. The changes in the **(a)** contribution of P_r on temperature distribution and **(b)** contribution of P_r on concentration distribution of homogeneous bulk fluid

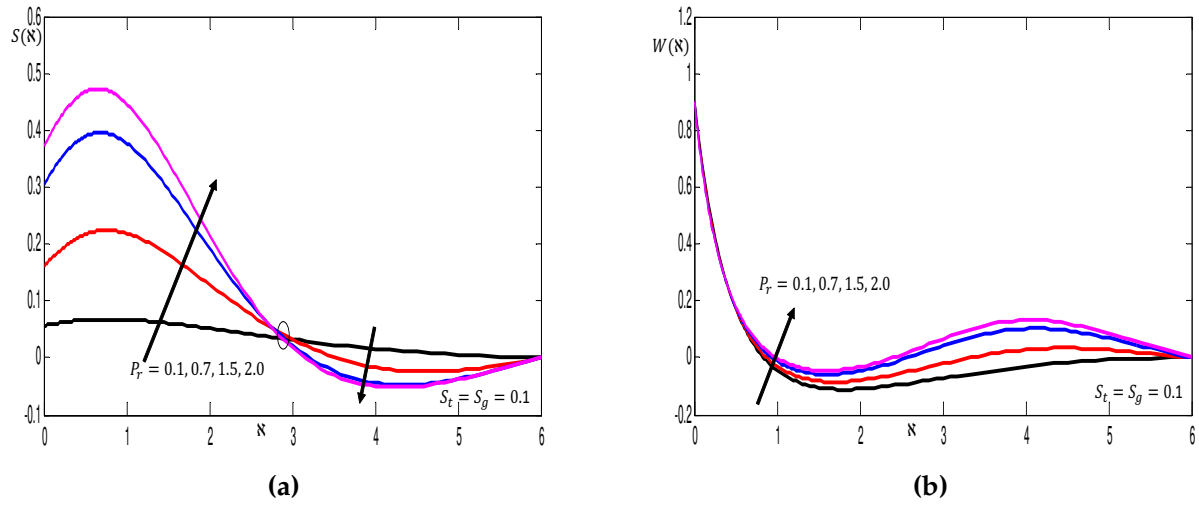

Figure 20. The changes in the **(a)** contribution of P_r on concentration distribution of heterogeneous catalysts at the surface and **(b)** contribution of P_r on bioconvection distribution

Figs. 21(a)-21(b) demonstrate the behavior of temperature-dependent viscous parameter ξ and temperature-dependent thermal conductivity parameter on velocity and temperature distributions, respectively. In Fig. 21(a), it revealed that the velocity distribution is enhanced with higher ξ, likewise with elevation in ε as seen in Fig. 21(b), there is a well-pronounced augmentation in the temperature distribution. Physically, this observation is a result of the fact that increasing thermal conductivity causes the kinetic energy of the fluid particles to increase, thus enhancing the temperature of the fluid. Figs. 22(a) and 22(b) present the effect of Prandtl number P_r on skin friction coefficient $Cf_x(Re_x)^{\frac{1}{2}}$ and Nusselt number $Nu_x(Re_x)^{-\frac{1}{2}}$, respectively. It is envisioned that both $Cf_x(Re_x)^{\frac{1}{2}}$ and $Nu_x(Re_x)^{-\frac{1}{2}}$ encumber with increasing P_r.

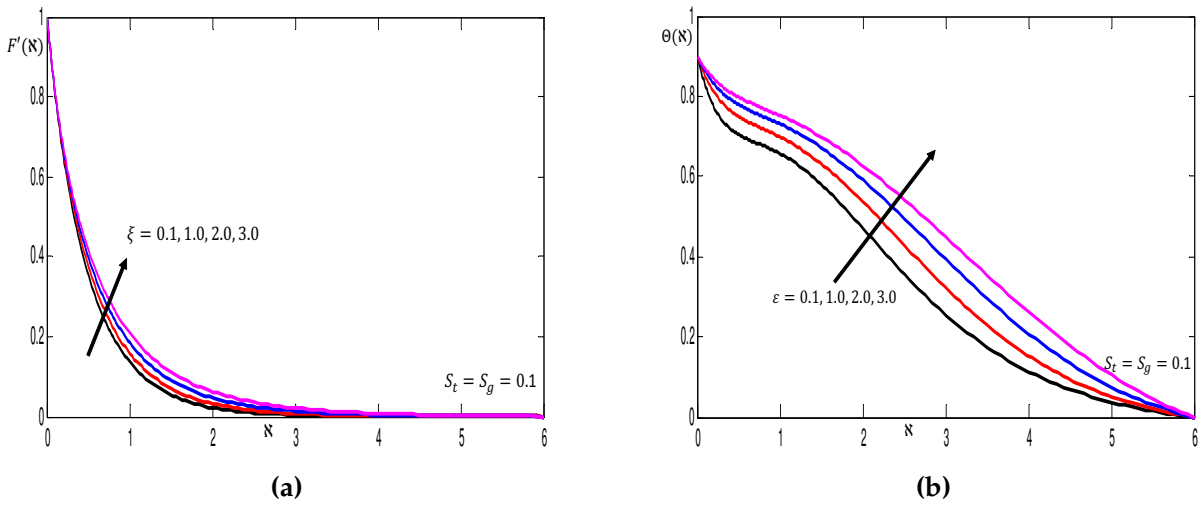

Figure 21. **(a)** Contribution of ξ on velocity distribution and **(b)** contribution of ε on temperature distribution

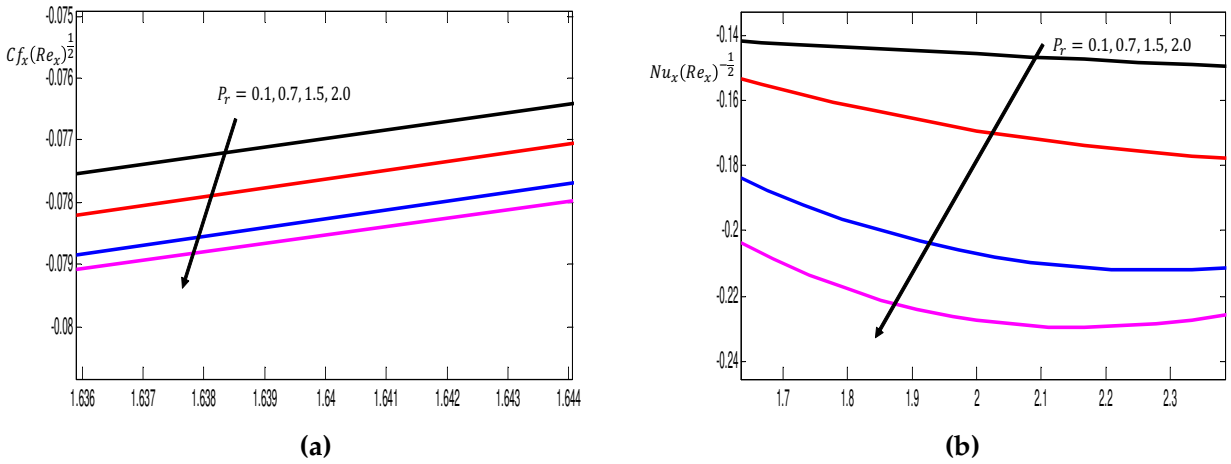

Figure 22. The changes in the **(a)** contribution of P_r on on coefficient of skin friction and **(b)** contribution of P_r on Nusselt number

5 Conclusions

The use of catalytic reactions in industry and real-life applications offers numerous economic advantages which include improved process efficiency, reduced energy consumption, and reduced waste production making it a critical tool for achieving sustainable and cost-effective chemical production. The motion of air across the pointed surface of an aircraft or over the bonnet of a car is highly important to scientists. Geometrically, the motion of fluid over this particular domain is termed the upper horizontal surface of a paraboloid of revolution. Simulation has been carried out for the boundary layer flow of Erying-Powell fluid transporting nanoparticles in the presence of stratifications and varying fluid characteristics across a surface with variable thickness. Thermal stratification, microorganisms stratification, and variable fluid properties have been appropriately modeled. When material parameters are increased, it is concluded that the viscosity of fluid subsides at the lowest layer of stratification, and the motion of Erying-

Powel increases across the upper horizontal surface of the paraboloid of revolution. Increasing the magnitude of Darcy-Forchheimer parameters corresponds to the diminution of velocity distribution and augmentation of temperature distribution. An improvement in bioconvection distribution is shown as the thermophoretic parameter is elevated. With increasing Brownian motion parameters, the homogeneous bulk fluid displays substantial augmentation. When the temperature-dependent viscosity parameter and temperature-dependent thermal conductivity parameter are raised, the fluid's velocity and temperature are increased. Significant enhancement is noticed in both temperature distribution and concentration distribution of heterogeneous catalysts at the surface when heat generation is increased. It is therefore significant to state that the major influence of these germane parameters would go a long way towards assisting scientists in reaching efficiency in the course of production in industries.

The present work can be extended to hybrid nanofluids. The combined effect of nonlinear thermal radiation and stratification can be properly incorporated which has many applications in the industry.

Declarations

Ethical approval

Not applicable.

Consent for publication

Not applicable.

Conflicts of interest

The authors declare that they have no conflict of interest.

Author's contributions

A.O.P.: Conceptualization, Supervision, Project Administration. T.O.: Formal Analysis, Investigation, Data Curation, Writing-Original Draft, Writing-Review & Editing. N.A.S.: Conceptualization, Formal Analysis, Resources, Visualization, Acquisition. E.O.: Methodology, Writing-Original Draft, Validation Project Administration, M.M.A.: Software, Validation, Data Curation, Writing-Review & Editing. All authors discussed the results and contributed to the final manuscript.

Acknowledgements

Not applicable.

References

[1] Shamshuddin, M.D., Shahzad, F., Jamshed, W., Bég, O.A., Eid, M.R. and Bég, T.A. Thermo-solutal stratification and chemical reaction effects on radiative magnetized nanofluid flow along an exponentially stretching sensor plate: Computational analysis. *Journal of Magnetism and Magnetic Materials*, 565, 170286, (2023). [CrossRef]

[2] Tamilzharasan, B.M., Karthikeyan, S., Kaabar, M.K., Yavuz, M. and Özköse, F. Magneto mixed convection of Williamson nanofluid flow through a double stratified porous medium in attendance of activation energy. *Mathematical and Computational Applications*, 27(3), 46, (2022). [CrossRef]

[3] Jagan, K. and Sivasankaran, S. Soret & Dufour and Triple stratification effect on MHD flow

with velocity slip towards a stretching cylinder. *Mathematical and Computational Applications*, 27(2), 25, (2022). [CrossRef]

[4] Rehman, S., Anjum, A., Farooq, M., Hashim and Malik, M.Y. Melting heat phenomenon in thermally stratified fluid reservoirs (Powell-Eyring fluid) with joule heating. *International Communications in Heat and Mass Transfer,* 137, 106196, (2022). [CrossRef]

[5] Oreyeni, T., Ramesh, K., Nayak, M.K. and Oladele, P.A. Triple stratification impacts on an inclined hydromagnetic bioconvective flow of micropolar nanofluid with exponential space-based heat generation. *Waves in Random and Complex Media*. [CrossRef]

[6] Fayz-Al-Asad, M., Oreyeni, T., Yavuz, M. and Olanrewaju, P.O. Analytic simulation of MHD boundary layer flow of a chemically reacting upper-convected Maxwell fluid past a vertical surface subjected to double stratifications with variable properties. *The European Physical Journal Plus,* 137, 813, (2022). [CrossRef]

[7] Khan, W.A., Anjum, N., Waqas, M., Abbas, S.Z., Irfan, M. and Muhammad, T. Impact of stratification phenomena on a nonlinear radiative flow of sutterby nanofluid. *Journal of Materials Research and Technology,* 15, 306-314, (2021). [CrossRef]

[8] Chen, S.B., Shahmir, N., Ramzan, M., Sun, Y.L., Aly, A.A. and Malik, M.Y. Thermophoretic particle deposition in the flow of dual stratified Casson fluid with magnetic dipole and generalized Fourier's and Fick's laws. *Case Studies in Thermal Engineering*, 26, 101186, (2021). [CrossRef]

[9] Dawar, A., Shah, Z., Alshehri, H. M., Islam, S. and Kumam, P. Magnetized and non-magnetized Casson fluid flow with gyrotactic microorganisms over a stratified stretching cylinder. *Scientific Reports*, 11, 16376, (2021). [CrossRef]

[10] Verma, A.K., Bhattacharyya, K., Rajput, S., Mandal, M.S., Chamkha, A.J. and Yadav, D. Buoyancy driven non-Newtonian Prandtl-Eyring nanofluid flow in Darcy-Forchheimer porous medium over inclined non-linear expanding sheet with double stratification. *Waves in Random and Complex Media*, (2022). [CrossRef]

[11] Mahmood, Z., Alhazmi, S.E., Alhowaity, A., Marzouki, R., Al-Ansari, N. and Khan, U. MHD mixed convective stagnation point flow of nanofluid past a permeable stretching sheet with nanoparticles aggregation and thermal stratification. *Scientific Reports,* 12, 16020, (2022). [CrossRef]

[12] Koriko, O.K., Shah, N.A., Saleem, S., Chung, J.D., Omowaye, A.J. and Oreyeni, T. Exploration of bioconvection flow of MHD thixotropic nanofluid past a vertical surface coexisting with both nanoparticles and gyrotactic microorganisms. *Scientific Reports,* 11, 16627, (2021). [CrossRef]

[13] Shah, N.A., Tosin, O., Shah, R., Salah, B. and Chung, J.D. Brownian motion and thermophoretic diffusion effects on the dynamics of MHD upper convected Maxwell nanofluid flow past a vertical surface. *Physica Scripta,* 96(12), 125722, (2021). [CrossRef]

[14] Nadeem, S., Fuzhang, W., Alharbi, F.M., Sajid, F., Abbas, N., El-Shafay, A.S. and Al-Mubaddel, F.S. Numerical computations for Buongiorno nano fluid model on the boundary layer flow of viscoelastic fluid towards a nonlinear stretching sheet. *Alexandria Engineering Journal,* 61(2), 1769-1778, (2022). [CrossRef]

[15] Rao, A.S., Ramaiah, K.D., Kotha, G., Rao, M.V.S. and Chamkha, A.J. A Spectral Relaxation approach for boundary layer flow of nanofluid past an exponentially stretching surface with variable suction in the presence of heat source/sink with viscous dissipation. *Arabian Journal*

for Science and Engineering, 46, 7509-7520, (2021). [CrossRef]

[16] Ur Rasheed, H., AL-Zubaidi, A., Islam, S., Saleem, S., Khan, Z. and Khan, W. Effects of Joule heating and viscous dissipation on magnetohydrodynamic boundary layer flow of Jeffrey nanofluid over a vertically stretching cylinder. *Coatings*, 11(3), 353, (2021). [CrossRef]

[17] Abbas, Z., Abdal, S., Hussain, N., Hussain, F., Adnan, M., Ali, B., ... & Younas, S. (2019). Mhd boundary layer flow and heat transfer of nanofluid over a vertical stretching sheet in the presence of a heat source. *Scientific Inquiry and Review*, 3(4), 60-73, (2019). [CrossRef]

[18] Rasool, G., Shafiq, A. and Durur, H. Darcy-Forchheimer relation in magnetohydrodynamic Jeffrey nanofluid flow over stretching surface. *Discrete & Continuous Dynamical Systems Series S*, 14(7), 2497-2515, (2021). [CrossRef]

[19] Kebede, T., Haile, E., Awgichew, G. and Walelign, T. Heat and mass transfer in unsteady boundary layer flow of Williamson nanofluids. *Journal of Applied Mathematics*, 1890972, (2020). [CrossRef]

[20] Swain, K., Mahanthesh, B. and Mebarek-Oudina, F. Heat transport and stagnation-point flow of magnetized nanoliquid with variable thermal conductivity, Brownian moment, and thermophoresis aspects. *Heat Transfer*, 50(1), 754-767, (2021). [CrossRef]

[21] Qureshi, M.A. Numerical simulation of heat transfer flow subject to MHD of Williamson nanofluid with thermal radiation. *Symmetry*, 13(1), 10, (2021). [CrossRef]

[22] Sravanthi, C.S., Mabood, F., Nabi, S. G. and Shehzad, S.A. Heterogeneous and homogeneous reactive flow of magnetite-water nanofluid over a magnetized moving plate. *Propulsion and Power Research*, 11(2), 265-275, (2022). [CrossRef]

[23] Alzahrani, F., Growda, R.J.P., Kumar, R.N. and Khan, M.I. Dynamics of thermosolutal Marangoni convection and nanoparticle aggregation effects on Oldroyd-B nanofluid past a porous boundary with homogeneous-heterogeneous catalytic reactions. *Journal of the Indian Chemical Society*, 99(6), 100458, (2022). [CrossRef]

[24] Sarojamma, G., Lakshmi, R.V., Narayana, P.V.S. and Animasaun, I.L. Exploration of the significance of autocatalytic chemical reaction and Cattaneo-Christov heat flux on the dynamics of a micropolar fluid. *Journal of Applied and Computational Mechanics*, 6(1), 77-89, (2020). [CrossRef]

[25] Animasaun, I.L., Mahanthesh, B., Sarojamma, G. and Damisa, J.S. Significance of thickness of paraboloid of revolution and buoyancy forces on the dynamics of Erying-Powel fluid subject to equal diffusivity kind of quartic autocatalysis. *Physica A: Statistical Mechanics and its Applications*, 549, 124047, (2020). [CrossRef]

[26] Hayat, T., Hussain, Z., Muhammad, T. and Alsaedi, A. Effects of homogeneous and heterogeneous reactions in flow of nanofluids over a nonlinear stretching surface with variable surface thickness. *Journal of Molecular Liquids*, 221, 1121-1127, (2016). [CrossRef]

[27] Zhao, Q., Xu, H. and Tao, L. Homogeneous-heterogeneous reactions in boundary-layer flow of a nanofluid near the forward stagnation point of a cylinder. *Journal of Heat Transfer*, 139(3), 034502, (2016). [CrossRef]

[28] Platt, J.R. Bioconvection patterns in cultures of free-swimming organisms. *Science*, 133(3466), 1766-1767, (1961). [CrossRef]

[29] Ramzan, M., Shamshad, U., Rehman, S., Saeed, A., Kumam, P. and Watthayu, W. Compuation of MHD flow of three-dimensional mixed convection non-Newtonian viscoelastic fluid with the physical aspect of gyrotactic microorganism. *Waves in Random and Complex Media*, 1-23, (2022). [CrossRef]

[30] Zhang, L., Puneeth, V., Ijaz Khan, M., El-Zahar, E.R., Manjunath, N., Shah, N.A., Chung, J.D., Khan, S.U. and Khan, M.I. Applications of bioconvection for tiny particles due to two concentric cylinders when role of Lorentz force is significant. *Plos One,* 17(5), e0265026, (2022). [CrossRef]

[31] Rao, M.V.S., Gangadhar, K., Chamkha, A.J. and Surekha, P. Bioconvection in a convectional nanofluid flow containing gyrotactic microorganisms over an isothermal vertical cone embedded in a porous surface with chemical reactive species. *Arabian Journal for Science and Engineering,* 46, 2493-2503, (2021). [CrossRef]

[32] Sankad, G., Ishwar, M. and Dhange, M. Varying wall temperature and thermal radiation effects on MHD boundary layer liquid flow containing gyrotactic microorganisms. *Partial Differential Equations in Applied Mathematics,* 4, 100092, (2021). [CrossRef]

[33] Parveen, N., Awais, M., Awan, S.E., Shah, S.A., Yuan, A., Nawaz, M., Akhtar, R. and Malik, M.Y. Thermophysical properties of chemotactic microorganisms in bio-convective peristaltic rheology of nano-liquid with slippage, Joule heating and viscous dissipation. *Cases in Thermal Engineering,* 27, 101285, (2021). [CrossRef]

[34] Naganthran, K., Md Basir, M.F., Thumma, T., Ige, E.O., Nazar, R. and Tlili, I. Scaling group analysis of bioconvective micropolar fluid flow and heat transfer in a porous medium. *Journal of Thermal Analysis and Calorimetry,* 143, 1943-1955, (2021). [CrossRef]

[35] Ramzan, M., Bilal, M., Kanwal, S. and Chung, J.D. Effects of variable thermal conductivity and non-linear thermal radiation past an Eyring Powell nanofluid with chemical reaction. *Communications in Theoretical Physics,* 67(6), 723-731, (2017). [CrossRef]

[36] Hayat, T., Iqbal, Z., Qasim, M. and Alsaedi, A. Flow of an Eyring-Powell fluid with convective boundary conditions. *Journal of Mechanics,* 29(2), 217-224, (2013). [CrossRef]

[37] Animasaun, L. and Koriko, O.K. New similarity solution of micropolar fluid flow problem over an UHSPR in the presence of quartic kind of autocatalytic chemical reaction. *Frontiers in Heat and Mass Transfer,* 8(26), (2017). [CrossRef]

[38] Kuznetsov, A.V. and Nield, D.A. Double-diffusive natural convective boundary layer flow of a nanofluid past a vertical plate. *International Journal of Thermal Sciences,* 50(5), 712-717, (2011). [CrossRef]

[39] Raees, A., Xu, H., Sun, Q. and Pop, I. Mixed convection in gravity-driven nanoliquid film containing both nanoparticles and gyrotactic microorganisms. *Applied Mathematics and Mechanics,* 36(2), 163-178, (2015). [CrossRef]

[40] Chaudhary, M.A. and Merkin, J.H. A simple isothermal model for homogeneous-heterogeneous reaction in boundary-layer flow. I Equal diffusivities. *Fluid Dynamics Research,* 16(6), 311-333, (1995). [CrossRef]

[41] Koriko, O.K., Omowaye, A.J., Sandeep, N. and Animasaun, I.L. Analysis of boundary layer formed on an upper horizontal surface of a paraboloid of revolution within nanofluid flow in the presence of thermophoresis and Brownian motion of 29 nm CuO. *International Journal of Mechanical Sciences,* 124-125, 22-36, (2017). [CrossRef]

[42] Kuznetsov, A.V. The onset of nanofluid bioconvection in a suspension containing both nanoparticles and gyrotactic microorganisms. *International Communications in Heat and Mass Transfer,* 37(10), 1421-1425, (2010).[CrossRef]

[43] Batchelor, G.K. *An Introduction to Fluid Dynamics*. Cambridge University Press: London, (1987).

[44] Charraudeau, J. Influence de gradients de proprietes physiques en convection forcee-application au cas du tube. *International Journal of Heat and Mass Transfer,* 18(1), 87-95, (1975). [CrossRef]

[45] Oreyeni, T., Shah, N.A., Popoola, A.O., Elzahar, E.R. and Yook, S.J. The significance of exponential space-based heat generation and variable thermophysical properties on the dynamics of Casson fluid over a stratified surface with non-uniform thickness. *Waves in Random and Complex Media*, (2022). [CrossRef]

[46] Oreyeni, T. and Omokhuale, E. Optimal homotopy analysis of MHD natural convection flow of thixotropic fluid under subjection of thermal stratification: Boundary layer analysis. *American Journal of Computational Mathematics,* 9(02), 116-131, (2019). [CrossRef]

[47] Koriko, O.K., Animasaun, I.L., Omowaye, A.J. and Oreyeni, T. The combined influence of nonlinear thermal radiation and thermal stratification on the dynamics of micropolar fluid along a vertical surface. *Multidiscipline Modeling in Materials and Structures,* 15(1), 133-155, (2019). [CrossRef]

[48] Koriko, O.K., Oreyeni, T., Omowaye, A.J. and Animasaun, I.L. Homotopy analysis of MHD free convective micropolar fluid flow along a vertical surface embedded in non-darcian thermally-stratified medium. *Open Journal of Fluid Dynamics,* 6(3), 198-221, (2016). [CrossRef]

Mathematical Modelling and Numerical Simulation with Applications (MMNSA)
(https://dergipark.org.tr/en/pub/mmnsa)

How to cite this article: Shah, N.A., Popoola, A.O., Oreyeni, O., Omokhuale, E., & Altine, M.M. (2023). A modelling of bioconvective flow existing with tiny particles and quartic autocatalysis reaction across stratified upper horizontal surface of a paraboloid of revolution. *Mathematical Modelling and Numerical Simulation with Applications,* 3(1), 74-100. https://doi.org/10.53391/mmnsa.1280184